Barbara Sartori, Dott.

In situ SAXS study of the gas phase Evaporation Induced Self-Assembly of mesoporous material

DOCTORAL THESIS

to achieve the university degree of

Doktorin der technischen Wissenschaften

submitted to

Graz University of Technology

Supervisor

Univ.-Prof. Dipl.-Chem. Dr.rer.nat. Frank Dieter Uhlig

Institute of Inorganic Chemistry

Co-Supervisor

Ass.Prof. Dipl.-Ing. Dr.techn. Heinz Amenitsch

Graz / Trieste, 2017

AFFIDAVIT

I declare that I have authored this thesis independently, that I have not used other than the declared sources/resources, and that I have explicitly indicated all material which has been quoted either literally or by content from the sources used. The text document uploaded to TUGRAZonline is identical to the present doctoral thesis.

16/11/2017

Date

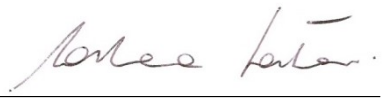

Signature

Abstract

Aerosol technology for producing micro- and nanoparticles based on fast evaporation of aerosol droplets is widely used in various industrial areas in order to produce a variety of materials, such as silica, titania, ceramics or even hybrid compounds.

In particular, spray-drying is a very attractive route to produce mesoporous nanoparticles, because it offers high control of the structure and morphology through “nature inspired” synthetic strategies that combine soft chemical routes to well controlled processing methods[1]. Mesostructured nanoparticles are used for many different applications, from catalysis, sensors, filtration, to therapeutic carriers [1,2].

In the spray drying process, aerosol droplets are formed continuously by an aerosol generator and are driven through evaporators and/or furnaces. During this process, the droplet size and composition are influenced by the external conditions like temperature or humidity, and by the evaporation rate of the solvents. The characterization of nanoparticles produced via spray drying has been treated extensively in the past, as demonstrated by the huge amount of literature available in the field. Nevertheless, a detailed comprehension of the mechanism behind the formation of these hierarchically ordered materials is still missing.

This work aims to give an insight of the condensing mechanism of silica mesoporous nanoparticles produced in the gas phase. The structural evolution of mesoporous material can be followed *in situ* with Small Angle X-ray Scattering (SAXS), which allows to probe the condensing aerosol directly inside the furnace during the process of formation.

Acknowledgments

First, I wish to thank my supervisor Prof. Frank Uhlig, that gave me the possibility to work on this thesis at the TU Graz SAXS outstation at the Elettra Synchrotron in Trieste.

I wish to thank Dr. Heinz Amenitsch, my boss at the Austrian SAXS beamline and co-supervisor, for his support and patience with my “non–mathematically inclined” attitude.

I whish to thank the colleagues of the *SAXS family*: Benedetta, Christian, Richard, Max, Marco, Marcell, Andrea, Sigrid, for being excellent colleagues and most important, good friends. And of the former SAXS crew, thanks to Michi, Shyju, Fernando and Karin, whose work was essential for the success of this project.

A special thanks to Dr. Michaela Flock, for her practical help with the Austrian bureaucracy.

My deepest gratitude to Gianpaolo, for his love and support, whatever happens.

And thanks to all my friends, who sometimes I bother with weird stories of the beamline life.

Last but not least, a warm thanks to my parents, Silvana and Gianni.

… If it works, it works.

I. Shyjumon

TABLE OF CONTENTS

1. INTRODUCTION

1.1 Silicon-based hierarchically ordered materials

According to the IUPAC nomenclature, porous materials can be divided in 3 classes: macroporous, in which the pore size is bigger than 50 µm, mesoporous (2 to 50 nm), and microporous, which pore size are smaller than 2 nm. Hierarchically ordered porous materials can be found in nature, like sea shells, bones and teeth tissue, and they are a beautiful example of how hierarchically ordered structure are well-suited to sophisticated functional characteristics [3].

Silicon-based structured compounds such as natural zeolites are microporous crystalline solids with ordered framework structure that may contain linked cages, cavities or channels of limited size: due to this characteristical feature, they are widely used in industry as catalysts for chemical reaction which take place within the pores, or as molecular sieves. Technological applications of natural materials have been the starting point and a challenge to develope new, synthetic materials with improved, modulable characteristics: synthesized silica-based micro-and mesoporous material can now be functionalized and used in the most different applications: not only as catalysts, filters, sorbents, but also as Lithium-ion battery components[4], as optical sensors[5], and in the biomedical field, thanks to their bio-compatibility, to promote bone regeneration or for drug delivery [6].

In this perspective, it is clear why hierarchically ordered porous materials were an inspiration for the scientific community since the early 70s: a protocol to prepare low density silica was patented by V. Chiola and co-workers in 1971[7] , but the discovery was almost unnoticed until, in the early 90s, a group of scientists from the Mobil Oil Corporation were able to synthesize for the first time mesoporous materials that showed a well ordered structure and a narrow pore distribution[8]. These materials were named MCM41 (Mobil Composition of Matter), and soon after their discovery, a wide interest raised around their characteristics and possible technical applications: these versatile materials were proposed as scaffolds to encapsulate enzimes and bio- molecules to use the resulting hybrid material as biosensors, optical components, electrodes[9]; nanometer-sized silica nanoparticles were suggested as drug carriers[10]; as nanocapsules for control release, with applications in nanotechnology and nanomedicine[11] [12] [13]. Functionalized nanoparticles were proved to be able to remove

pollutants from the water[14]. A big effort was put to understand the behavior of these materials and to develop new syntesis methods in order to control their properties[15–18]; mesoporous silica nanoparticles of various sizes and with different morphologies and pore organization were synthesized and investigated, aiming to tailor the pore size, volume, and architecture on the foreseen application, varying the synthetic procedure[19].

1.2 Nanoparticles characterization

Several techniques are available to characterize the size, the shape, and the structure of nanoparticles: microscopy techniques like Scanning Electron Microscopy (SEM) and Transmission Electron Microscopy (TEM), scattering techniques such as DLS (Dynamic Light scattering), X-ray scattering (Small and Wide Angle X-ray Scattering), neutron scattering[20–22], and gas adsorption methods [23] [24] are currently used to determine mesomaterials properties such as monodispersity, size distribution, mesopores architecture and volume, allowing to obtain a comprehensive model of the sample.

SEM and TEM are excellent tools to determine the shape and surface features of the sample. In a very simplified way, both instruments work sending a focussed electron beam on the sample, and the resulting scattered (SEM) or transmission (TEM) signal is recorded and converted into a magnified image. From these images, a number of different informations on the particles can be extracted, such as size, morphology, and – with TEM – mesopores size and arrangement. TEM in particular, covers the same spatial range as SAXS, but the investigated area is so small that with this technique it is not possible to get a statistically significative image of the entire sample. This restriction can be overcame with SAXS because it delivers informations on the entire irradiated volume of the sample *in situ*, so the two techniques are complementary.

Gas adsorption methods use the adsorption isotherms to calculate the surface area of non-porous solids (BET method [23]) as well as to get informations on the sample's porosity, including the pore size and volume (BJH method [24]). Recently, FTIR spectroscopy was used to estimate the surface area of porous and non-porous silica powders [25]. Among the scattering techniques, DLS (Dynamic Light Scattering) provides statistical informations on the size distribution, as well as on average polydispersity of small particles in suspension.

All these methods provide informations on the final product of the process: none of them deliver informations on the mesoporous silica condensation while the process occur. Synchrotron SAXS proved to be effective to study *in situ* fast self-assembly processes of silica mesoporous material deposited as thin films on silicon surfaces [26] [27], as well as the SBA15 nanoparticles self assembly in batch reactors[28] or to characterize the nanoparticles produced via spray-drying[29]. *In situ* SAXS can be coupled to other analytical techniques, as demonstrated by Grosso and coworkers [26] who studied the structural formation of ordered silica mesostructure in thin films obtained via dip-coating and its correlation with film thickness, coupling *in situ* grazing incidence SAXS and interferometry. Doshi and coworkers characterized the formation of the mesostructured thin films during solvents evaporation combining GISAXS with gravimetric analysis and IR spectroscopy [30]. Another advantage is that synchrotron SAXS allows to investigate even diluted samples obtaining significative data with short exposure time, making it a powerful tool for *in situ* time resolved studies even when the amount of scattering particles in the sample is low, as happens in gas-phase samples[29] .

1.3 Objectives

The goal of this thesis, was the study *in situ* with SAXS of the processes beyond the formation of mesostructured nanoparticles in the gas phase. We choose synchrotron SAXS as the main investigation tool to understand the mechanism of condensation of mesoporous nanoparticles in the gas phase because, as previously mentioned, differently from other investigation techniques with SAXS it is possible to couple a spatial resolution in the order of few nanometers with a time resolution fast enough to detect structural changes that take place in milliseconds.

One of the main problems to face during a SAXS experiment, is to isolate the scattering of the sample from all the external contributions. As the scattering signal is generated by any difference in the electron density, during a measurement, everything around the investigated object generates parasitic scattering – both instrumental such as windows, sample holders, air, and that due to the sample type – as sample container and solvent in case of solution scattering.

Improve the signal-to-noise ratio is thus a big challenge in SAXS analysis, and even more, when the sample under investigations is in the gas phase, as the concentration of scattering particles is very low. To address this problem, we designed and developed a reaction chamber based on the concept of tubular reactor, coupled to an aerosol generator, to study *in situ* the condensation of nanoparticles with synchrotron SAXS [31].

The tubular reactor allows to de-couple time and space: as the aerosol droplets move continuosly along the reactor, each position along the reaction chamber corresponds to a reaction time. The condensing material can be measured for longer time without radiation damage or aging effect, improving at the same time the statistics of the scattering signal.

The final product of the reaction was studied both *ex situ* (collected at the end of the reaction chamber), *in situ* deposited (collected on polymer film at different time during the condensation process), and finally *in situ*, following the evolution of the mesostructure in the aerosol droplets while they travelled along the reaction chamber.

Beside the SAXS experiments, TEM and SEM analysis were made, to confirm the scattering results and to obtain further information on the crystalline structure and size distribution of the synthesized nanoparticles.

1.4 Workplan

The characterization of the Evaporation Induced Self Assembly (EISA) process, and of the mesostructure nanoparticles obtained was done with synchrotron SAXS at the AustroSAXS beamline at ELETTRA Sincrotrone Trieste [32].

The reaction chamber was designed and realized in-house, as part of the project.

The deposited nanoparticles were also analized with SEM and TEM. Scanning Electron Microscopy (images were acquired using a Zeiss Supra 40 instrument from Carl Zeiss MicroImaging GmbH, Germany, using the secondary electrons as the measuring signal) was done at CNR-IOM, Trieste, Italy, while Transmission Electron Microscopy (performed with a JEOL JEM ARM 200F electron microscope operated at an accelerating voltage of 200kV) was done as a CERIC-ERIC proposal at the National Institute of Materials Physics in Magurele,

Romania. In both cases, the scientist responsible for the instrument was present for support during the measurement.

The first experiments aimed to understand better the polymerization of mesoporous materials during self assembly process. To do so, an aerosol generator coupled to a temperature controlled furnace was designed and constructed [33]. To allow *in situ* study of the self assembly process, an observation cell for SAXS was connected to the outlet of the aerosol generator, and a test measurement with gold nanoparticles suspension was performed, to ensure that with the in-house system it was possible to reach a nanoparticle concentration high enough to perform SAXS measurements in the gas phase. After this proof of principle, silica nanoparticles were synthesized and collected to be characterized. The furnace was connected to the aerosol generator, and the nanoparticles were collected at the end of it on filter paper for subsequent SEM and SAXS structural analysis (*ex situ* deposited).

In the following experiments, a windowless observation cell was connected to the end of the furnace and the nanoparticles flowing through it were studied *in situ* with SAXS. The material was also collected on a thin polymer film placed inside the SAXS cell (*in situ* deposited), in the same position where they were observed in the *in situ* measurements.

Further on, a different design of the reaction chamber was made, to observe the EISA process from the beginning, by scanning with the X-ray beam along the temperature gradient inside the furnace. Different precursor solutions were studied, to investigate carefully how the variation of the surfactant and of the solvents influence the self-assembly process.

2. SCIENTIFIC BACKGROUND

2.1 Mesostructured material synthesis: the sol-gel process

One common approach to the synthesis of ordered mesoporous materials is based on the sol-gel process: colloidal solutions (sol) are the precursors for the formation of a continuos inorganic network (gel) through reactions of hydrolysis and condensation [34 35 36].

Common precursors for this reaction are silicon alkoxides like Tetraethoxysilane (TEOS, $Si(OC_2H_5)_4$) or Tetramethoxysilane (TMOS, $Si(OCH_3)_4$), metal alkoxides or metal salts, indicated as $M(OR)_n$ or MX_n respectively, where *M* is a metal atom like Ti, Zr, Al, Sn or Ce, *n* is its oxidation state and *X* and *-OR* are common ligands present in metallic salts or metal alkoxides such as a nitrate, or organic groups [35].

In a typical sol-gel reaction, the metal centers connect to generate metal-oxo or metal hydroxo-polymers in solution. The reaction proceeds in three steps: hydrolysis, condensation, evaporation of solvents [35].

2.1.1 Hydrolysis

Metal alkoxides react readily with water, and the result of the hydrolysis is the formation of reactive hydroxy groups.

$$M(OR)_n + H_2O \rightarrow HO\text{-}M(OR)_{n-1} + R\text{-}OH$$

This reaction can be controlled using catalysts or different solvents or precursors: depending on these factors, the hydrolysis of the metallorganic compound can be complete:

$$M(OR)_n + nH_2O \rightarrow M(OH)_n + nR\text{-}OH$$

and all the OR groups are replaced by hydroxyles, or stop when the metal is only partially hydrolyzed:

$$M(OR)_n + xH_2O \rightarrow M(OR)_n\text{-}x\ (OH)_x + R\text{-}OH$$

2.1.2 Condensation

The second step of the sol-gel reaction is the condensation, in which the hydroxylated metal species react with each other to form an oligomer bridging two metal centers, releasing small molecules like water, or alcohol.

$$HO\text{-}M(OR)_{n-1} + HO\text{-}M(OR)_{n-1} \rightarrow (OR)_{n-1}\ M\text{-}O\text{-}M(OR)_{n-1} + H_2O$$

or

$$HO\text{-}M(OR)_{n-1} + HO\text{-}M(OR)_{n-1} \rightarrow (OR)_{n-1}\ M\text{-}O\text{-}M(OR)_{n-1} + R\text{-}OH$$

This reaction can continue and the subsequent hydrolysis and condensation reactions lead to the formation of networks of metal-oxo based frameworks. Depending on the metal center charactristics such as acidity, lability, or on reaction conditions such as solvent, water contents, pH, catalysts, reaction time, a variety of structures can be obtained, from oligomers to branched polymers, to compact structures. These structures can subsequently grow to form macroscopic aggregates, trapping solvents and small monomers: evaporation of solvents produces the final solid material. Further steps can be done, to remove from the mesostructured material any templating agent that may have been used during the synthesis, to obtain a final structure with empty pores [1] .

2.2 Mesoporous material synthesis – practical approach

Typically, sol-gel processes take place in bulk: the precursors react in the vessel and the solid precipitates are collected and subsequetly treated to remove the surfactant and to stabilize the structure. A number of protocols are available, to obtain mesoporous material either in films on surface, or as solid powders: textured material can be obtained via multiple templating strategies and subsequently processed to obtain a variety of structures for a virtually infinite number of applications [36].

2.3 The EISA process

Besides the precipitation process, mesoporous materials can be synthesized in the gas phase, via aerosol assisted Evaporation Induced Self Assembly (EISA).

Self assembly typically refers to a process in which amphiphilic molecules organize in supramolecular assemblies and act as a template for the final mesostructure. Typical templating molecules are asymmetrical and are made of an hydrophilic and an hydrophobic part. Over a certain concentration, called Critical Micelles Concentration (CMC), the surfactant molecules assemble in micelles or cylindrical structure when in aqueous solution, with the hydrophilic part directed towards the water and the hydrophobic part inside the micelles [37]. At increased concentration, the micelles start to organize in ordered mesophases (i. e. lamellar, cubic, hexagonal) that act as templates for the coassembly of other species, like silicon oxide or titanium oxide. The same process is the basis of the aerosol assisted production of mesoporous nanoparticles: the precursor solution is vaporized in microdroplets of defined size through a temperature controlled reaction chamber: the surfactant concentration reaches the CMC and the coassembly of the mesostructure takes place in the droplets, as the solvents evaporate at high temperature. The final product is then collected at the end of the drying process [38].

2.4 Aerosols

An aerosol is defined as a suspension of solid or liquid in a gas. Often referred in literature as „particles“, aerosol size range goes from 1 nm to 100 µm; these includes for example oil or tobacco smokes, various type of ashes, dusts (coal dust, cement dust), as well as biological related matter like viruses, bacteria, fungi, pollens.

Aerosols present in the environment may be a result of natural events like the soil formation, blazes or volcanic eruptions, or due to pollution phenomena. Being ubiquitous, they have an influence on our daily life: first reports on the effect of particles in the atmosphere on the climate date back already to 44 BC, when a cool summer and a scarce harvest was reported as the result of an eruption of Mount Etna[39]. In the early 19th Century, it was observed that solid particles could arise from chemical reaction in the gaseous atmosphere. In the following decades, several authors reported on the behaviour of the so-

called „atmospheric dust“ and its effect on the environment or on human activities, like e.g. agriculture, or health [40] [41].

In the past, aerosols were mostly considered for their potential harmful effect. More recently, aerosols were studied with increasing interest regarding their properties, and not only as pollutant, or harmful materials. Besides being naturally present in nature, aerosols can be produced and used for their suitable properties: small molecules, latex beads, polymers can be added to the vessel and homogeneously dispersed in the aerosol microdroplets, making it possible to synthesize nanoparticles according to the forseen application [1].

2.5 Aerosol synthesis of mesoporous material

The spray-drying production of nanoparticles is a well established method that consists in flowing a vaporized liquid in a hot gas stream, where the droplets are immediately dried [42]. It offers several advantages: the aerosol assisted process is economically attractive because it is an one-step process, avoiding the necessity to perform additional steps and thus helping to reduce the costs. Moreover, it can run for several hours, keeping the waste of material to the minimum and allowing continuous material production and collection, which is not possible with the classical precipitation pathway. On a smaller scale, it allows the *in situ* study of the mechanisms involved in the mesostructure formation because along with the chemical composition of the precursor solutions, other parameters such as the temperature of the gas stream, or the relative humidity at which the synthesis takes place, can be carefully tuned and controlled [37].

In 1999, Lu and colleagues proposed a versatile route to synthesize mesoporous nanoparticles based on the evaporation induced self assembly of spherical aerosol droplets[38]. The precursor solution was vaporized and subsequently driven by a stream of carrier gas through a temperature controlled tube: each droplet featured a microreactor where the condensation of the silica and surfactant into an ordered network occurred, and the final product was then collected on a filter at the end of the furnace (Figure 1).

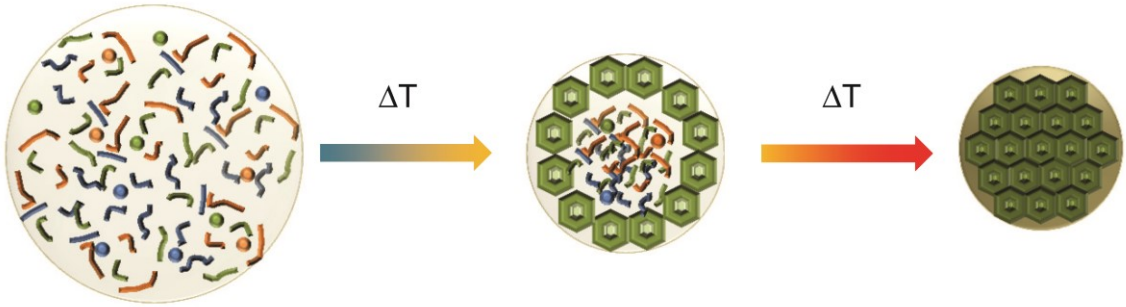

Figure 1: *Sketch of the EISA process to obtain mesoporous nanoparticles by spray-drying.*

Structural analysis on the collected nanopowders revealed the presence of well ordered cubic, hexagonal, or vescicolar nanostructures, depending on the different composition of the precursor solutions [38].

In the following years, several experiments of aerosol EISA were conducted and the nanoparticles deposited at the end of the reaction chamber were analyzed, to correlate the chemical composition and the process parameters such as the temperature, or the relative humidity, with the final size and mesostructure[43] [44]. Though, a detailed insight of the micro/nanoparticles formation was missing.

To fully understand the condensation mechanism, structural studies of the nanopaticles obtained at the end of the condensation is not sufficient. To learn how each of the variables involved influence the particles size and their architecture, and to establish a reproducible synthetic protocol to produce nanoparticles of defined characteristics reliably, it is essential to follow the process step by step, during the evaporation of the solution droplets and until the full condensation of the mesostructured particles, and this is made possible by *in situ* SAXS.

3. ANALYTICAL TECHNIQUE

3.1 Small Angle X-ray Scattering (SAXS)

SAXS is a specific diffraction like technique that allows structural characterization by analyzing the radiation scattered from the sample in forward direction. Depending on the angular range, SAXS delivers information in a range from 100 nm to 1 nm in real space, which can be extended to 1000 nm in USAXS (ultra small X-ray scattering). It allows to measure a variety of samples, from powders to solutions, to supported thin films, to aerosols. The sample can be exposed to different environmental conditions, such as changing temperature, humidity, pressure, and the response to these variables can be measured *in situ* [45].

Until the middle of the 20th century, diffraction studies were done only on crystallized samples, in the wide angle region. in the late 1930s the main principles of SAXS were established by André Guinier, who developed the first small angle scattering camera and used it to study the age-hardening phenomena in metal alloys [46]. In the following decades, with the introduction of the Kratky camera in the 1950s, and later on due to the availability of high brilliance synchrotron radiation sources, the potentialities of the method were developed and small angle scattering was used to obtain information on the overall shape, size, and internal structure of matter [45].

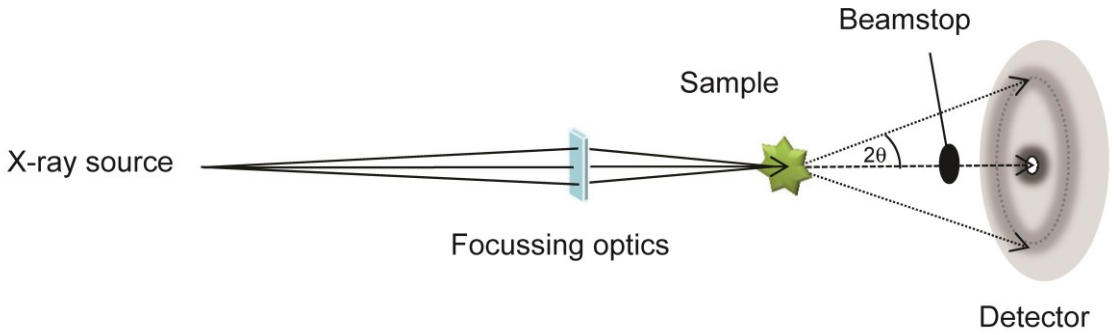

***Figure 2**: Sketch of a generic X-ray experiment.*

3.2 X-rays interaction with matter

When X-rays hit a material, part of them are transmitted, part of them are absorbed and converted into another type of energy (fluorescence radiation, heat), and part of them are scattered in different directions. The scattered photons can be detected at low angles, typically between 0.1° and 10°, giving structural insights on shape and size of macromolecules, characteristic distances of partially ordered materials, and distribution of small objects.

X-rays interaction with matter thus results in three main phenomena [47]:

(i) Absorption occurs when an atom irradiated with X-rays absorbs all the energy of the incident photons: as a result, an electron is expelled from the absorbing atom leaving it into an unstable (ionized) condition. The remaining electrons in the atom are rearranged to restore the atom ground state energy, which then results in fluorescence radiation: these are X-rays, with lower energy and thus higher wavelength from the incident one.

(ii) Fluorescence, when one of the electrons in an outer orbital shell "falls" in a lower electron shell to fills the hole, creating a photon which energy is equal to the specific difference in energy between two quantum states of the electron (i.e., the energy difference of the two orbitals involved) (Figure 3, left), and **Auger electron emission**, which occurs when an electron is expelled out of the atom, to restore its ground state energy. (Figure 3, right)

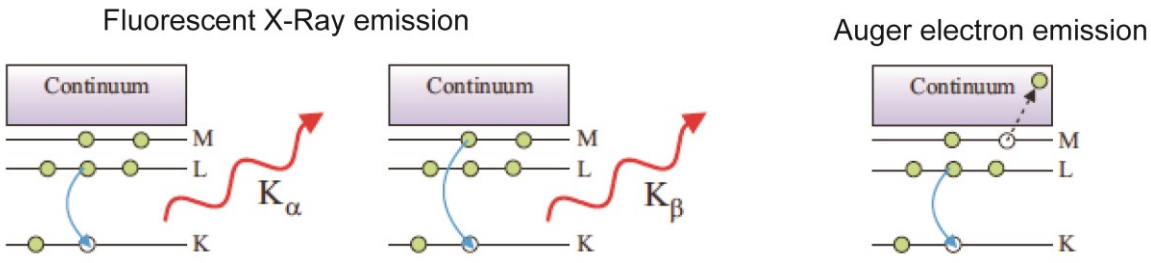

***Figure 3**: Sketch of absorption and Auger electron emission as a resulto of X-ray interaction with matter (adapted from [47]).*

(iii) Scattering can be of two types: (i) in the **inelastic (Compton) scattering** process, part of the energy of the incident X-rays is transferred to the electrons of the irradiated material.

The resulting scattered X-rays will have a different (larger) wavelength and no phase relationship with the incident X-rays. (ii) **Elastic (Thomson) scattering** occurs when the X-ray beam interacts with the sample inducing its electrons to oscillate at the same frequency as the incident radiation. As a consequence, the sample atoms will emit coherent secondary waves[48] .

3.3 Theory of small angle scattering

3.3.1 Scattering and pair distance distribution function

When X-rays interact with a solid, the incident radiation interacts with the electrons in the sample, and will force them to oscillate at the same wavelength of the incident X-rays. As mentioned before, as a consequence of the acceleration during the oscillation the electrons emit coherent secondary waves that will interfere with each other. These secondary waves will generate a 2D interference pattern characteristic of the material structure, where the intensity is modulated at different position of the detection plane [49].

Scattered waves are coherent, that means, that their amplitudes are added, and the intensity is given by the absolute square of the resulting amplitude. The magnitude of the waves amplitude for each electron is the same, and differ only by their phase φ, which is correlated to the position of the electron in space. The phase is $2\pi/\lambda$ times the difference between the optical path and an arbitrary selected reference point, see Figure 4 [49].

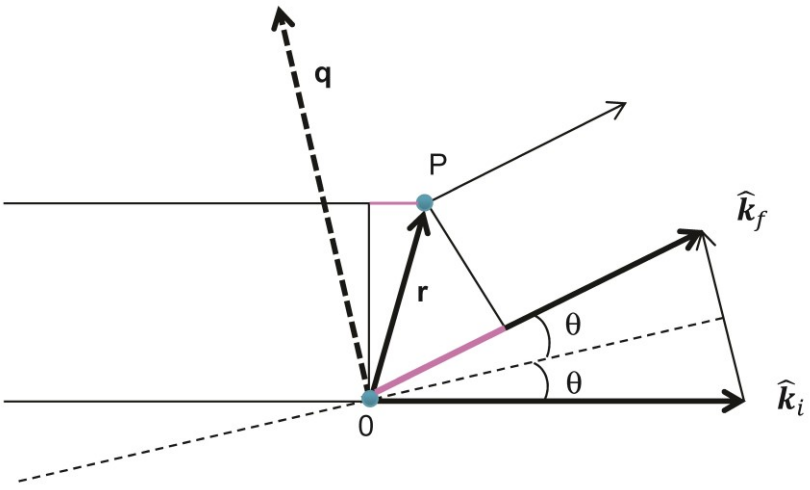

***Figure 4**: Sketch of scattering by two point centres (adapted from [49]).*

If $\widehat{\boldsymbol{k}_i}$ = unit vector of the incident beam, and $\widehat{\boldsymbol{k}_f}$= unit vector of the scattered beam, the path difference between a point P and the origin 0, specified by the vector **r**, is -**r**($\widehat{\boldsymbol{k}_f}$ -$\widehat{\boldsymbol{k}_i}$); the phase φ is then expressed as

$$\varphi = -\frac{2\pi}{\lambda}\boldsymbol{r}\left(\widehat{\boldsymbol{k}_f} - \widehat{\boldsymbol{k}_\iota}\right)$$

which can be written as φ=-**qr** with **q** as scattering vector.

Its magnitude, based on geometrical considerations, is given by:

$$q = \frac{4\pi \sin(\theta)}{\lambda}$$

The vector product **qr** means that the only component important for the phase is **r**: all the points on a plane perpendicular to **q** will have the same phase. In order to sum the amplitudes of all the secondary waves, the electron density ρ(**r**), which is defined as the number of electrons per unit volume, is used and the sum is replaced by an integral.

As result, the amplitude of diffraction in a direction specified by **q**, is the Fourier transform of the electron density distribution in the object, that means, the integration over the whole volume irradiated by the incident beam. Thus, after the usual rotational average according to the sample geometry, the scattered intensity is given by:

$$I(q) = \left\langle \left| \int d^3\,\boldsymbol{r}\ \cdot\ \rho(\boldsymbol{r}) \cdot e^{(-i\cdot\boldsymbol{q}\cdot\boldsymbol{r})} \right|^2 \right\rangle_{rot}$$

The scattered intensity contains information on various sample parameters, such as size, shape, electron density distribution. These parameters can be extracted from the scattering curves by fitting the experimental data with appropriate analytical models [50].

Another way of interpreting the data is that the information collected in the scattering pattern (in inverse space) can be converted into structure in the sample (in real space) by means of the inverse Fourier transform. The scattered intensity of a particle I(q) can be calculated from the pair-distance distribution function (PDDF) p(**r**) of the electron density difference and vice versa. The PDDF is obtained from geometrical considerations and represents the paired-set of distances between all of the electrons within the sample [49]:

$$I(q) = 4\pi \int p(r) \frac{\sin(qr)}{qr}\, dr$$

3.3.2 Form Factor and Structure Factor

In a more general case, the scattering intensity should be considered as composed of two terms, the form factor P(q) and the structure factor S(q):

$I(q) \propto P(q) \bullet S(q)$

The form factor P(q) is the scattering intensity of a single particle, as it was mentioned before, and describes its shape and size. The form factor corresponds to the scattering signal of a monodispersed system, in which the particles are all identical in shape and size.

The structure factor S(q) describes the interference between the neighbour particles in the system. In case of diluted systems the structure factor is approximated to 1 and can be neglected.

In case of concentrated systems, the correlation between individual particles must be considered: if the particles are ordered in a periodic lattice, the scattering pattern will develop in intense peaks (Bragg peaks) at well defined angles, which indicate the existence of crystalline symmetry. The position and intensity ratio between the peaks is characteristic of the specific crystal symmetry [51].

3.3.3 Guinier Approximation

The *Radius of Gyration* R_g can be obtained directly from the scattering curve: it corresponds to the root-mean square of the distance of all electrons from the center of gravity of the particle weighted by the scattering length density. It represents the effective size of a scattering particle, whether it is a polymer chain, part of a protein, a micelle, or a domain in a multiphase system.

At very low angles ($q < 1/R_g$), according to the Guinier approximation [48],

$$\ln I(q) \approx \ln I(0) - q^2 R_g^2/3$$

According to this equation, R_g can be extracted from a $\mathrm{Ln}(I_q)$ vs q^2 plot (Guinier Plot): the slope of the linear fit of the Guinier plot determines the R_g, and the intrercept at q=0 gives

the forward scattering I(0). Once scaled to absolute units, i.e. macroscopic scattering cross section [1/L], by means of a standard material whose scattering power is known [52], I(0) is proportional to the molecular weight and the concentration of the sample [53].

As an example, for a solid sphere of radius R, the *Radius of Gyration* is given by:

$$R_g = \sqrt{\frac{3}{5}}R$$

The Radius of Gyration of simple homogeneous particles are reported in the literature [48].

3.3.4 Porod Approximation and Porod Invariant

Other parameters that can be extracted from the scattering curve are the characteristics of the inner particle's surface and the particle's volume.

At high q values, the intensity I(q) is sensitive to small interparticle distances, thus the scattering signal derives from the internal structure and in particular near the particle surface [54].

For compact particles, the scattering intensity for q>> 1/R (R characteristic dimension) is described with the so-called Porod approximation:

$$I(q) \cong \frac{K}{q^4}$$

where K is a constant dependent on the surface of the particle. This value of the specific surface can be estimated from the Porod plot I(q)*q^4 vs q, analyzing the asymptotic behavior of the intensity curve at high q.

For diluted, non interacting systems, the Porod constant K is correlated to the inner surface to volume ratio :

$$\frac{K}{Q} \propto \frac{S}{V}$$

with Q = Porod invariant, and

$\frac{S}{V}$ = shape to volume ratio.

Contrary to the Radius of Gyration, the Porod invariant Q, which is an integral parameter, is only correlated to the particle's volume and electron density, rather than to the particle shape:

$$Q = \int q^2 I(q) dq \quad .$$

3.3.5 Crystalline Structures and Electron density reconstruction

The crystal structure of a material can be described in terms of its unit cell, which can be considered as a small box, in which atoms are arranged in three dimensions. The unit cells are characterized by the lattice parameters, which are the lengths of the cell edges, and the angles between them. Periodic structures in the sample give rise to Bragg peaks, which positions give informations on the type of lattice and on the unit cell parameter of the sample. In SAXS measurements, the scattering signals are collected in a region at which regular X-ray diffraction experiments are not possible ($2\theta < 10°$): thus, structures with sizes of tens of nanometers can be probed.

The crystal lattice is described by the particular geometric arrangement of the three axis that compose the unit cell. There are 7 lattice systems, which if considered in a three dimensional space, are divided in 14 Bravais lattices obtained combining the seven lattice systems (triclinic, monoclinic, orthorhombic, tetragonal, trigonal, hexagonal and cubic) with one of the centering types (primitive, base-centered, body centered, and face centered) [55]

The relation between the X-ray wavelength λ, the diffraction angle θ and the distance between lattice planes (d-spacing) is defined by the Bragg's Law

$$n\lambda = 2d \sin\theta$$

where n is an integer.

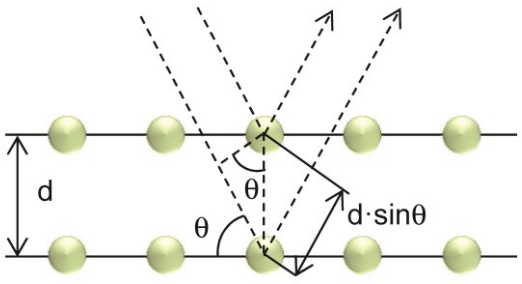

Figure 5: *Schematic illustration of Bragg's law.*

The scattering amplitude of a crystal is dependent on the unit cell structure factor and on the lattice vector R_n that define the crystal:

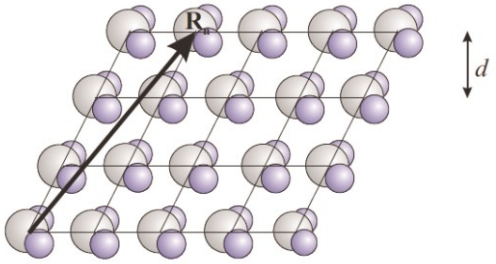

Figure 6: *Scattering from a molecular crystal. The molecules are organized on a lattice with position vectors R_n, and a lattice plane spacing of d. (adapted from [47])*

The reciprocal lattice vectors obtained from the Bragg reflection and the structure amplitudes can be used to reconstruct the real-space electron density of the sample [56].

3.3.6 Electron density reconstruction

The electron density $\rho(r)$ for a centrosymmetric unit cell can be expressed as a Fourier series of cosines by

$$\rho(\boldsymbol{r}) = \rho_{average} + \sum_{\boldsymbol{q}} A_{\boldsymbol{q}} \cos(\mathbf{q} \cdot \mathbf{r})$$

where A_q is the Fourier coefficient, ***r*** is the vector to the position in the unit cell, ***q*** is the Fourier vector, and $\rho_{average}$ is the average electron density [57].

From a crystalline isotropic sample, the scattering pattern collected on a 2D detector consist of a series of concentric diffraction rings, each corresponding to a Fourier component **q** of the electron density. The integrated intensities of each ring can be determined by integrating the area under the diffraction peaks. The absolute values of the Fourier coefficients A_q can be calculated from the integrated intensity of the diffraction peak, as

$$|A_{\mathbf{q}}| = \sqrt{\frac{I(|q|)|q|^2}{CM_{h,k}}}$$

where, for a 2D hexagonal unit cell,

$$q = \frac{4\pi}{\sqrt{3a}}\sqrt{h^2 + k^2 + hk}$$

q^2 is the Lorenz correction for the used diffraction geometry [58], C is a constant to rescale the diffraction intensity in absolute units to the real intensity measured in the real experiment, $M_{h,k}$ is the multiplicity of the h and k reflection respectively, a is the unit cell parameter [59 60]

The correct sign of the Fourier coefficients A_q (i.e. +1 or -1) should be determined either from models or by iterations. In the latter one the correct "phasing" of the coefficients will be found by taking into account possible boundaries, derived from other observation methods, such as the higher electron density of the silica shell if compared to the core.

The interpretation of small angle scattering data rely mostly on the possibility to find a model, which scattering curve agrees within experimental error to the scattering curve of the sample. Although information on size, shape and surface can be deduced directly from the scattering curve, a deeper understanding of the sample can be reached applying structural models to the experimental curves.

In this particular work, a structural model first presented by Imperor-Clerc and coworkers [61] was applied to model the scattering data and obtain information on the architecture of the nanoparticles. The details of the model and the fitting function are described in paper B [62].

4. RESULTS AND DISCUSSION

The experiments and the results described in the following sections are reported in:

A. *Novel in situ setup to study the formation of nanoparticles in the gas phase by small angle X-ray scattering.* Shyjumon, I., Rappolt, M., Sartori, B., Amenitsch, H. Laggner, P. The Review of scientific instruments, 79, 4, 43905 (2008)

B. *Mesostructured silica aerosol particles: comparison of gas-phase and powder deposit X-ray diffraction data.* Shyjumon, I., Rappolt, M., Sartori, B., Cacho-Nerin, F., Grenci, G., Laggner, P., Amenitsch, H. Langmuir : the ACS journal of surfaces and colloids, 27, 9, 5542-8 (2011)

C. *Aerosol flow reactor with controlled temperature gradient for in situ gas-phase X-ray experiments - Measurements of Evaporation Induced Self Assembly (EISA) in aerosols.* Jungnikl, K., Rappolt, M., Shyjumon, I., Sartori, B., Laggner, P., Amenitsch, H. Aerosol Science and Technology, 45, 795-800 (2011)

Section 4.5 includes unpublished results (paper in preparation).

4.1 Design and realization of an aerosol generator prototype

Inspired by previous works which aimed to characterize with SAXS the mesophase formation of ethanol rich and water rich TEOS/CTAB (inorganic/surfactant) and $TiCl_4$/Brij58 systems influenced by the drying temperature [29], we designed an experimental setup that coupled an in-house assembled aerosol generator based on a low cost ultrasonic ceramic disc mist maker with a heating furnace which could be heated up to 300°C. (Figure 7-8, adapted from paper A [33]).

The heating furnace is necessary because a thermal treatment between 125°C and 250°C helps to avoid the coalescence of the particles that may occur if the condensation does not proceed enough to stiffen the droplets surface [43].

The mist maker we chose has a working frequency of 1.7 MHz. When submerged in the precursor solution, the ultrasonic waves generated by the piezoelectric disc induce the formation of tiny peaks at the surface of the solution, which break off generating droplets. The droplets diameter and the effective evaporation rate were estimated in a cold trap

experiment with pure water, at ca -50°C: the droplets size proved to be about 2.5µm diameter, and the averaged evaporation rate at the end of the transfer line to our heating furnace was estimated to be 14 ml/hr. The heating zone consist of a 1 m long quarz tube wrapped with a ceramic heating tape, connected to a custom built control unit. The temperature into the heating zone was monitored with a Pt100 thermoresistor and the temperature profile was measured across the full diameter of the tube, showing a difference of about 1°C between the center and the wall at a T set to 200°C, after few minutes of stabilization.

A variable flow rate (1-15 SLM) dry air unit was connected to the aerosol generator container and the air stream delivered the aerosol droplets through the heating zone, and into a windowless SAXS observation cell. After the observation cell, an exhaust system was employed to remove efficiently the nanoparticles from the environment.

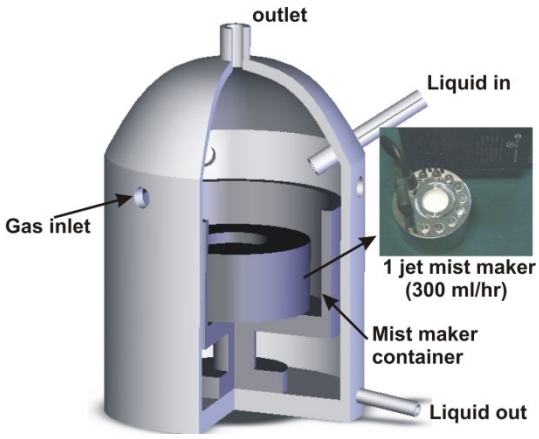

***Figure 7**: Detailed scheme of the mist maker container, including the aerosol generator. A gentle gas flow is supplied through a circular gas inlet system (not shown), to drive the aerosol to the outlet avoiding turbulence and condensation.*

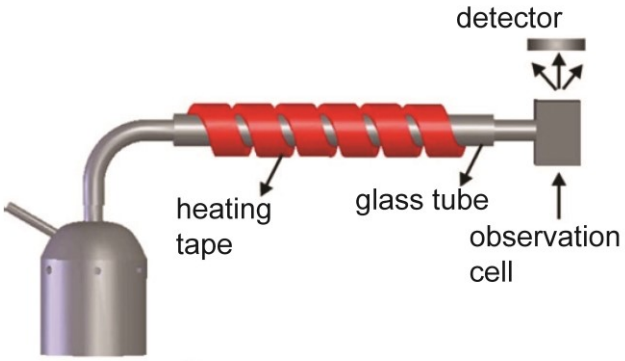

Figure 8: *Sketch of the setup for the gas phase analysis of nanoparticles produced via EISA. The aerosol droplets move along the heating quarz tube, which temperature is controlled by an external unit. Figures adapted from paper A* [33].

The very first experiment was performed to prove the feasibility of the SAXS measurement in the gas phase. Gold nanoparticles were synthesized offline by the citrate route, according to Turkevich and Stevenson [63], were dispersed in water and the dispersion was measured with SAXS. The synchrotron X-ray scattering measurements were conducted at the high flux Austrian SAXS beamline at Elettra Synchrotron, Trieste [32], in a q-range from $2\pi/330$ Å^{-1} to $2\pi/15$ Å^{-1}, at a photon energy of 8 keV.

The *Radius of Gyration* (R_g) of the nanoparticles in solution was estimated around 5 nm in a solution scattering SAXS experiment. To demonstrate the feasibility of the gas phase measurements, the aerosol generator was filled with the gold nanoparticles solution. The outlet of the fog generator was then connected directly to the windowless observation chamber, and an exhaust system was used to remove the nanoparticles from the sample cell after the measurements. The scattering signal from the flowing nanoparticles was collected *in situ* for an exposure time of 240 seconds.

After background subtraction, the collected data allowed to estimate the *Radius of Gyration* of the scattering material. As shown in paper A, the dimension obtained was about five times bigger that that of the single nanoparticles, demonstrating that nanoparticles aggregation induced by the confinement occurred in the aerosol droplets. This result proved that each droplet was acting as a microreactor, and confirmed that our setup could be used to study *in situ* the nucleation and growth of nanoparticles.

4.2 Mesoporous silica nanoparticles synthesis and SAXS characterization of gas phase and deposited material

Silica mesoporous nanoparticles were produced by evaporation Induced Self Assembly (EISA) according to Boissiere *et al.*[29], from a solution containing tetraethylorthosilicate (TEOS) as the inorganic precursor, cetyltrimethylammonium bromide (CTAB) as the surfactant, deionized water, and concentrated HCl, at a molar ratio of CTAB/TEOS/H_2O/HCl 0.14:1:41:0.13. The pH of the solution was ~2.5. The dryer temperature was set to increasing temperatures from room temperature to 250°C and the air stream flowrate was adjusted to 5 LPM, corresponding to a resident time of ca. 10 seconds in the heating zone.

To determine the structure of the nanoparticles, a filter paper was placed at the end of the dryer; the nanoparticles were collected for 2 hours, carefully dried and filled into a 1 mm diameter glass capillary. The SAXS pattern of this collected material clearly showed 4 reflections corresponding to a 2D hexagonal phase and one peak from the crystalline CTAB (Figure 9).

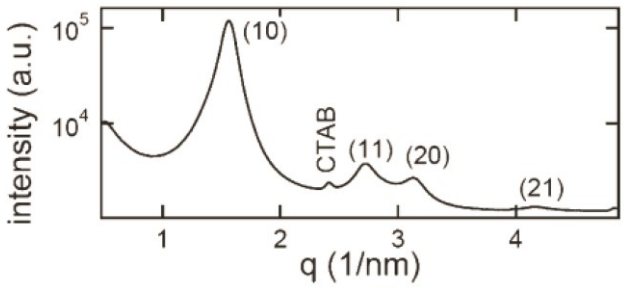

Figure 9: *Ex situ deposited data obtained at 200°C, flowrate 5 LPM. The (10), (11), (20) and (21) reflection for the hexagonal phase, as well as one reflection from crystalline CTAB are indicated (adapted from paper B [62]).*

The scattering signal from the aerosol was collected in the observation cell at the end of the dryer, at different temperatures, for an exposure time of 600s. These first results are reported in figure 4 of paper A: one peak corresponding to the (10) reflection of the hexagonal phase is visible in the scattering signal.

The material was collected at increasing temperature on silicon wafers and was analized with SEM to determine the size distribution of the nanoparticles.

The size distribution, as shown in Figure 10 (adapted from paper A), ranged from few hundreds of nanometers to few micrometers, and was remaining more or less constant with increasing dryer temperature, demonstrating that the final particles size is influenced mainly by the size of the aerosol droplets.

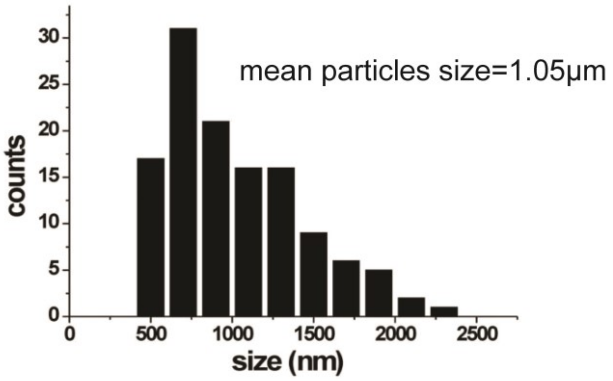

Figure 10: *Silica nanoparticles mean size distribution (adapted from paper A*[33]*).*

In a second set of experiments, the scattering data were collected from nanoparticles synthesized at 200°C in gas phase, and immediately after deposition on a polymer film (*in situ* deposited). As shown in figure 11, adapted from paper B, due to the lower amount of scattering material the signal of nanoparticles in the gas phase is weak if compared to that of the *in situ* deposited particles: in the gas phase data only the strong (10) reflection was visible, while the scattering pattern obtained from the particles deposited on the polymer film placed in the observation cell showed also the higher order reflections typical for the hexagonal phase, i.e. the (10), (11) and (20). Informations could be extracted from both measurements, as the gas phase data allowed to deduce the effect of the process parameters, and those from the *in situ* deposited material revealed the details of the mesostructure.

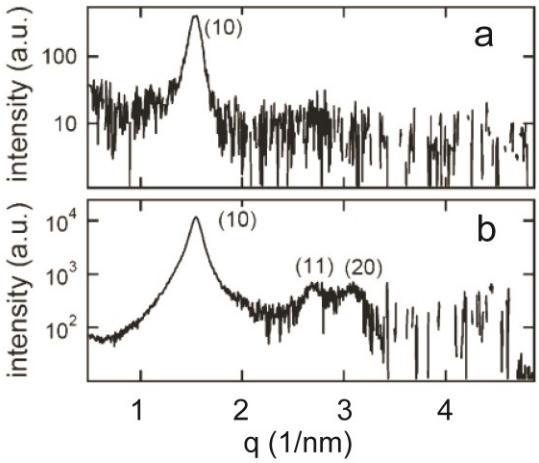

***Figure 11**: Comparison of the gas phase (A), and in situ deposited (B) data obtained at 200°C, flowrate 5LPM. The CTAB /TEOS molar ratio was 0.14. The (10) reflection in the gas phase data, and the (10), (11), and (20) reflection for the hexagonal phase in the in situ data are shown. (adapted from paper B [62])*

From the position of the (10) reflection, we could calculate the unit cell (lattice) parameter of the mesostructure, *a*, and the comparison between the value obtained from *in situ* gas phase, *in situ* particle deposits (investigated immediately after deposition), and ex situ particle deposited data (recorded after extensive drying), showed the influence of hydration on the particles mesostructure.

4.3 Structural parameters of the mesostructure

The core radius was calculated according to a structural model based on the scattering amplitude of cylindrical particles[64], proposed by Imperor-Clerc and coworkers[61]. This model assumes that the mesoporous material is an assembly of monodispersed cylinders, ordered in a 2D-hexagonal lattice and with a perfect circular cross section with an inner CTAB core surrounded by an outer silica shell with two different, but uniform, densities (Figure 12).

With this model, the corrected integrated intensities $I_{h,k}$ of different diffraction peaks (*h,k*) were fitted applying

$$I_{h,k}\left(q_{h,k}\right) = K\left(\frac{2J_1\left(q_{h,k}R_1\right)}{\left(q_{h,k}R_1\right)}\right)^2$$

where K is a scaling constant which includes the electron density contrast and J_1 is the Bessel function of the first kind of first order.

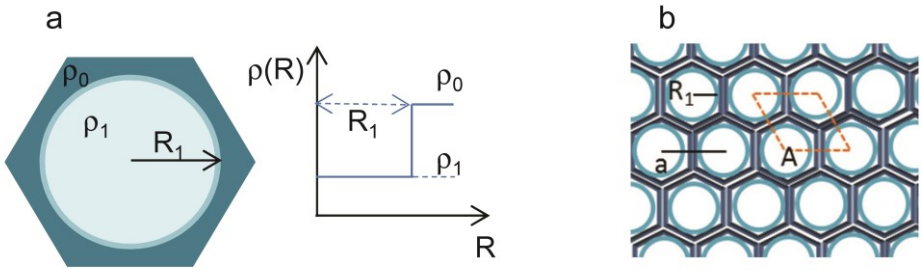

Figure 12: *(a) Sketch of the two-density model structure; (b) unit cell A, lattice parameter a, CTAB core radius R_1.*

From these two parameters, a and R_1, we could deduce the silica wall thickness, $\Delta = a - 2R_1$, and the silica cross sectional area A_Δ, defined as $A_\Delta = \sqrt{3}/2a^2 - \pi R_1^2$.

The experiments were repeated at different temperature, as this parameter drives the evaporation rate of the solvents and at the same time influences the silica condensation, thus determining the final structure of the particles. Further, the CTAB/TEOS molar ratio was varied, with a ratio of 0.06, 0.14, and 0.25, keeping the TEOS constant and varying the CTAB amount.

The details of the structural features extracted from *in situ*, *in situ* deposited and *ex situ* deposited data are summarized in Table 1 and are reported in paper B: the temperature inside the furnace showed to be critical for the formation of the mesostructure: despite it was impossible, with the current setup, to follow the first stages of evaporation of the solvents, it was still possible to investigate the effect of residual hydration when the experiments were done al low temperature. Comparing the *in situ* (I) and *ex situ* deposited (III) nanoparticles produced at 80°C, a difference of approximately 1 nm in the calculated unit cell parameter a could be observed. This means that both the surfactant radius R_1 and the silica wall thickness were larger. This effect is evident even at higher temperatures: at 140°C, the unit cell parameter of *in situ* and *in situ* deposited were 5.01 nm and 4.76 nm respectively. The ex situ deposited nanoparticles had a unit cell parameter value of 4.66 nm, while the difference of the silica matrix thickness was 1.5 Å. This demonstrated a shrinkage of the CTAB radius with increasing temperature. Interestingly, the difference of R_1 between the *in situ* and the *ex situ* deposited data is around 2.3 Å, which corresponds approximately

to one water layer[65]: this means, that CTAB micelles are still hydrated even at high temperature.

	T (°C)	a (nm)	R_1 (nm)	Δ (nm)	A (nm^2)	$A_Δ$ (nm^2)	$A_Δ/A$
in situ	60	6.17±0.04	-	-	-	-	-
	80	5.97±0.03	-	-	-	-	-
	100	5.84±0.01	-	-	-	-	-
	120	5.29±0.01	-	-	-	-	-
	140	5.01±0.01	-	-	-	-	-
	160	4.84±0.01	-	-	-	-	-
	180	4.76±0.01	-	-	-	-	-
	200	4.72±0.01	-	-	-	-	-
ex situ	80	5.06±0.01	-	-	-	-	-
	100	4.95±0.01	-	-	-	-	-
	120	4.86±0.01	2.11±0.09	0.64±0.11	20.44	6.44	0.32
	140	4.76±0.01	2.09±0.08	0.60±0.09	19.92	6.10	0.31
	180	4.72±0.01	1.94±0.08	0.84±0.09	19.29	7.45	0.38
	200	4.70±0.01	1.88±0.08	0.93±0.09	19.15	7.98	0.42
ex situ deposited	80	4.93±0.01	1.96±0.04	1.01±0.08	21.04	8.98	0.42
	150	4.66±0.01	1.86±0.04	0.95±0.07	18.81	7.94	0.42
	200	4.66±0.01	1.87±0.03	0.93±0.07	18.81	7.83	0.42

***Table 1**: Structural parameters of in situ, ex situ, and ex situ deposited nanoparticles at different furnace temperatures (from paper B [62]):*

a: unit cell parameter,

R_1: core radius,

$Δ = a - 2R_1$: deduced silica wall thickness,

$A_Δ = (3)^{1/2}/2a - πR_1^2$: silica cross-sectional area.

The slightly lower cell parameters for the *ex situ* deposited particles as compared with the *in situ* deposited particles data demonstrates that the structure condensation is complete only after protracted drying: this confirms the importance of an *in situ* study to understand the mechanism of the self-assembly process.

Besides the temperature (Figure 13 a), the surfactant/silica molar ratio is also known to have an effect on the nanoparticles' mesostructure (Figure 13 b).

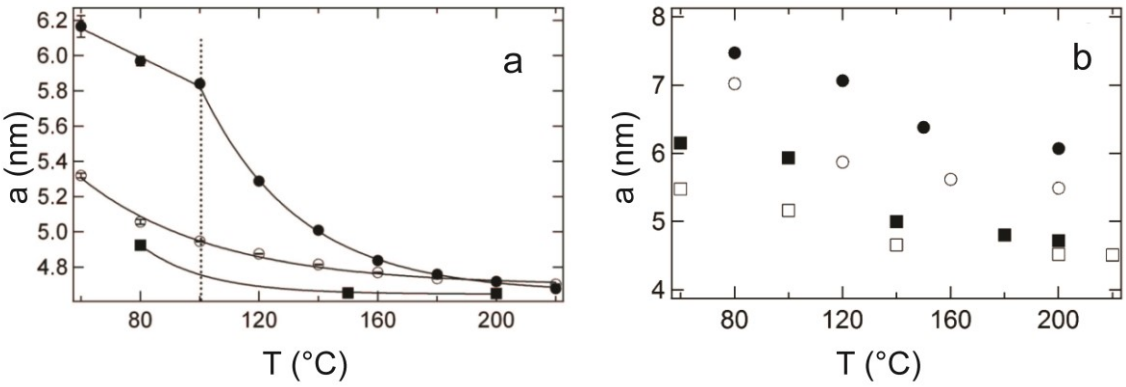

***Figure 13**: Calculated cell parameter a for ex situ collected data in dependance of the dryer temperature and of the CTAB/TEOS molar ratios (a): temperature dependance of solution with CTAB/TEOS 0.04 (●), 0.06 (o) 0.14 (■) and 0.25 (□). (b) Calculated cell parameter for gas phase (●), in situ deposited (o) and ex situ deposited (■) data obtained at different temperatures. CTAB/TEOS molar ratio was 0.14. The flowrate was set to 5LPM. (from paper B [62])*

Bore and coworkers demonstrated that 2D hexagonal ordered nanoparticles can be produced at high temperature (425°C) with a CTAB/TEOS molar ratio between 0.094 and 0.28[43]: they demonstrated with TEM analysis that the hexagonally ordered pores are organized in adjacent regions, with the pore axis oriented at different angles one to each other. In our experiments we set the furnace temperature at 80°C, and changed the surfactant molar ratio with respect to the silica one, which was kept constant. Our results confirmed the impact of the surfactant to silica ratio when the nanoparticles were produced at low temperature: we obtained 2D-hexagonally ordered nanoparticles in a CTAB/TEOS range between 0.06 and 0.25, with a small decrease in the core radius R_1.

This can be explained keeping in mind the critical packing parameter *g* of the surfactant molecules [66], which is defined as

$$g = V/A_I * L$$

where V is the volume of the hydrophobic chain, A_I is the area of the CTAB headgroup at the micelle's interface, and L is the length of the hydrophobic chain. As in this case the temperature is kept constant, it has no influence on the chain length so L does not change during drying. Thus, the headgroup area at the interface is responsible for the size of the micelles. Icreasing the surfactant concentration, the counterion concentration (in this case, Cl^- as the reaction happen in presence of HCl) becomes lower, and as a consequence the headgroup charges shielding decrease [67]. The area at the surface A_I increases, and this leads to a smaller critical packing parameter, that implies that the micelles curvature increase, inducing the shrinkage of the pores diameter.

A comparison of the cell parameter a calculated from the data obtained at different surfactant to silica ratio, showed that the unit cell parameter decrease with increasing CTAB to TEOS ratio (Figure 14). This was ascribed mainly to a thinning of the silica wall, because the surface fraction of surfactant increase with respect to the silica quantity.

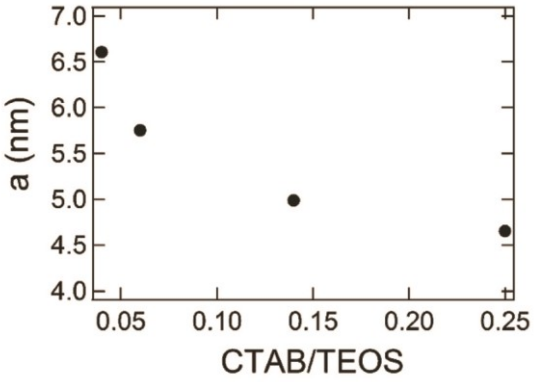

Figure 14: *calculated cell parameter a as a function of the CTAB/TEOS ratio of nanoparticles produced at T=150°C. The flowrate was set to 5LPM. (from paper B [62])*

The analysis of the deposited data allowed us to extract the Fourier amplitudes of each reflection, from which, with the lattice parameter and an appropriate guess of the phase value, it was possible to reconstruct the electron density map of the sample in real space. The details of the reconstruction of the electron density maps are reported in paper A.

4.4 *In situ* study of mesoporous silica during solvents evaporation

Following the results obtained from the previous studies, that demonstrated that the lattice parameter *a* of the silica hexagonal phase depends strongly on the conditions of the sample preparation, we designed and constructed a new setup, that allowed the *in situ* study of the silica condensation along the furnace: the aim of the experiment was to observe how the self assembly process occur during the solvents' evaporation, scanning along the temperature gradient with the X-ray beam.

We designed and built a new setup, shown in Figure 15: it consist of a windowless experimental chamber made of two tubular parts which feature an axial slit along the whole lenght, to make possible the observation of the nanoparticles condensation *in situ*. The observation chamber at the end of the dryer was removed, and the inner, sliding reaction chamber was equipped with two independent temperature controls. The first, water cooled segment (cold zone) stabilizes the experimental conditions of the aerosol droplets, while the second one (heating zone) provides a steep temperature gradient for nanoparticle condensation. In the first version of this new setup, the heating was provided by ceramic heater tapes connected to the temperature controller [68]. In a subsequent improvement of the setup, the ceramic tapes were exchanged with four heating rods, so we were able to increase the heating temperature over 300°C. A PT100 was mounted inside the inner tube, and connected to the temperature controller to adjust the heating according to the aerosol temperature. The two tubes were mounted inside an external shell with a vertical slit wide enough to allow simultaneous small and wide angle X-ray scattering (SWAXS) measurements. The thermostated parts featured an axial slit to collect X-ray scattering data along the full length, and were designed to slide inside the confinement shell while the X-ray window opening stayed fixed in the beam. An efficient exhaust was connected at the outlet of the tube, and on top of the vertical slit, to avoid contamination of the beamline environment.

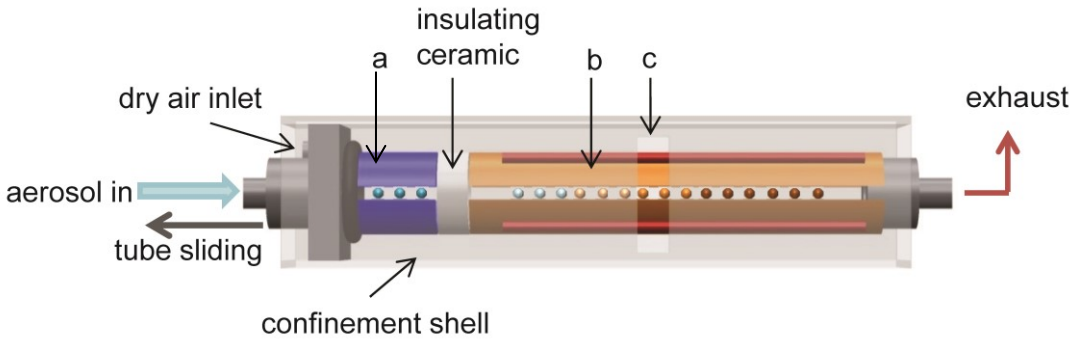

***Figure 15**: Sketch of the flow reactor: the aerosol droplets are driven into the drying (cold) zone (a) of the chamber, and subsequently into the heating zone (b) . The position of the confinement shell with the X-ray opening (c) is fixed, while the inner tube with axial slit can be moved by a motor stage to change the measurement position within the aerosol flow path.*

A commercial atomizer aerosol generator (TSI 3079 Atomizer, Topas GmbH) with adjustable flowrate, equipped with a nozzle that produce monodispersed droplets of an average diameter of 200 to 300 nm was used to generate the aerosol droplets: these were carried through the cold zone, to stabilize the droplets conditions, and then through the heating zone. An insulating ceramic insert was placed between the cold and hot part of the dryer, to achieve a steep temperature gradient inside the reaction chamber.

The temperature profile along the cold and heating zones was characterized with aerosol at different set temperatures (temperature in the heating zone was set from 100 to 180°C with ceramic tapes as heat source, and from 90 to 200°C when heat rods were used), with pure water and 70% EtOH (Figures 16 - 17). The heating capacity and evaporation of the solvents affected the temperature inside the dryer, this effect being more evident near the cold/heating zone interface, as described in paper C [68]. The heating rods showed to provide more efficient heating (figure 17) as the temperature measured in the middle of the aerosol path was higher that the set one. A calibration of the system was thus performed before every experiement, to optimize the chamber temperature.

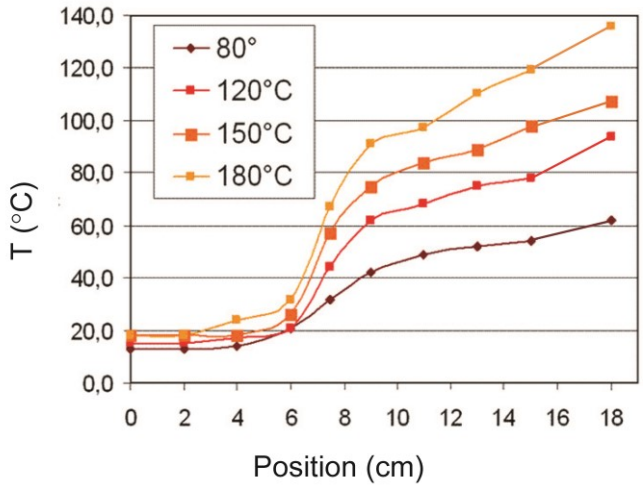

***Figure 16**: Temperature profile inside the reaction chamber, in presence of aerosol (EtOH 70%). Heating was provided by ceramic heater tapes.*

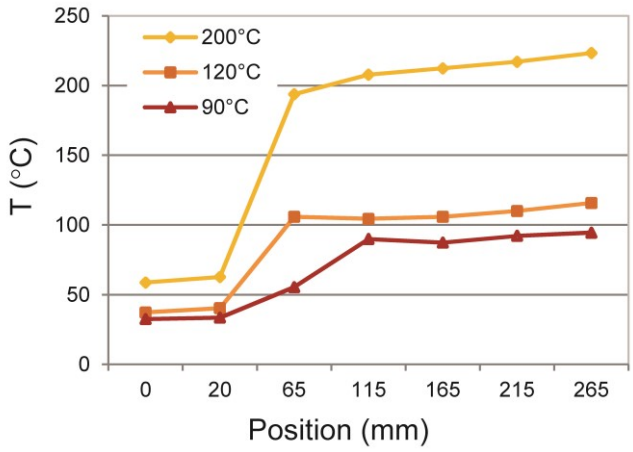

***Figure 17:** Temperature profile inside the reaction chamber, in presence of aerosol (EtOH 70%). Heating was provided by heating rods.*

To test the feasibility of *in situ* study of the mesophase formation during the drying process with the new setup, and to determine the optimal flowrate of both aerosol and carrier gas stream, an experiment to study the self assembly process of the surfactant (CTAB) mesophase was performed. An aerosol was produced from solutions based on the reaction proposed by Lu *et al.* [38], but containing only CTAB dissolved in equal molar amount of EtOH only for the first test, and of EtOH and H_2O for a second one. TEOS was not added to the reaction in these tests.

As visible in figure 3 (a) of paper C, the gas phase data collected from the ethanol-only solution showed a clear increase of the peak height from the beginning of the mesostructure formation, and subsequent drying, due to the crystallization of the CTAB in a lamellar mesostructure, in agreement with the literature [69]. The formation of a lamellar phase at the interface of the aerosol droplet with air, may have induced the surfactant bilayer to tilt, and this would explain why the maximum observed dimension of the lattice spacing, ca. 3 nm, is larger than the length of the stretched tail group of CTAB (ca. 2.2 nm). The fluctuation of the d-spacing during the drying process are due to the evaporation of the solvent. Initially, the evaporation of the interlamellar ethanol induces the decrease of the lattice spacing. It increases again in the final drying stage, when the ethanol intercalated in the CTAB layers evaporates. The opposite behaviour is observed in the EtOH/H_2O solution (Figure 18): this can be explained as the result of the steric effect of the water molecules associated with the surfactant head groups during the first stages of evaporation.

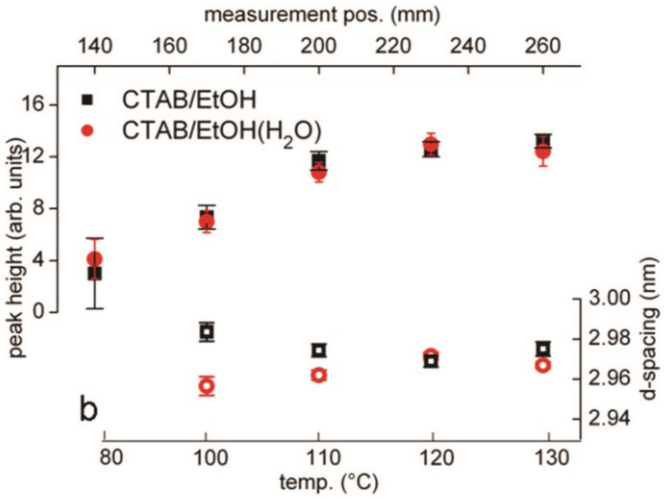

Figure 18: *Peak height (full circles/squares) and d spacing (open circles/squares) during drying of CTAB/EtOH and CTAB/EtOH/(H_2O) solutions (from paper C [68]).*

As explained by Doshi and coworkers[30], ethanol actively shields the hydrophobic tails of the surfactant molecules from water, and promotes the interdigitation of heads and tails groups. When ethanol starts to evaporates, the tails interdigitation extent decreases inducing a lattice expansion. The progressive ethanol evaporation induces the tails to stretch, to minimize the interaction with water.

4.5 Phase transformation during aerosol synthesis of silica nanoparticles

4.5.1 Solution aging effect

Previous studies on thin films [70] [26] [71], demonstrated that the condensation of silica oligomers that occurs in the vessel during the aging of the solution, has an influence on the final mesostructure of the silica film. To study the influence of the precursors solution condensation on the mesostructure of the nanoparticles synthesized via spray drying, we measured the aerosol obtained from two aliquotes of the same batch of ethanol-rich solution (molar ratio TEOS/EtOH/H_2O 1: 20: 5, according to Lu *et al.*[38]), aged 1 hr and 12 hrs respectively. During aging, the solution was kept under gentle stirring in a closed vessel, to avoid ethanol evaporation. The aerosol of the aged solutions was subsequently measured *in situ*, at the same position in the heating zone, for about 1.5 hrs. The temperature of the heating zone was set to 150°C. The precursor solution vaporized through the nozzle was partly driven through the connection tube to the experimental chamber, partly recirculated in the reservoir. During this recirculation, the solution was depleted in ethanol. There wasn't a significative change in the d-spacing of the nanoparticles obtained from the two measured aliquotes at the beginning of the aerosol experiment. On the other hand, we observed a slight increase in the lattice spacing already at the beginning of the cold zone during the aerosol experiment as a consequence of depletion of ethanol from the solution.

4.5.2 Solvents composition effect

We performed a sistematic study on the effect of solvents composition in the precursor solution, (Sartori *et al*., in preparation), changing the ratio between EtOH and H_2O while keeping the other components constant, to cover a range from ethanol rich (Si/templating agent/EtOH/H_2O 1: 0.14: 17: 5, adapted from Lu *et al.* [38]) to water rich formulations (Si/templating agent/EtOH/H_2O 1: 0.14: 0: 41) [29]. The temperature of the heating part of the reaction chamber was set to 90°C in this experiment.

Aerosol synthesized nanoparticles were obtained from a precursor solution containing cetyltrimethylammonium bromide (CTAB) as templating agent, and tetraethylortosilicate (TEOS) as silica source. The mixed precursor solution was stirred at room temperature for one hour in a closed vessel and measured immediately. The pH of all the final solutions was

adjusted to ~2.5. To study the effect of the differential evaporation of the solvents on the mesostructure, the silica to surfactant molar ratio was kept constant (TEOS/CTAB= 1 : 0.14), while the relative EtOH to H_2O ratio was modified, maintaining the total volume of the final solution. The molar ratio for the sol-gel precursors is summarized in table 2.

Table 2: *Molar composition of each tested solutions*

CTAB	TEOS	EtOH	H_2O	HCl	EtOH: H_2O	Solution
0.14	1	0	41	0.026	0:1	**A (water rich)**
0.14	1	5.3	16	0.026	1:3	**B**
0.14	1	12	12	0.026	1:1	**C**
0.14	1	14	7	0.026	2:1	**D**
0.14	1	17	5	0.026	3.4:1	**E (ethanol rich)**

The aerosol flow rate was set to 3 L/min for all the experiments. At the selected reaction conditions, the total resident time of the nanoparticles inside the reaction chamber in the X-ray scanning range is 6.65 seconds. The temperature at each measurement position was monitored with a sensor placed at the same position as the X-ray beam inside the reaction chamber (Figure 19).

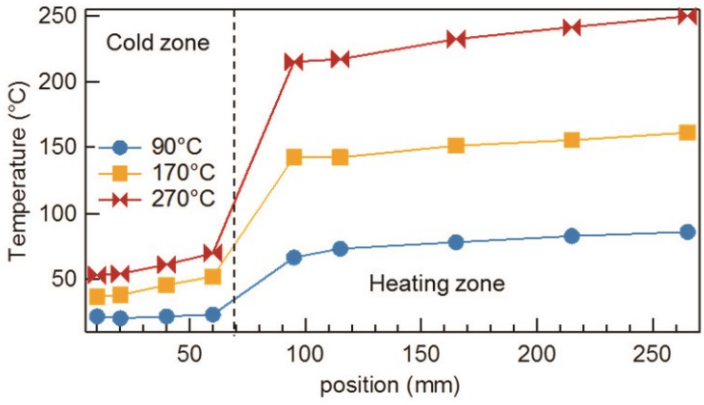

Figure 19: *Axial temperature profile of aerosol inside the reaction chamber. The calibration was done with a solution of 50 $^{v}/_{v}$ ethanol in water. The maximum temperature of the reaction chamber was set to 90°C (circles), 170°C (squares) and 270°C (ribbons), respectively.*

For the *ex situ* experiments, a vacuum pump was connected to the end of the heating chamber, and the nanoparticles were collected on a filter positioned between the reaction chamber and the pump.

In situ SAXS measurements were performed at the Austrian SAXS beamline at Elettra Sincrotrone Trieste, Italy [32] at a photon energy of 8 keV. SAXS patterns were recorded with a Pilatus 1M detector (Dectris, CH) covering a q-range from 0.08 nm^{-1} to 5.04 nm^{-1}. The scattering data were collected in steps of 20 mm along the drying part and 50mm along the heating part of the reaction chamber, sliding the thermostated section of the reaction chamber with respect to the X-ray beam with a high precision linear stage (Newport Corporation, Irvine, California, USA). Exposure times were set to 60s per image.

The experiments were repeated at various temperatures and using solutions with different solvent composition. Before each measurement and after setting the heating chamber temperature, a background measurement without aerosol was taken at each position. Primary data reduction and integration of the scattered intensity were done using the program Fit2D [72]. Subsequent data analysis was carried out in Igor Pro (Wavemetrics, USA). The scattering data analysis was focused on the strongest first-order reflection, due to the weak scattering signal of the aerosol.

The normalized, background subtracted scattering patterns were fitted to the following function

$$I_{(q)} = A + bq + I_0 / \left(1 + \left(\frac{q - q_0}{FWHM_0}\right)^2\right) + I_1 / \left(1 + \left(\frac{q - q_1}{FWHM_1}\right)^2\right)$$

which combines a constant offset *A*, a linear baseline with slope *b* to correct the residual background, and two independent Lorentzian peaks, each characterized by its position q_i, its full width at half maximum $FWHM_i$ and the relative intensity I_i.

Figure 20 shows the scattering data obtained from the ethanol-rich (a) and the water-rich (b) solutions along the whole length of the reaction chamber: in this experiment, the temperature in the drying “cold” zone was kept below 25°C, the maximum temperature measured at the end of the heating zone was 86°C.

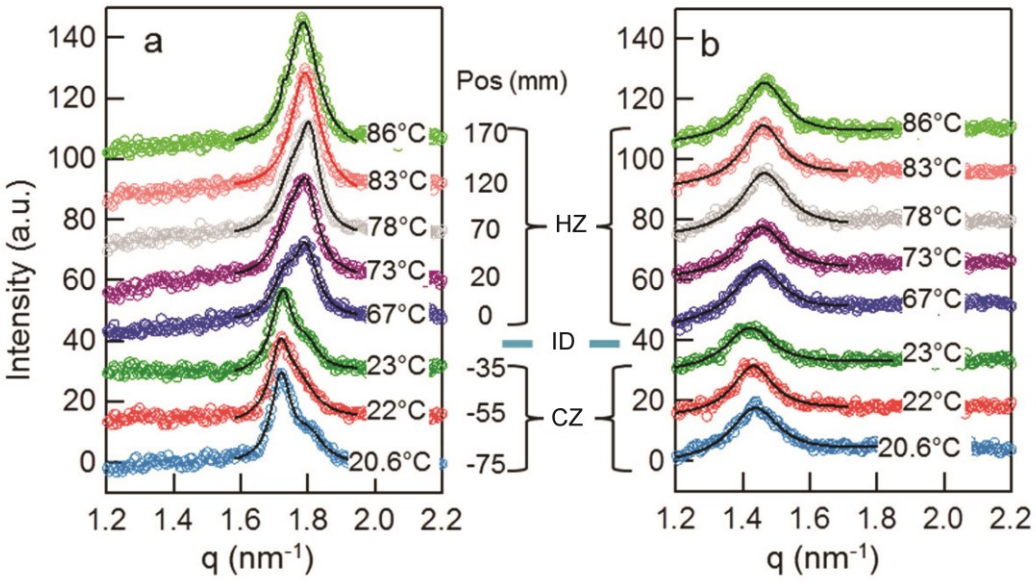

Figure 20: *Comparison between in situ SAXS data obtained from (a) ethanol-rich solution (solution E in Table 2) and (b) water-rich solution (solution A in Table 2) at set positions, corresponding to different temperatures, in the reaction chamber. HZ=heating zone; ID=insulating disc; CZ=Cold Zone. The patterns have been shifted vertically for clarity. Solid lines show the best fit of the curves. The aerosol temperature is indicated for each position.*

In the ethanol rich solution data, at temperatures below 25°C, a prominent peak at q ~ 1.72 nm^{-1} (d-spacing ~ 3.65 nm) and a second peak at q ~1.80 nm^{-1} (d-spacing ~ 3.49 nm) are visible; moving into the heating zone at a temperature higher than 70°C, the 1.72 nm^{-1} peak disappears, while the intensity of the 1.80 nm^{-1} peak increases (Figure 20a). Under the same temperature and humidity conditions, water-rich data show a single peak at q ~1.44 nm^{-1}, corresponding to a d-spacing of 4.35 nm in the cold zone. The peak shifts to q ~1.46 nm^{-1} corresponding to a d-spacing of 4.30 nm in the heating zone, indicating a decrease of the d spacing of 0.05 nm.(Figure 20b). The decrease of the d-spacing as the temperature increases along the reaction chamber is consistent with previously reported results [62].

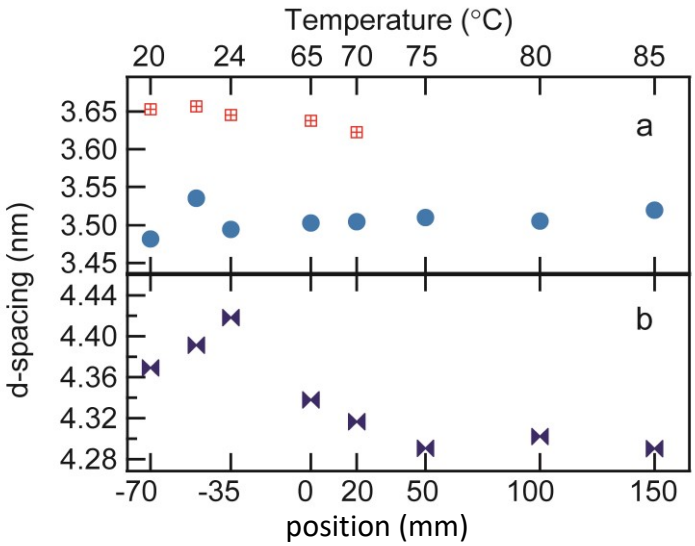

***Figure 21**: d-spacing of nanoparticles calculated from the two peaks visible in the scattering curves obtained in situ at different positions along the temperature gradient of the reaction chamber (shown in Figure 20) for (a) ethanol-rich solution, and (b) water rich solution. The corresponding temperatures at each position is shown in the top axis.*

Figure 21 shows the respective d-spacing calculated from the scattering data at each position for ethanol rich (top) and water rich solutions (bottom) respectively. Figure 22 shows the calculated peak area for the two reflections of the ethanol rich solution.

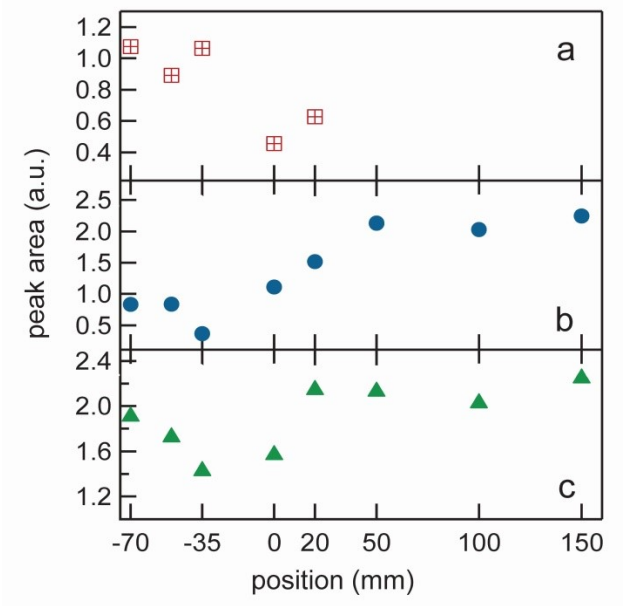

***Figure 22**: Calculated areas of the 1.72 nm^{-1} (a) and 1.8 nm^{-1} (b) peaks from the ethanol rich solution. (c) Sum of the two peaks areas.*

When a phase separation occurs, the volume fraction of each phase is correlated to the calculated area of the respective scattering peak [73]. In our case, the peak area decreases for the 1.72 nm^{-1} peak, and increases for the 1.8 nm^{-1} peak along the temperature gradient. The sum of the two respective areas is approximately constant throughout the reaction chamber, indicating the evolution from one phase to another.

To investigate the effect of the evaporation rate of the solvents keeping the solution composition constant, the experiment was repeated with the ethanol-rich solution, increasing the temperature (90°C, 170°C, 270°C respectively) in the heating zone.

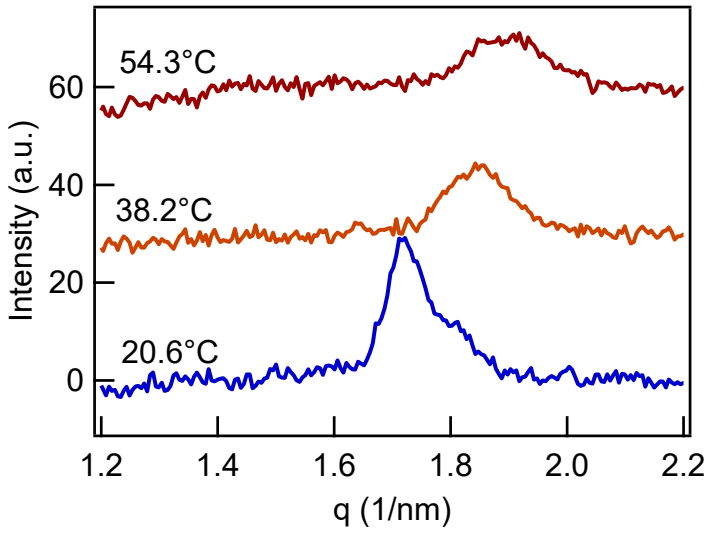

Figure 23*: In situ scattering data recorded from the aerosol of ethanol-rich solution in the cold zone of the reaction chamber. The heating zone was set at three different temperatures (bottom to top, 90°C, 170°C and 270°C respectively). The SAXS patterns were recorded at the same position in the reaction chamber ensuring the same resident time of the aerosol at the moment of data collection (for clarity patterns are shifted vertically).*

Despite the insulating disc, as a consequence of the heat transfer the temperature of the cold zone increased. Figure 23 shows the scattering data obtained from *in situ* measurements at the same position in the cold zone, but at increasing temperatures: a higher temperature accelerates the evaporation of the solvents, leading to the formation of a single peak with lower mesostructural order as measured by the width of the scattering

peak (Figure 24). The same effect on the mesostructural order is visible in the heating zone (data not shown). The d-spacing decreases slightly as the temperature increases, as expected from previous experiments with ethanol-rich solutions [33].

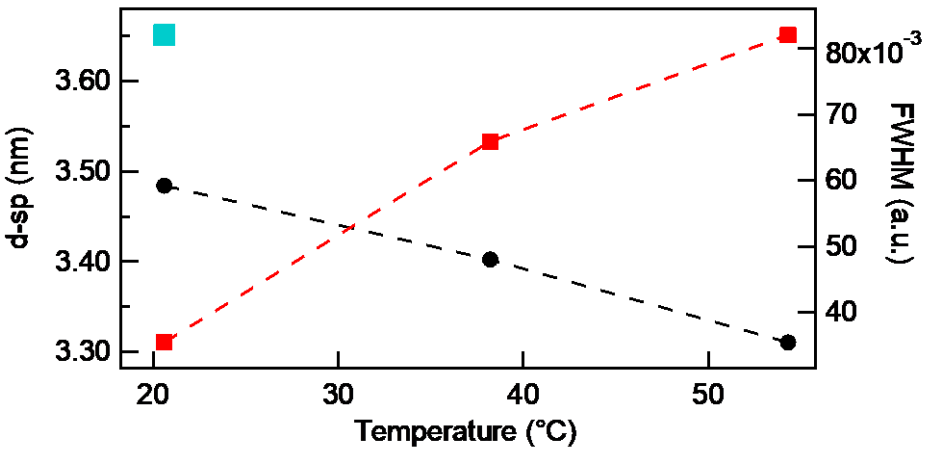

Figure 24 *Peak positions (circles) and FWHM (squares) derived from data fitting at three temperatures. The square in the inset indicates the d-spacing of the second peak.*

The influence of the two solvents on the inner nanostrucure of the formed particles is shown in figure 25. The *in situ* EISA experiment was conducted setting the heating zone temperature to 90°C, changing the EtOH to H_2O molar ratio while keeping the silica and surfactant composition constant. Each scan was repeated 5 times, to investigate the effect of the aging of the solutions on the mesostructure. The duration of each scan was 630 s.

The data show that the lattice parameters of the silica nanoparticles change with the solvent ratios; at low temperature, solutions with high ethanol content (1 : 1 and higher) present two overlapping peaks, while mixtures with high water content show only one reflection in the cold zone .

The peak position shift also depends on the ethanol content, with larger d-spacing for higher EtOH to H_2O ratio. The mesostructure did not show significant lattice changes during the 5 scans.

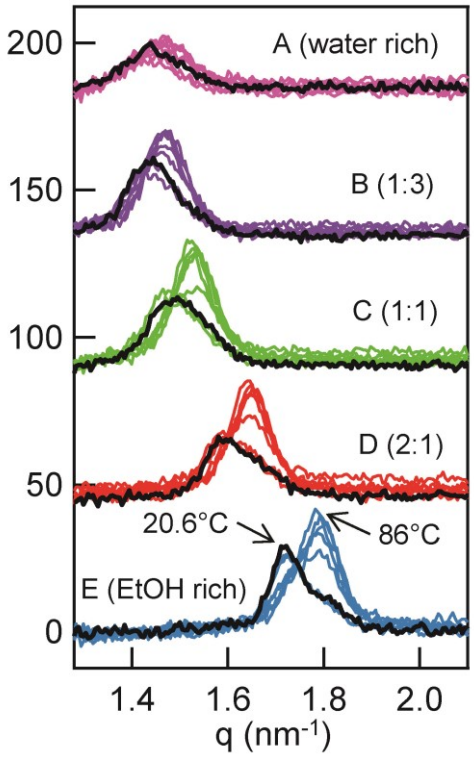

***Figure 25**: Scattering data collected along the reaction chamber from aerosol of solutions with different EtOH:H_2O molar ratio. The data corresponding to the -70mm position, 20.6°C, is shown by the black, thicker line. At low temperature, higher ethanol content solutions lead to the formation of two peaks, indicating the presence of separated mesophases. The d-spacing of the mesophase increases with the water content.*

Figure 26 shows the calculated d-spacing of different EtOH to H_2O molar ratio in the cold zone and in the last position of the heating zone. For these 2-solvents systems, the *in situ* data show that the pore size decreases linearly with the ethanol content.

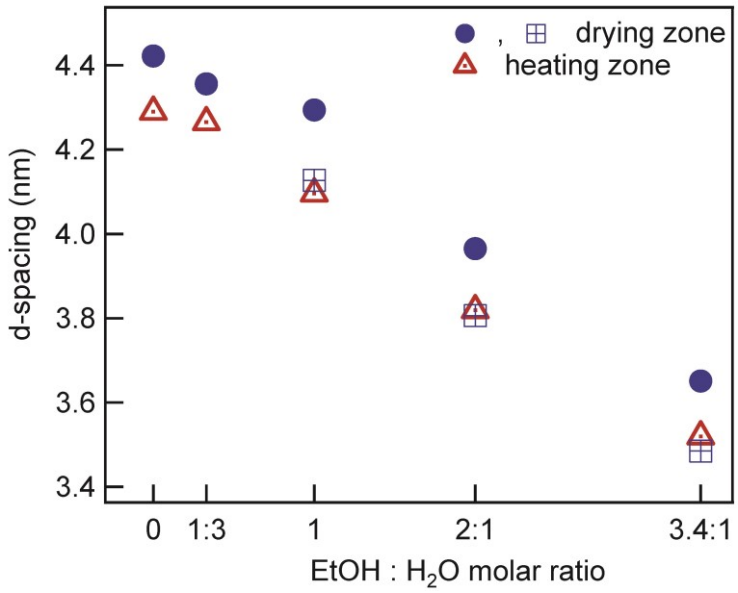

Figure 26: *Hexagonal (100) d-spacings obtained from in situ SAXS in the experiments with varying EtOH to H_2O molar ratio. Measurements were carried out in the cold zone , at 20.6°C (full circles and open squares indicate the two coexisting peaks corresponding to two different mesophases), and in the heating zone, at 86°C (open triangles).*

The SAXS analysis on the powders collected at the end of the furnace confirmed that the solvent molar ratio allows to tune the pore size of the nanoparticles: with increasing water content the d-spacing grows from ~3.5 to ~4.3 nm.

For a detailed structural analysis on the collected powders, the SAXS data were fitted according to the two-density model described previously [61], which takes into account the high electron density of the silica shell and the lower one of the CTAB core. SAXS analysis of the collected powders show that when the water content in the precursor solution is higher, nanoparticles with a larger unit cell are produced: the core shell radius *R* does not show significant changes, but the silica shell thickness Δ increases.The structural parameters obtained for the different two solvents compositions are summarized in table 3.

***Table 3**: Structural parameters of the collected powders at different water to ethanol molar ratio*

sample	*a*(nm)	*R* (nm)	Δ (nm)	*A* (nm²)
A	4.630	1.396 ± 0.09	1.838	12.444
B	4.794	1.358 ± 0.01	2.079	14.113
C	4.654	1.437 ±0.047	1.779	12.266
D	4.422	1.407 ±0.083	1.608	10.720
E	4.051	1.372 ±0.082	1.307	8.300

a = unit cell parameter; R = core shell radius; Δ silica shell thickness; A = unit cell cross sectional area

TEM analysis on the collected powders allowed us to determine the morphology and size distribution of the nanoparticles, as well as to visualize their internal structure (Figures 27, 28, 29). The images confirmed the presence of well ordered, hexagonal mesostructure in all the analyzed samples, in agreement with previously reported SAXS results.

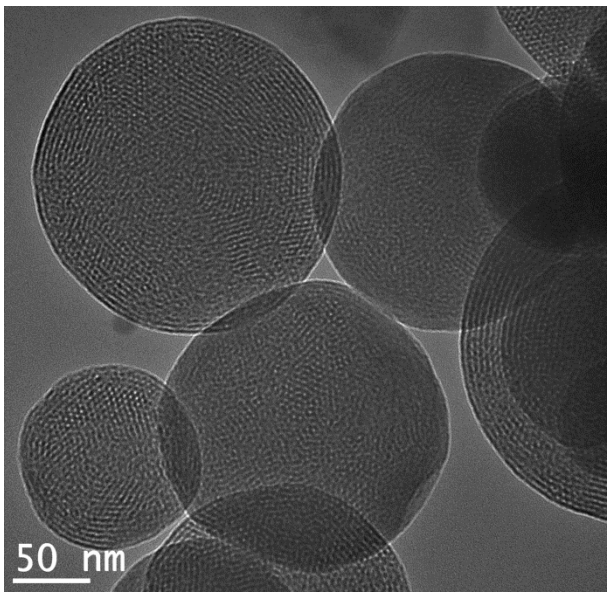

***Figure 27:** TEM of mesostructurerd nanoparticles obtained from water-rich precursor solution. The temperature of the heating zone was set to 90°C, and the nanoparticles were successively calcined at 450°C for 5 hrs.*

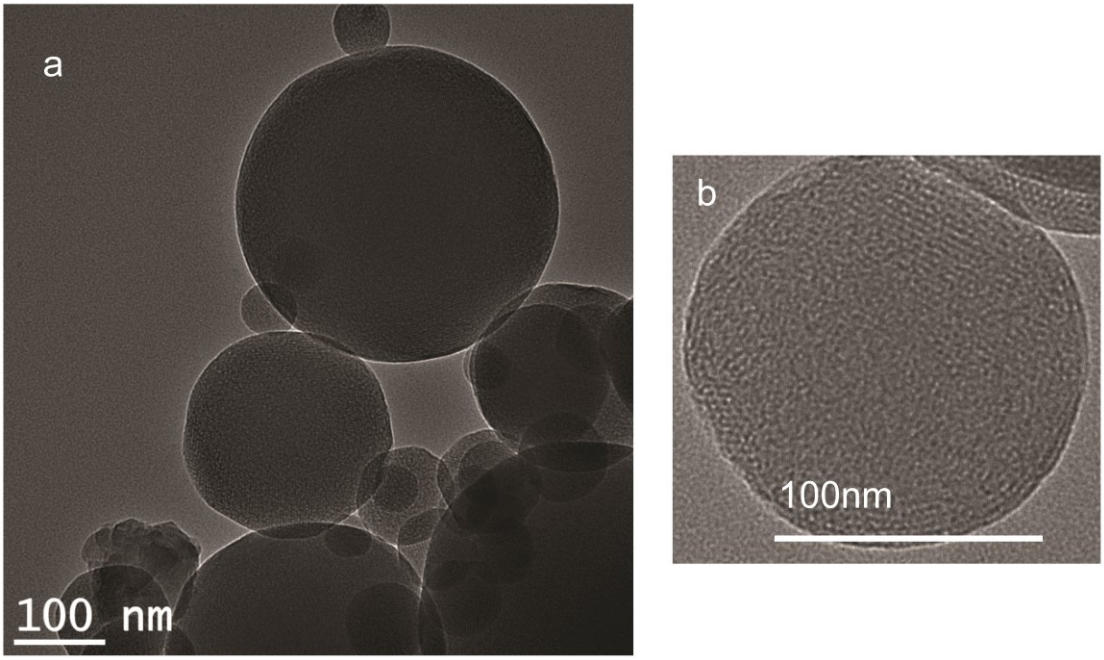

Figure 28: *a) TEM of mesostructurerd nanoparticles obtained from ethanol-rich precursor solution. b), detail of one nanoparticle. The molar ratio between ethanol and water in the procursor solution was 3.4:1. The temperature of the heating zone was set to 100°C, and the nanoparticles were successively calcined at 450°C for 5 hrs to remove the surfactant.*

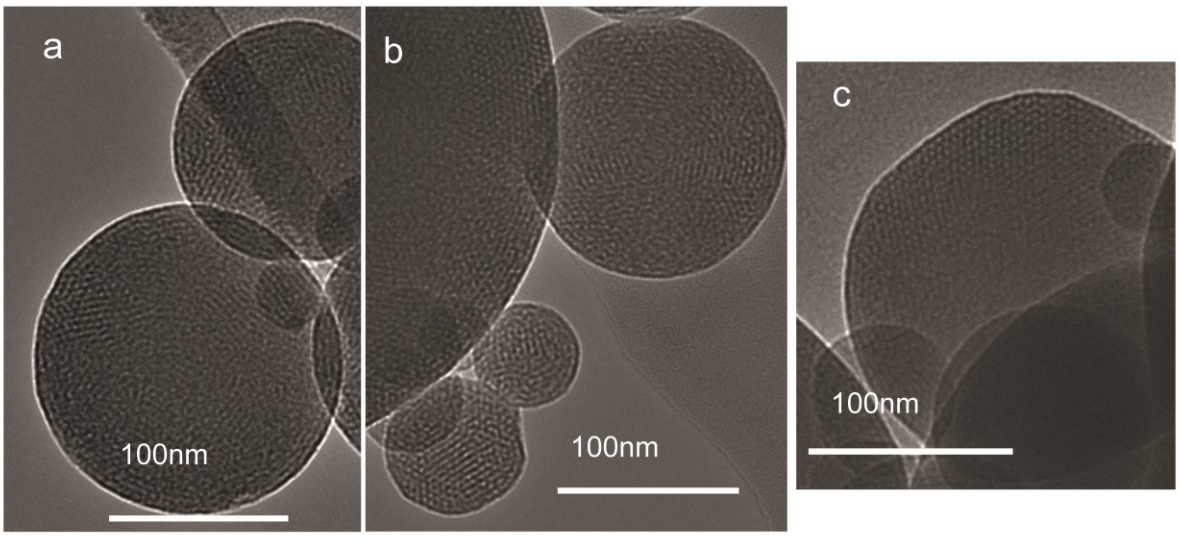

Figure 29: *TEM images of collected powders, produced from precursor solution with different molar ratio between solvents. The temperature in the reaction chamber was set to 90°C for all samples. The nanoparticles were not calcined. EtOH : H_2O molar ratio for a), b), c) are 1:3, 1:1, 2:1 respectively.*

The structural analysis of the powders collected at the end of the reaction chamber (*ex situ* deposited) showed a correlation between the solvent molar ratio and the mesostructure parameters. Although the CTAB core radius remained approximately constant for all the solutions studied, the silica shell thickness and the unit cell cross sectional area decreased when the relative amount of ethanol increased.

As confirmed by both SAXS and TEM, a higher amount of water in the initial solution led to the formation of a better ordered mesostructure: the (210) reflection of the hexagonal phase wass not visible in powders produced from solution **E** (Figure 30). The better order achievable, as well as the different silica thickness obtained from water enriched solutions can be explained with the faster evaporation of the more volatile solvent, that reduces the time available for the silica molecules to organize in a well ordered structure.

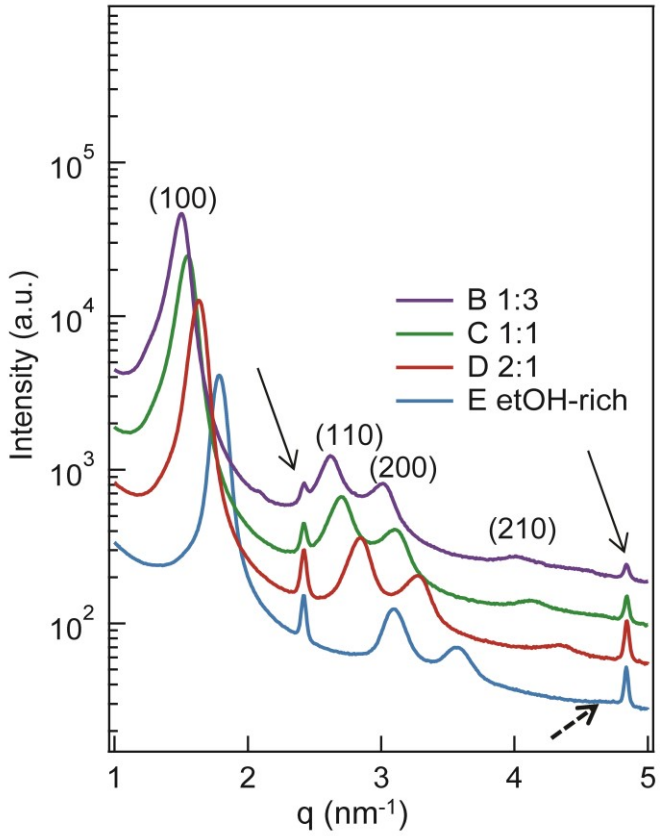

Figure 30: *SAXS scattering data from powders collected at the end of the reaction chamber obtained from different solvents composition (ethanol:water molar ratio) solutions. The temperature of the heating chamber was set to 90°C. The two black arrows indicate the peaks due to the crystals of CTAB. Dotted line indicates the expected position of the (210) reflection in solution* ***E****. Data are shifted vertically for clarity.*

The dynamics of the evaporation of aerosol microdrops has been explained previously with theoretical models for single solvent [74] and for multi-solvent systems [75]. According to these works, the condensation of the mesostructure during the EISA process is diffusion controlled. In a CTAB/TEOS system the evaporation of the solvent increases the concentration of the precursors at the droplet/air interface, creating a concentration gradient toward the droplet centre. Consequently, the Critical Micelles Concentration (CMC) is reached at the droplet surface first. Thus, the silica mesostructures are formed from outside towards the centre of the droplet [11].

Bearing this process in mind, we explain our results with the simultaneous presence of two separated silica mesostructures in the evaporating aerosol droplets, as evidenced by the two reflections in the scattering data (Figure 20a). The high intensity of the 1.72 nm^{-1} peak at low temperature suggests that most of the condensed material is in an intermediate ordered phase formed along the radial surfactant gradient as the solvents evaporate. The weaker scattering intensity of the 1.8 nm^{-1} peak indicates that part of the silica and surfactant are organized in a second ordered structure.

We note, that this 2-phase organization is present only at the beginning of the droplet evaporation if the water content is below a certain amount, and only if the first steps of the EISA process inside the reaction chamber take place at low (room) temperature (Figure 23). Our interpretation is that these conditions cause a solvent demixing in the aerosol droplet: at the beginning the vapour pressure of water in the cold zone of the reaction chamber is in equilibrium with the liquid droplet, so almost no water evaporation occurs. This does not apply for ethanol, whose vapour pressure is higher at the same temperature. As previously mentioned, ethanol plays an important role in the organization of the surfactant molecules, shielding its hydrophobic tails from the water molecules and favouring the interdigitation of the hydrocarbon chains of CTAB[30], thus, promoting the formation of an ordered lamellar phase that evolves into a hexagonal phase, as observed in thin films for similar silica-surfactant systems. From the reported results[27], the calculated d-spacing ratio between the lamellar (L) and the hexagonal (H) phases corresponds to L/H = 1.03, while from our data, the calculated d-spacing ratio L/H = 1.04. This suggests that in the aerosol EISA process a structural evolution similar to the one observed in thin films takes place, in much shorter time. We postulate that in the first stages of condensation, the evolving mesostructure in

the droplet is lamellar (ethanol-rich condition), although only the mixture of the two first order reflections of the coexisting lamellar (strong peak) and hexagonal (weak peak) phases are visible in our SAXS data. The evolution of the lamellar and hexagonal peak area further supports the hypothesis of a phase coxistence during solvent evaporation: in the cold part of the reaction chamber, the area of the lamellar and hexagonal peak decreases and increases respectively, reflecting the evolution of the transient lamellar structure in the final hexagonal one. From the results obtained from ethanol-rich solution when the temperature of the heating chamber was set to 90°C, in the first position in the heating zone, at 65°C, the sum of the two peak areas corresponds to the area calculated for the (100) reflection of the hexagonal lattice (Figure 22): in these conditions, the solutes are condensed into the two ordered mesostructures, although they are not locked: as the nanodrops move along the heating zone of the reaction chamber, the surfactant reorganizes, and the lamellar phase disappears.

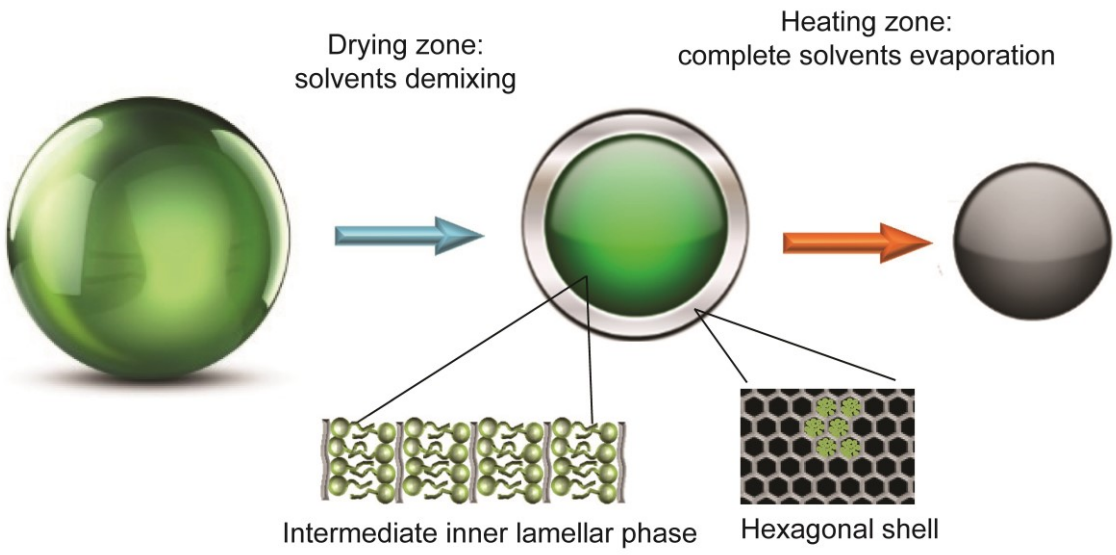

Figure 31: *Sketch of the proposed evaporation –driven evolution of the mesostructure*

The proposed mechanism for the mesostructure evolution is shown in figure 31. Ethanol evaporates more quickly than water from the droplet surface, inducing the formation of an intermediate water-rich phase close to the air/droplet interface. In the water-enriched layer, the interaction of the hydrophobic tails of CTAB with water induces the formation of a 2D hexagonal mesophase. At the same time, inward the droplet the solutes form a lamellar

intermediate. During this transient period both mesostructures are permeable to the solvents and thus, as the evaporation proceeds, the hexagonal phase becomes more and more prominent at the expense of the lamellar phase, which vanishes as the TEOS and CTAB condense into their final state. These observations are in agreement with previous SAXS studies on EISA on thin films[27], where a first, transient lamellar phase was visible at the very beginning of the film organization. It is then possible to assume that, even if it was not visible in our measurements due to the setup design, just after the aerosol nozzle a transient lamellar phase is formed at the droplets surface: it evolves into the hexagonal phase almost immediately as the solvents demixing starts.

At higher temperatures the evaporation of ethanol is too fast, so that this phase separation cannot be observed anymore. The d-spacing of the hexagonal phase is slightly larger during the early stages of the mesostructure formation. This is consistent with the behaviour observed in silica thin films, where the phase transition from lamellar to hexagonal in response to the reorientation of the surfactant hydrophobic tails to minimize their contact with the water-rich silica solution, is accompanied by an increase of the d-spacing[76]. The subsequent decrease in the lattice spacing is thought to be due to a denser chain packing. In fact, when ethanol evaporates, the interaction of the water molecules with the surfactant induces its hydrophobic chains to stretch, thus reducing the curvature of the micelles. But as evaporation proceeds, the lower water content induce the chains to shorten again, the curvature of the micelles increase, and the d-spacing decreases. When water is the only solvent, we also observe a slightly larger lattice of the mesostructure at the beginning of the evaporation process, and then a slight decrease in the d-spacing along the temperature gradient (Figure 20).

We assume that the hexagonal phase grows according to the same mechanism in both the water-rich and in the ethanol-rich solution, but in the latter case the evaporating ethanol sets the conditions for the formation of an intermediate, ordered phase. From the data shown in figure 23, we can see that if the temperature in the cold zone exceeds 38°C, only a single reflection corresponding to the (100) of the 2D hexagonal phase is visible. These results agree with the notion that at temperatures higher than 25°C, both solvents quickly evaporate in a single step since the beginning, so that the surfactant molecules do not have

enough time to organize differently at the surface and along the radial concentration gradient [77].

Changing the respective ethanol and water ratio in the solution allowed us to investigate *in situ* how the presence of ethanol influences the mesostructure formation. Increasing the water content up to a 1 : 1 molar ratio, at room temperature the presence of two scattering peaks confirms the formation of an intermediate lamellar phase. The lamellar to hexagonal d-spacing ratio is approximately constant (Figure 21), suggesting that the lamellar and the hexagonal mesostructure coexist during the drying process, as described above for the ethanol-rich solution. At high water content (EtOH/H_2O 1:3) only one reflection corresponding to the 2D hexagonal phase is visible. In this case, the system behaviour is the same as observed when water is the only solvent. We therefore hypothesize that when water is the major constituent of the solvent mixture, the number of ethanol molecules present in the outer shell of the droplets is too low to avoid the interaction between the hydrophobic tails of the surfactant and water, and this inhibits the formation of an intermediate lamellar phase.

5. CONCLUSIONS AND OUTLOOK

Understanding the mechanism behind the formation of hierarchically structured mesoporous material is of great importance, for their design and subsequent utilization.

However, despite the big effort made to develop new, effective and economically attractive synthetic paths for the production of size- and shape-controlled mesoporous nanoparticles, the number of parameters involved remain a challenge when it comes to optimize a design strategy. Thus, every step forward to a deeper understanding of the condensation process represents an improvement and can help in the rational design of tailored mesostructured material.

In situ study of aerosol supported EISA of silica nanoparticles allows to investigate the evolution of the mesostructure from the sol-gel precursor, during the evaporation of solvents which drive the material condensation.

At the moment when this work was started, no studies were perfomed to study *in situ* the evaporation induced self assembly of mesoporous silica in the gas phase. SAXS has already proven to be an excellent tool to study the architecture of mesostructured nanoparticles produced via spray-drying, but the material had to be collected and characterized *ex situ*, thus losing all the details of the condensation mechanism.

We designed and built an aerosol generator based on a low cost mist maker. We first demonstrated the working principle by vaporizing a suspension of gold nanoparticles: the stable nanoparticles solution was carried by a gentle gas flow directly from the aerosol generator to a windowless observation cell for SAXS measurements. We thus demonstrated that the particle density obtained from our in-house built system was sufficient to perform succesful SAXS measurement in the gas phase.

Following these positive results, we integrated an efficient temperature controlled dryer chamber in the setup, and placed the observation cell at the end of it. We studied the condensation of mesoporous silica nanoparticles changing the temperature of the dryer and/or the carrier gas flowrate, tracking the evolution of the nanostructure in dependance on the temperature and on the resident time inside the dryer. The particles size distruibution was determined by Scanning Electron Microscopy observation, and the details

of the nanostructures were revealed by SAXS measuremets on the nanoparticles deposited at the end of the dryer. Further improvement of the setup, namely the use of a commercial apparatus for aerosol production, the design of a new dryer with a horizontal slit to perform *in situ* SAXS measurements along the whole evaporation path, and the introduction of a cold zone at the beginning of the dryer, thermally isolated from the hot zone to equilibrate the microdroplets before evaporation, allowed us to study *in situ* the influence of several parameters: we changed the surfactant/silica molar ratio, the relative humidity and residence time of the aerosol inside the dryer varying the flowrate of the carrier gas, the evaporation temperature, the solvents composition. The nanoparticles were measured *in situ* with SAXS along the dryer, and collected for more detailed structural analysis with SEM and TEM.

The main findings reported in the papers in the Appendix can be summarized as follows:

- An optimal surfactant silica molar ratio to obtain a well ordered mesostructure exist, and our findings (CTAB/TEOS = 0.14) go along with with those reported in previous studies [43]. The optimal temperature for the synthesis of well ordered mesostructured material is lower than 100°C, suggesting that slowing down the process improves the condensation. Low residual humidity in the mesostructure keeps the silica network flexible for several hours after collection, letting the superstructure adjust to a stable low energy configuration for a longer time. Thanks to this effect, a well ordered mesostructure can be obtained also at CTAB/TEOS ratio different from the optimal.

- At high temperature, significant differences in the structural parameters are induced only by changes in the surfactant/silica composition. The lattice spacing remains constant also in the collected powder, and this demonstrate that the fast evaporation somehow locks the structure, contrary to what happens at low temperature.

- The solvents evaporation rate influences the mesostructure: at constant CTAB/TEOS molar ratio, changes in the solvents composition induce changes in the lattice spacing. The pore size increase with the increasing of the less volatile solvent.

- In two-solvents systems, an intermediate, ordered lamellar phase develops in the first stages of evaporation during the silica condensation. This transient phase evolves into a well

ordered hexagonal phase as the evaporation proceeds, and is the result of the solvents demixing at the surface of the microdroplets.

SAXS is recognized as a state-of-the-art characterization technique for nano-assembly in solution: in a broader context, one of the main topics underlined by this thesis is that SAXS addresses the need for an effective tool to elucidate the condensation process of mesostructured material also in the gas phase.

In the last 10 years, several studies were published, that show how this technique can be employed for aerosol characterization: Sinha and coworkers[78] used SAXS to validate their theoretical model of the dynamic of formation and growth of H_2O/D_2O droplets in a supersonic nozzle. SAXS experiments provided a mean to estimate directly the width of size distribution, the mean radius and the total number density of droplets in the aerosol.

Recently, the dynamics of silica nanoparticles growth in a methane/oxygen flame doped with hexamethyldisiloxane was probed *in situ* by Beaucage and colleagues, using synchrotron radiation SAXS[79]; Wang and coworkers studied i*n situ* with SAXS the decomposition of a molecular organopalladium precursor (Palladium acetate) in nanoparticles during combustion in an acetilene flame[80]. In both cases, the particle size distribution could be determined at different positions in the flame (i.e, at different residence time at high temperature).

In a scanning experiment with a micro-focused X-ray beam on a single droplet of silica colloidal dispersion, Sen and coworkers demonstrated how SAXS can be used to follow the evolution of a gradient of silica nanoparticles in an evaporating droplet [81]. This experiment allowed to develop a theoretical model which describes the distribution of the volume fraction of the nanoparticles in two zones inside the droplets during evaporation, namely a hollow core, and a surrounding denser shell. This model proposes a three stages time dependent evolution of nanoparticles diffusion, which may be used to predict the evolution of the viscosity inside the microdroplets, a useful parameter for nanostructured nanoparticles produced via spray drying.

These studies delivered informations on the size, shape and aggregation state of nanoparticles synthesized in the gas phase. The work described in this thesis goes beyond it,

using SAXS to give an insight on the mechanism of molecular condensation. The low concentration of nanoparticles in the gas phase samples represents a challenge for scattering tecniques. Nevertheless, we demonstrated that it is feasible to characterize even low amounts of material during condensation, and the accuracy of our measurements was confirmed by the results obtained on the collected material.

LIST OF ABBREVIATIONS AND SYMBOLS

MCM41	Mobil Composition of Matter
SAXS	Small Angle X-ray Scattering
SEM	Scanning Electron Microscopy
TEM	Transmission Elecron Microscopy
TEOS	Tetraethyl Ortosilicate
CTAB	Cetyltrymethylammonium Bromide
HCl	Hydrochloric Acid
CMC	Crytical Micelles Concentration
EISA	Evaporation Induced Self Assembly
$\rho(r)$	Electron density
I(q)	Scattering intensity
P(q)	Form factor
S(q)	Structure factor
p(r)	Pair distribution function
q	Scattering vector
d	Lattice spacing
I(q)	Scattering intensity
Rg	Radius of gyration
FWHM	Full Width Half Maximum
a	Unit cell parameter
R_1	Core radius
Δ	Silica wall thickness
A_Δ	Silica cross sectional area

REFERENCES

(1) Boissiere, C.; Grosso, D.; Chaumonnot, A.; Nicole, L.; Sanchez, C. Aerosol route to functional nanostructured inorganic and hybrid porous materials. *Adv. Mater.* **2011**, *23* (5), 599–623 DOI: 10.1002/adma.201001410.

(2) Faustini, M.; Boissière, C.; Nicole, L.; Grosso, D. From chemical solutions to inorganic nanostructured materials: A journey into evaporation-driven processes. *Chem. Mater.* **2014**, *26* (1) DOI: 10.1021/cm402132y.

(3) Fratzl, P.; Weinkamer, R. Nature's hierarchical materials. *Prog. Mater. Sci.* **2007**, *52* (8), 1263–1334 DOI: 10.1016/j.pmatsci.2007.06.001.

(4) Ge, M.; Rong, J.; Fang, X.; Zhang, A.; Lu, Y.; Zhou, C. Scalable preparation of porous silicon nanoparticles and their application for lithium-ion battery anodes. *Nano Res.* **2013**, *6* (3), 174–181.

(5) Orlova, B. I. N.; Kargapolova, I.; Kuchyanov, A.; Shelkovnikov, V.; Plekhanov, A. Optical Sensors Based on Opal Film and Silica Nanoparticles Modified with a Functional Dye. In *Advances in Chemical Sensors*; Wang, P. W., Ed.; InTech, 2012.

(6) Vallet-Regí, M. Mesoporous Silica Nanoparticles: Their Projection in Nanomedicine. *ISRN Mater. Sci.* **2012**, *2012*, 1–20 DOI: 10.5402/2012/608548.

(7) Chiola, V.; Ritsko, J. E.; Vanderpool, C. D. . US Patent No. 3 556 725, 1971.

(8) Kresge, C. T.; Leonowicz, M. E.; Roth, W. J.; Vartuli, J. C.; Beck, J. S. Ordered mesoporous molecular sieves synthesized by a liquid-crystal template mechanism. *Nature* **1992**, *359* (6397), 710–712 DOI: 10.1038/359710a0.

(9) Avnir, D. Braun, S. Lev, O. Ottolenghit, M. Enzymes and Other Proteins Entrapped in Sol-Gel Materials. *Chem. Mater.* **1994**, *6* (12), 1605–1614.

(10) Jain, T. K.; Roy, I.; De, T. K.; Amarnath, M. Nanometer silica particles encapsulating active compounds: a novel ceramic drug carrier. *J. Am. Chem. Soc* **1998**, *120*, 11092–11095.

(11) Jiang, X.; Jiang, Y.-B.; Liu, N.; Xu, H.; Rathod, S.; Shah, P.; Brinker, C. J. Controlled Release from Core-Shell Nanoporous Silica Particles for Corrosion Inhibition of

Aluminum Alloys. *J. Nanomater.* **2011**, *2011*, 1–10 DOI: 10.1155/2011/760237.

(12) Sahoo, N. G.; Abbas, A.; Li, C. M. Micro/Nanoparticle Design and Fabrication for Pharmaceutical Drug Preparation and Delivery Applications. *Curr. Drug ther.* **2008**, *3* (2), 78–97.

(13) Rosenholm, J. M.; Gulin-Sarfraz, T.; Mamaeva, V.; Niemi, R.; Özliseli, E.; Desai, D.; Antfolk, D.; von Haartman, E.; Lindberg, D.; Prabhakar, N.; et al. Prolonged Dye Release from Mesoporous Silica-Based Imaging Probes Facilitates Long-Term Optical Tracking of Cell Populations In Vivo. *Small* **2016**, n/a-n/a DOI: 10.1002/smll.201503392.

(14) Mercier, T. L.; Pinnavia, T. J. Access in Mesoporous Materials: Advantages of a Uniform Pore Structure in the Design of a Heavy Metal Ion Adsorbent for Environmental Remediation. *Adv. Mater.* **1997**, *9* (6), 500–503.

(15) Cai, Q.; Luo, Z.; Pang, W.; Fan, Y.; Chen, X.; Cui, F. Dilute Solution Routes to Various Controllable Morphologies of MCM-41 Silica with a Basic Medium. *Chem. Mater.* **2001**, *13* (2), 258–263.

(16) Fowler, C. E.; Khushalani, D.; Lebeau, B.; Mann, S. Nanoscale Materials with Mesostructured Interiors. *Adv. Mater.* **2001**, *13* (9), 649–652.

(17) Nooney, R. I.; Thirunavukkarasu, D.; Chen, Y.; Josephs, R.; Ostafin, A. E. Synthesis of Nanoscale Mesoporous Silica Spheres with Controlled Particle Size. *Chem. Mater.* **2002**, No. 17, 4721–4728.

(18) Zhao, D.; Feng, J.; Huo, Q.; Melosh, N.; Fredrickson, G. H.; Chmelka, B. F.; Stucky, G. D. Triblock Copolymer Syntheses of Mesoporous Silica with Periodic 50 to 300 Angstrom Pores. *Science (80-.).* **1998**, *279* (5350), 548–552 DOI: 10.1126/science.279.5350.548.

(19) Slowing, I. I.; Vivero-Escoto, J. L.; Trewyn, B. G.; Lin, V. S.-Y. Mesoporous silica nanoparticles: structural design and applications. *J. Mater. Chem.* **2010**, *20* (37), 7924 DOI: 10.1039/c0jm00554a.

(20) Chu, B.; Liu, T. Characterization of nanoparticles by scattering techniques. *J. Nanoparticle Res.* **2000**, *2* (1), 29–41 DOI: 10.1023/A:1010001822699.

(21) Chen, Z. H.; Kim, C.; Zeng, X. B.; Hwang, S. H.; Jang, J.; Ungar, G. Characterizing size

and porosity of hollow nanoparticles: SAXS, SANS, TEM, DLS, and adsorption isotherms compared. *Langmuir* **2012**, *28* (43), 15350–15361 DOI: 10.1021/la302236u.

(22) Edler, K. J.; Reynolds, P. A.; White, J. W. Small-Angle Neutron Scattering Studies on the Mesoporous Molecular Sieve {MCM-41}. *J. Phys. Chem. B.* **1998**, *102* (19), 3676–3678.

(23) Brunauer, S.; Emmett, P. H. Gases i n Multimolecular Layers. **1936**, *407* (1) DOI: citeulike-article-id:4074706\rdoi: 10.1021/ja01269a023.

(24) Barret, E. P.; Joyner, L. G.; Halenda, P. The determination of pore volume and area distributions in porous substances. I. Computations from nitrogen isotherms. *J. Am. Chem. Soc* **1951**, *73*, 373–380 DOI: 10.1021/ja01145a126.

(25) McCool, B.; Murphy, L.; Tripp, C. P. A simple FTIR technique for estimating the surface area of silica powders and films. *J. Colloid Interface Sci.* **2006**, *295* (1), 294–298 DOI: 10.1016/j.jcis.2005.08.010.

(26) Grosso, D.; Babonneau, F.; Albouy, P. A.; Amenitsch, H.; Balkenende, A. R.; Brunet-Bruneau, A.; Rivory, J. An in situ study of mesostructured CTAB-silica film formation during dip coating using time-resolved SAXS and interferometry measurements. *Chem. Mater.* **2002**, *14* (2), 931–939 DOI: 10.1021/cm011255u.

(27) Grosso, D.; Babonneau, F.; Soler-Illia, G. J. D. A. A.; Albouy, P.-A.; Amenitsch, H. Phase transformation during cubic mesostructured silica film formation. *Chem. Commun.* **2002**, No. 7, 748–749 DOI: 10.1039/b111499a.

(28) Khodakov, A. Y.; Zholobenko, V. L.; Impéror-Clerc, M.; Durand, D. Characterization of the initial stages of SBA-15 synthesis by in situ time-resolved small-angle X-ray scattering. *J. Phys. Chem. B* **2005**, *109* (48), 22780–22790 DOI: 10.1021/jp052786z.

(29) Boissiere, C.; Grosso, D.; Amenitsch, H.; Gibaud, A.; Baccile, N.; Sanchez, C. First in-situ SAXS studies of the mesostructuration of spherical silica and titania particles during spray-drying process. *Chem. Commun. (Camb).* **2003**, No. c, 2798–2799.

(30) Doshi, D. A.; Gibaud, A.; Liu, N.; Sturmayr, D.; Malanoski, A. P.; Dunphy, D. R.; Chen, H.; Narayanan, S.; MacPhee, A.; Wang, J.; et al. In-Situ X-ray Scattering Study of Continuous Silica-Surfactant Self-Assembly during Steady-State Dip Coating. *J. Phys. Chem. B* **2003**, *107* (31), 7683–7688 DOI: 10.1021/jp027214i.

(31) Amenitsch, H. Marmiroli, B. Time-resolved structure investigation with small angle X-ray scattering using scanning techniques. *Rend. Lincei* **2011**, *22* (SUPPL 1), S93–S107.

(32) Amenitsch, H.; Rappolt, M.; Kriechmabum, M.; Mio, H.; Laggner, P.; Bernstorff, S. First performance assessment of the Small Angle X-Ray Scattering beamline at ELETTRA. *J. Synchrotron Radiat.* **1998**, *5*, 506–508.

(33) Shyjumon, I.; Rappolt, M.; Sartori, B.; Amenitsch, H.; Laggner, P. Novel in situ setup to study the formation of nanoparticles in the gas phase by small angle x-ray scattering. *Rev. Sci. Instrum.* **2008**, *79* (4), 43905 DOI: 10.1063/1.2908436.

(34) Hench, L. L.; West, J. K. The Sol-Gel Process. *Chem. Rev.* **1990**, *90*, 33–72.

(35) Brinker, C. J.; Scherer, G. W. *Sol-Gel Science The physics and chemistry of sol-gel processing*; Academic Press, I., Ed.; Elsevier B.V., 1990.

(36) Sanchez, C.; Rozes, L.; Ribot, F.; Laberty-Robert, C.; Grosso, D.; Sassoye, C.; Boissiere, C.; Nicole, L. "Chimie douce": A land of opportunities for the designed construction of functional inorganic and hybrid organic-inorganic nanomaterials. *Comptes Rendus Chim.* **2010**, *13* (1–2), 3–39 DOI: 10.1016/j.crci.2009.06.001.

(37) Brinker, C. J.; Lu, Y.; Sellinger, A.; Fan, H. Evaporation-Induced Self-Assembly: Nanostructures Made Easy. *Adv. Mater.* **1999**, *11* (7), 579–585 DOI: 10.1002/(SICI)1521-4095(199905)11:7<579::AID-ADMA579>3.3.CO;2-I.

(38) Lu, Y.; Fan, H.; Stump, A.; Ward, T.; Rieker, T.; Brinker, C. J. Aerosol-assisted self-assembly of mesostructured spherical nanoparticles. *Nature* **1999**, *398*, 223–226.

(39) Colbeck I., L. M. *Aerosol Science: Technology and Applications*; John Wiley & Sons, Ed.; 2014.

(40) Calvo, A. I.; Alves, C.; Castro, A. et al. Research on aerosol sources and chemical composition: past, current and emerging issues. *Atmos. Res.* **2012**, *120–121*, 1–28.

(41) Husar R.B. *Atmospheric aerosol science before 1900*; Preining O., and D. E., Ed.; 2000.

(42) Okuyama, K.; Lenggoro, W. W. Preparation of nanoparticles via spray route. *Chem. Eng. Sci.* **2003**, *58* (3–6), 537–547 DOI: 10.1016/S0009-2509(02)00578-X.

(43) Bore, M. T.; Rathod, S. B.; Ward, T. L.; Datye, A. K. Hexagonal mesostructure in

powders produced by evaporation-induced self-assembly of aerosols from aqueous tetraethoxysilane solutions. *Langmuir* **2003**, *19* (2), 256–264 DOI: 10.1021/la020704h.

(44) Wyslouzil, B.; Cheung, J.; Wilemski, G.; Strey, R. Small Angle Neutron Scattering from Nanodroplet Aerosols. *Phys. Rev. Lett.* **1997**, *79* (3), 431–434 DOI: 10.1103/PhysRevLett.79.431.

(45) Pauw, B. R. Everything SAXS: small-angle scattering pattern collection and correction. *J. Phys. Condens. Matter* **2014**, *26* (23), 239501 DOI: 10.1088/0953-8984/26/23/239501.

(46) Guinier, A. No TitleStructure of Age-Hardened Aluminium-Copper alloys [2]. *Nature* **1938**, *142*, 569–570.

(47) Als-Nielsen J., M. D. *Elements of Modern X-Ray Physics.pdf*; 2001.

(48) Feigin, L. A. and Svergun, D. I. *Structure Analysis by Small-Angle X-Ray and Neutron Scattering*; George W. Taylor, Ed.; Plenum Press, 1987.

(49) Glatter, O.; Kratky, O. *Small Angle X-ray Scattering*; 1982.

(50) Pedersen, J. S. Analysis of small-angle scattering data from colloids and polymer solutions: modeling and least-squares fitting. *Adv. Colloid Interface Sci.* **1997**, *70*, 171–210 DOI: 10.1016/S0001-8686(97)00312-6.

(51) Dünkel, L. *Fundamentals of crystallography*; Oxford University Press, Ed.; 1992.

(52) Zhang, F.; Ilavsky, J.; Long, G. G.; Quintana, J. P. G.; Allen, A. J.; Jemian, P. R. Glassy carbon as an absolute intensity calibration standard for small-angle scattering. *Metall. Mater. Trans. A Phys. Metall. Mater. Sci.* **2010**, *41* (5), 1151–1158 DOI: 10.1007/s11661-009-9950-x.

(53) Kikhney, A. G.; Svergun, D. I. A practical guide to small angle X-ray scattering (SAXS) of flexible and intrinsically disordered proteins. *FEBS Lett.* **2015**, *589* (19), 2570–2577 DOI: 10.1016/j.febslet.2015.08.027.

(54) Roessle, M. Basics of X-ray Scattering - EMBO Course 2012, 2012.

(55) Aroyo M.I.,Muller U., W. H. Historical Introduction. In *International Tables for Crystallography*; Springer, 2006; pp 2–5.

(56) Rappolt, M.; Amenitsch, H.; Strancar, J.; Teixeira, C. V.; Kriechbaum, M.; Pabst, G.; Majerowicz, M.; Laggner, P. Phospholipid mesophases at solid interfaces: In-situ X-ray diffraction and spin-label studies. *Adv. Colloid Interface Sci.* **2004**, *111* (1–2 SPEC. ISS.), 63–77 DOI: 10.1016/j.cis.2004.07.004.

(57) Harper, P. E.; Mannock, D. A.; Lewis, R. N. A. H.; McElhaney, R. N.; Gruner, S. M. X-ray diffraction structures of some phosphatidylethanolamine lamellar and\ninverted hexagonal phases. *Biophys J* **2001**, *81* (November), 2693–2706 DOI: 10.1016/S0006-3495(01)75912-7.

(58) Warren, B. E. *X-ray Diffraction.*; Addison-Wesley, Ed.; Reading, MA, 1969.

(59) Beurroies, I.; Agren, P.; G., B.; Rosenholm, J. B.; Amenitsch, H.; Denoyel, R.; Linden, M. Detailed in situ XRD and calorimetric study of the formation of silicate/mixed surfactant mesophases under alkaline conditions. Influence of surfactant chain length and synthesis temperature. *J. Phys. Chem. B* **2006**, *110* (33), 16254–16260 DOI: 10.1021/jp053746y.

(60) Rappolt, M.; Hickel, A.; Bringezu, F.; Lohner, K. Mechanism of the Lamellar/Inverse Hexagonal Phase Transition Examined by High Resolution X-Ray Diffraction. *Biophys. J.* **2003**, *84* (5), 3111–3122 DOI: 10.1016/S0006-3495(03)70036-8.

(61) Imperor-Clerc, M.; Davidson, P.; Davidson, A. Existence of a microporous corona around the mesopores of silica-based SBA-15 materials templated by triblock copolymers. *JACS* **2000**, *122* (48), 11925–11933.

(62) Shyjumon, I.; Rappolt, M.; Sartori, B.; Cacho-Nerin, F.; Grenci, G.; Laggner, P.; Amenitsch, H. Mesostructured silica aerosol particles: comparison of gas-phase and powder deposit X-ray diffraction data. *Langmuir* **2011**, *27* (9), 5542–5548 DOI: 10.1021/la104892s.

(63) Turkevich, J.; Stevenson, P. C.; Hillier, J. A Study of the Nucleation and Growth Processes in the Synthesis of Colloidal Gold. *Discuss. Faraday Soc.* **1951**, *11* (c), 55–75 DOI: 10.1039/DF9511100055.

(64) Oster, G.; Riley, D. P. Scattering from cylindrically symmetric systems. *Acta Crystallogr.* **1952**, *5*, 272–276 DOI: 10.1107/S0365110X5200071X.

(65) Dourdain, S.; Rezaire, A.; Mehdi, A.; Ocko, B. M.; Gibaud, A. Real time GISAXS study of micelle hydration in CTAB templated silica thin films. *Phys. B Condens. Matter* **2005**, *357* (1–2 SPEC. ISS.), 180–184 DOI: 10.1016/j.physb.2004.11.052.

(66) Israelachvili, J. N.; Mitchell, D. J.; Ninham, B. W. Theory of self-assembly of hydrocarbon amphiphiles into micelles and bilayers. *J. Chem. Soc. Faraday Trans. 2* **1976**, *72*, 1525 DOI: 10.1039/f29767201525.

(67) Liu, M.; Sheu, H.; Cheng, S. Anion-Exchange Induced Phase Transformation of Mesostructured Silica. **2009**, No. 17, 3998–4005.

(68) Jungnikl, K.; Rappolt, M.; Shyjumon, I.; Sartori, B.; Laggner, P.; Amenitsch, H. Aerosol flow reactor with controlled temperature gradient for in situ gas-phase X-ray experiments - Measurements of Evaporation Induced Self Assembly (EISA) in aerosols. *Aerosol Sci. Technol.* **2011**, *45*, 795–800.

(69) Campanelli, A. R.; Scaramuzza, L. Hexadecyltrimethylammonium bromide. *Acta Crystallogr. Sect. C* **1986**, *C42* (I), 1380–1383 DOI: 10.1107/S0108270186092193.

(70) Klotz, M.; Ayral, A.; Guizard, C.; Cot, L. Synthesis conditions for hexagonal mesoporous silica layers. *J. Mater. Chem.* **2000**, *10* (3), 663–669 DOI: 10.1039/a906181i.

(71) Innocenzi, P.; Falcaro, P.; Grosso, D.; Babonneau, F. Order−Disorder Transitions and Evolution of Silica Structure in Self-Assembled Mesostructured Silica Films Studied through FTIR Spectroscopy. *J. Phys. Chem. B* **2003**, *107* (20), 4711–4717 DOI: 10.1021/jp026609z.

(72) A. P. Hammersley. FIT2D: An Introduction and Overview. *ESRF Intern. Report, ESRF97HA02T* **1997**.

(73) Hamley, I. W. Developments in block copolymer science and technology. *Mater. Today* **2004**, *7* (6), 53 DOI: 10.1016/S1369-7021(04)00291-3.

(74) Bandyopadhyay, A. Pawar, A. Venkataraman, C. Mehra, A. Modelling size and structure of nanoparticles formed from drying of submicron solution aerosols. *J. Nanoparticle Res.* **2015**, *17* DOI: 10.1007/s11051-014-2842-z.

(75) Homer, C. J.; Jiang, X.; Ward, T. L.; Brinker, C. J. Measurements and simulations of the near-surface composition of evaporating ethaol-water droplets. *Phys. Chem. Chem.*

Phys. **2009**, *11* (36), 7759 DOI: 10.1039/b916865f.

(76) Doshi, D. a.; Gibaud, A.; Goletto, V.; Lu, M.; Gerung, H.; Ocko, B.; Han, S. M.; Brinker, C. J. Peering into the self-assembly of surfactant templated thin-film silica mesophases. *J. Am. Chem. Soc.* **2003**, *125* (38), 11646–11655 DOI: 10.1021/ja0295523.

(77) Jiang, X.; Ward, T. L.; Swol, F. Van; Brinker, C. J. Numerical Simulation of Ethanol - Water - NaCl Droplet Evaporation. *Ind. Eng. Chem. res* **2010**, *49*, 5631–5643.

(78) Sinha, S.; Wyslouzil, B. E.; Wilemski, G. Modeling of H 2 O/D 2 O Condensation in Supersonic Nozzles. *Aerosol Sci. Technol.* **2009**, *43* (1), 9–24 DOI: 10.1080/02786820802441771.

(79) Beaucage, G.; Kammler, H. K.; Mueller, R.; Strobel, R.; Agashe, N.; Pratsinis, S. E.; Narayanan, T. Probing the dynamics of nanoparticle growth in a flame using synchrotron radiation. *Nat. Mater.* **2004**, *3* (6), 370–373 DOI: 10.1038/nmat1135.

(80) Wang, J.; Seifert, S.; Winans, R. E.; Tolmachoff, E.; Xin, Y.; Chen, D.; Wang, H.; Anderson, S. L. In situ X-ray Scattering and Dynamical Modeling of Pd Catalyst Nanoparticles Formed in Flames. *J. Phys. Chem. C* **2015**, *119* (33), 19073–19082 DOI: 10.1021/acs.jpcc.5b01226.

(81) Sen, D.; Bahadur, J.; Mazumder, S.; Santoro, G.; Yu, S.; Roth, S. V. Probing evaporation induced assembly across a drying colloidal droplet using in situ small-angle X-ray scattering at the synchrotron source. *Soft Matter* **2014**, *10* (10), 1621–1627 DOI: 10.1039/c3sm52039k.

6. PUBLICATIONS

A. Novel in situ setup to study the formation of nanoparticles in the gas phase by small angle X-ray scattering

I. Shyjumon, M. Rappolt, B. Sartori, H. Amenitsch,a and P. Laggner

Institute of Biophysics and Nanosystems Research, Austrian Academy of Sciences, Graz A-8042, Austria

Received 28 November 2007; accepted 24 March 2008; published online 18 April 2008

Abstract

An in-house built aerosol generator setup for *in situ* gas phase studies of aerosol and nanoparticles is described. The aerosol generator with an ultrasonic ceramic disk mist maker provides high enough particle concentrations for structural gas phase analysis by synchrotron small angle X-ray scattering for water 4x108 droplets/s with a droplet size of 2.5 µm. The working principle was proved by scattering of gold nanoparticles. For evaporation induced self-assembly studies of nanostructured particles, an additional thermal treatment chamber was included in the setup. The first on-line gas phase data with our setup for mesostructured silica particles are presented for different thermal treatments. Scanning electron microscope imaging revealed the average particle size to be 1 µm. Furthermore, to quantify their internal nanostructure, diffraction experiments of deposited silica aerosols were carried out and the corresponding electron density map indicates a silica wall thickness of about 1 nm.

DOI: 10.1063/1.2908436

Introduction

One of the major technological challenges today is the development of novel and improved materials based on the extraordinary physical and chemical properties of nanostructures.[1] Nanoparticles with well defined properties such as size, morphology fractal dimension, and

crystallinity can be used as building blocks to assemble such nanostructured materials and can be used to construct new devices with outstanding properties and functionality.[2] Powders of nanoparticles are frequently produced by gas phase process, namely, by those routes that allow the formation of a two phase mixture of solid particles within a carrier gas.[2,3] The main advantages of aerosol synthesis are the good control of the process parameters and its low cost with respect to other synthesis methods for instance, vacuum techniques.[4] Both physical size, concentration, crystal growth, agglomeration, porosity and chemical stoichiometry, surface state properties of the resulting products can be easily controlled.[3] A supplemental approach is the growth of mesostructured particles, i.e., particles of micron and submicron sizes with internal porous structures in the nanometer range, the evaporation induced self-assembly EISA process.[4–6] This technique is based on the surfactant mediated structuring mechanism and highly ordered mesostructured particles can be produced with a few seconds of process time.[5,7] Such aerosol generated particles find application in high end technologies such as drug delivery, cosmetics, catalysis, separation, semiconductor devices, fire-retarding materials, gas sensing, and energy conversion photovoltaic and fuel cells.[4,8–11]

There are several methods available for the investigation of the postdeposited nanoparticles, such as microscopic imaging of the deposited samples.[1,12,13] Sparsely deposited wafers can be used to determine particle size distributions, for instance, with scanning electron microscopy SEM, while higher amounts of postdeposited particles can be used to study their internal nanostructure by X-ray diffraction. Note, however, that true particle sizes cannot be measured in collected bulk material due to the strong particle aggregation during deposition. Directly studying the nanoparticles in the gas phase using synchrotron small angle X-ray scattering[14–17] SAXS circumvents this problem and addresses the basic formation and structuring processes. Nevertheless, only a few experiments have been performed so far with *in situ* SAXS.[4,14,18,19] The limiting factor is the particle concentration in the gas phase, which is usually very low e.g., for a commercial apparatus 10^7 particles equivalent to 6 g dry matter per cm^3.[4] In this letter, we describe a novel in-house built aerosol generator that sufficiently produces high particle concentrations for *in situ* SAXS. Our first aim is to make *in situ* gas phase studies on nanoparticle formation. Then

we carry out EISA of mesostructured aerosol particles during subsequent on-line temperature treatment.

Aerosol apparatus and Gas Phase Setups

1. Aerosol generator

Among the commercially available aerosol generators which give high particle concentrations, we decided to use an in-house built aerosol generator based on an economical mist maker following the previous work, which is described in Refs. 20 and 21. Our concept and design allow complete control of all working parameters. The working principle of an ultrasonic mist maker is the generation of ultrasonic waves by a piezoelectric disk placed under the surface of the solution. These waves drive the solution surface to form tiny peaks. After gaining enough energy from the ultrasonic waves, these tiny peaks break off from the surface forming droplets. The ultrasonic nebulizer produces a narrow size distribution of the droplets.[21]

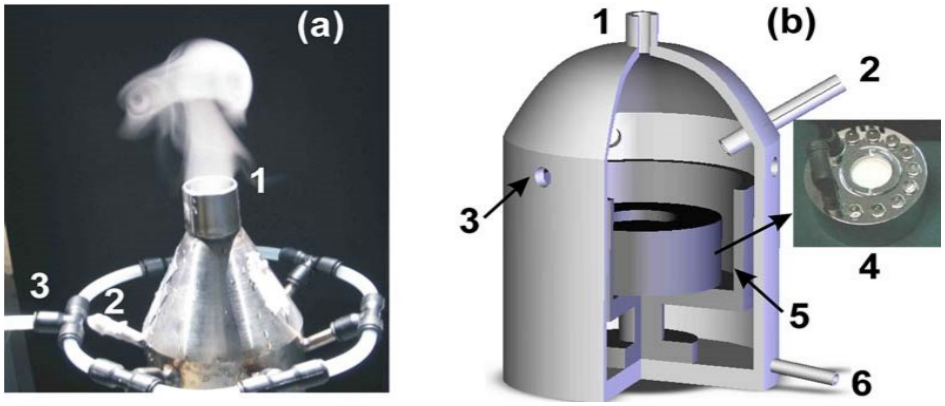

Fig. 1. *Aerosol generator. On the left side (a), a photo of the working fog generator is shown; its design is explained in a three dimensional 3D schematic. (b) 1, outlet; 2, liquid inlet; 3, gas inlet; 4, mist maker (see also small photo); 5, mist maker container; 6, liquid outlet.*

The heart of the aerosol generator is the low cost ultrasonic ceramic disk mist maker (type SL-24 from Foshan Nanhai Techsin Electronic Co. Ltd, China) working at 1.7 MHz that is shown in Fig. 1 (4). A ring gas inlet system (3) is used above the mist maker container (5), which efficiently en routes the fog to the outlet with minimal turbulence and condensation. An AD 41 dry air unit (Oxford Cryosystems, Oxford, UK) is used for inlet air supply with a typical flow rate of 5 SLM standard liter per minute. An automated refill system was installed consisting of two peristaltic pumps, one pumping in the solution (connected to the liquid

inlet, 2) from a reservoir of the aerosol mother solution to the mist maker container, and the other one collecting the spilled solution from the bottom of the aerosol vessel (liquid outlet, 6). The automated refill system enables the undisturbed operation of the aerosol generator for hours.

In order to quantify the evaporation rate of the aerosol generator, cold trap experiments (at −50 °C) with pure water were carried out off-line. In good agreement with the manufacturer information, the microscopically estimated droplet diameter is about 2.5 μm. The effective averaged evaporation rate at the end of the transfer line of our aerosol generator was measured to be 14 ml/h, which refers to $4x10^8$ droplets/s, which is about one order of magnitude higher than for commercial aerosol generators.[4]

For the *in situ* study of nanoparticles, the setup using the fog generator is shown in Fig. 2 with the only difference that the dryer was not used. For the gas phase analysis of nanoparticles, the outlet of the fog generator was directly connected to a windowless SAXS cell, which was equipped with an exhaust system for the removal of the fog after the sample cell.

For the EISA studies of mesostructured aerosol particles, a temperature treatment chamber (dryer) was included after the aerosol generator, as shown in Fig. 2. The dryer is composed of a quartz tube, 1 m long and 36 mm inner diameter, which is wrapped with heater tape (Omega Engineering Inc., Stamford, CT), and can be heated up to 300 °C. The temperature of the dryer is controlled by a custom built control unit with a GEFRAN 1020 configurable two loop temperature controller (GEFRAN Elettronica S.p.A, Italy). The temperature profile and the uniformity in the dryer were determined with a Pt100 thermoresistor. At the entrance (and exit), the temperature exponentially rises with a length constant, λ =8 cm, which corresponds to a time rise constant of 1.1 s at 5 SLM flow. The temperature gradient was measured across the diameter of dryer tube, i.e., at 200 °C the difference between the temperature at the center and at the wall of the dryer, respectively, was ~1 °C after a stabilization time of few minutes. Heating temperatures between 125 and 250 °C are routinely required depending on the aerosol system.[9,22]

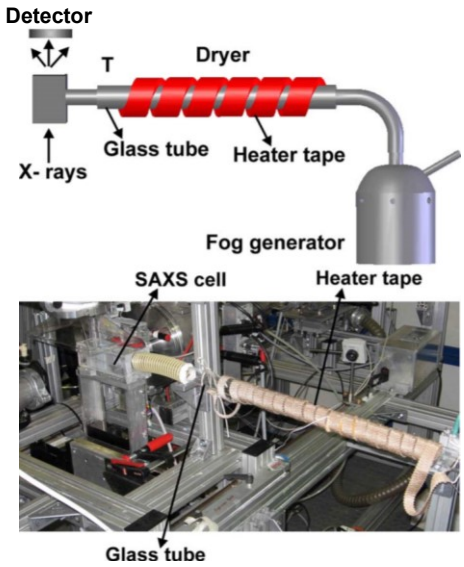

Fig. 2. *In situ setup for the gas phase analysis of nanoparticles and the EISA study of aerosol particles. At the top, a 3D schematic of the setup is illustrated and below a photo of the setup at the Austrian SAXS beamline is shown.*

2. Synchrotron SAXS and SEM

The synchrotron X-ray measurements were carried out at the Austrian high flux SAXS beamline of the 2 GeV electron storage ring ELETTRA Trieste, Italy.[23,24] A one dimensional linear position sensitive Gabriel detector was used,[25] which covered the interested *q*-range from about $2\pi/330$ to $2\pi/15$ $Å^{-1}$ at a photon energy of 8 keV which corresponds to a wavelength λ of 0.154 nm, with $q=4\pi\sin\theta/\lambda$, where 2θ is the scattering angle. The calibration of the angular scale of diffraction pattern was done with silver behenate [CH_3–$(CH_2)_{20}$–COOAg, *d* spacing of 58.38 Å].[26]

The SEM images were acquired using a Zeiss Supra 40 instrument (Carl Zeiss MicroImaging GmbH, Germany), using the secondary electrons as the measuring signal. The accelerating field for the primary electrons was set at 1.2 keV, so the actual nanoparticle surface could be scanned without any covering conductive layer.

Results and discussion

1. Aerosol particle scattering

To demonstrate the feasibility of our setup for aerosol or nanoparticle studies in the gas phase, we carried out experiments with Au nanoparticles synthesized by the citrate route

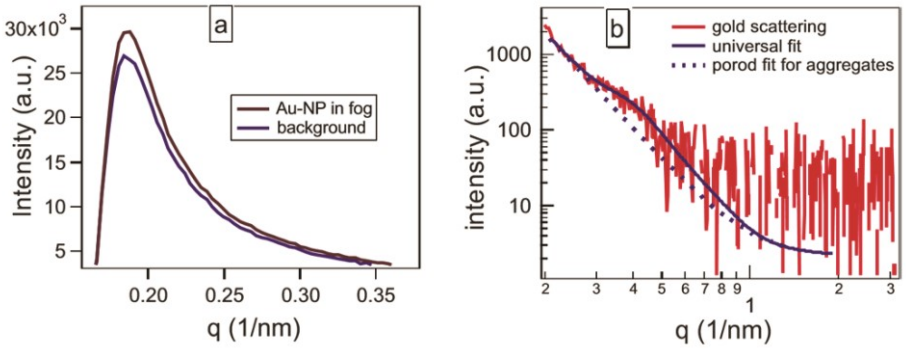

Fig. 3. *Scattering data of gold nanoparticles. (a) Scattering raw data of Au particles and background. (b) Reduced data together with a universal fit, which gives R_g ~25 nm for gold nanoparticles in the fog.*

($2.510^{-4}M$ $HAuCl_4$+34 mM sodium citrate, purchased from Sigma-Aldrich, Italy). Spherical gold nanoparticles were produced with a size of about 5–10 nm, which was confirmed by laboratory solution scattering SAXS experiment (R_g ~ 5 nm data not shown). These stable gold nanoparticles in solution were directly carried by the fog with a flow rate of 5 SLM to the windowless SAXS cell, i.e., the scattering data of the droplets containing gold nanoparticles were recorded *in situ* for an exposure time of 240 s.

Fig. 3(a) shows the scattering raw data of gold nanoparticles with and without fog background. Fig. 3(b) gives the background subtracted data together with a universal fit (simultaneous Guinier and Porod fits) for individual particles and an additional Porod contribution for large aggregates.

The fitting function is given in Eq. (1), according to Beaucage[16,17]

$$I_{(q)} = G\ exp\left(-q^2R_g^2/3\right) + B\left\{\frac{1}{q}\left[erf\left(qR_g/\sqrt{6}\right)\right]^3\right\}^p + \left(p_c/q^{p_e}\right) + C \qquad (1)$$

where *G* is the Guinier prefactor, *B* is a prefactor specific to the type of power-law scattering, *p* is the Porod exponent for individual particles, p_c and p_e are the Porod coefficient and Porod exponent for the aggregates and *C* is the offset. The fit results in a Radius of Gyration R_g of about 25 nm, which when compared to the gold nanoparticle radius (R_g ~ 5 nm) is about five times larger.

Thus particle aggregation occurred when the particles were trapped in the fog droplets. Assuming that the gold concentration in the initial bulk suspension and in the droplet is the same, we have calculated the number of Au nanoparticles per droplet. Furthermore, it turned out that the volume ratio of one aggregate to an individual nanoparticle is just the same (~125), i.e., all the Au nanoparticles in each droplet form only one aggregate of $R_g \sim 25$ nm. The aggregation is therefore clearly induced by the confinement inside the droplet. If the droplets in the aerosol are considered as microreactors,[20] our experiment also demonstrates the possibility for measuring *in situ* the nucleation and growth of nanoparticles in aerosol microreactors.

2. Formation of mesoporous aerosol particles by EISA

A very promising approach for the production of mesostructured particles is EISA. As an example, we demonstrate how to produce and investigate silica aerosols online. The aerosols were produced from a precursor solution using our aerosol generator. A standard solution prepared containing cetyltrimethylammonium bromide (CTAB), tetraethyl orthosilicate (TEOS), water, and HCl (Sigma Aldrich) with molar ratio, CTAB:TEOS:H_2O:HCl-0.14:1:41:0.13 (water rich).[4] The surfactant to inorganic ratio is the key factor that determines the final mesostructure. Mesoporous materials with well ordered hexagonal structures can be obtained at CTAB-Si ratios in the range of 0.09–0.28.[22] The generated aerosol droplets with the CTAB-TEOS (solution aging ~ 1 h) was carried by air at a flow rate of 5 SLM to the dryer, which corresponds to a mean residence time in the dryer of approximately 10 s. Scattering data were recorded by the one dimensional gas detector at the end of the dryer at various temperatures from room temperature up to ~ 250 °C.

Fig. 4(a) shows the first obtained scattering data using our setup for silica aerosol particles in gas phase at different temperatures inside the dryer for an exposure time of 600 s. Fig. 4(b) demonstrates the corresponding shift of the unit cell parameter *a* at different temperatures in the gas. An exponential decay of the *a* spacing is observed with temperature; the structure and ordering are mostly governed by the competition between the rates of evaporation and silica condensation.[22]

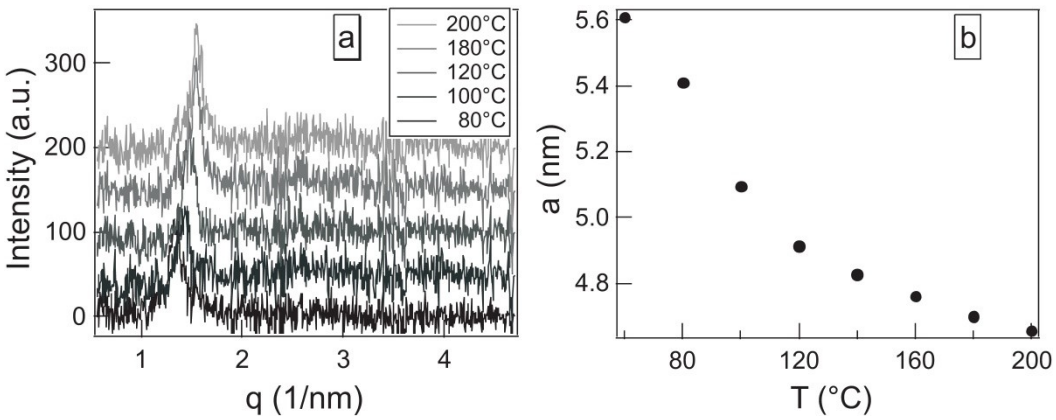

Fig.4*. (a) Scattering data stack plot of silica aerosol in the gas phase at different temperatures, and (b) the evolution of the unit cell parameter a with temperature.*

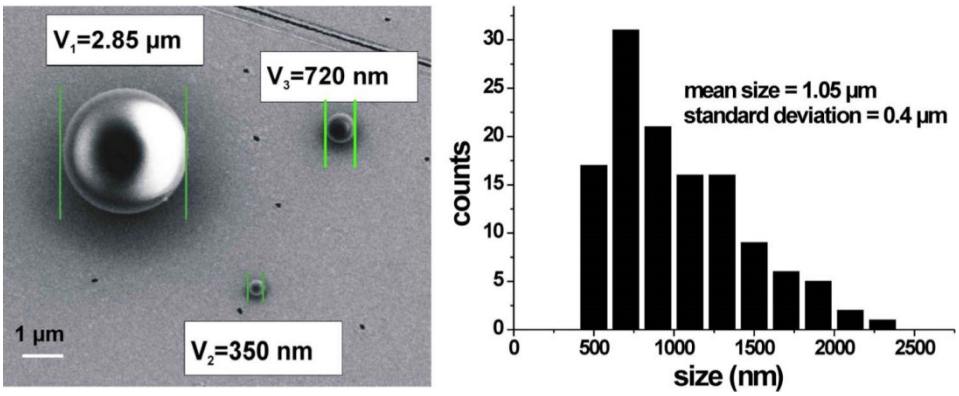

Fig. 5*. SEM image of silica aerosol particles on Si wafer T=150 °C, and the size histogram showing the average size of particles to be 1 m.*

The decay of unit cell parameter *a* with temperature is mainly due to the core CTAB shrinkage. Fig. 5 is a representative SEM image of the aerosol particles deposited on a Si wafer for a relatively short time 20 s to trace the individual particle size of solid matter per droplet. The average size of aerosol particle was determined to be ~1 µm.

For the structure determination of mesostructured silica particles, these particles were deposited on a thin polyethylene terephtalate film for a longer time (~ 2 h) and diffraction data were obtained from these deposits. Please note that the true particle size cannot be determined well from highly dense deposited samples; however, due to the measured amount of scattering material, the signal to noise ratio is greatly enhanced (compare

diffraction patterns of Fig. 6 to Fig. 4), and hence allows the determination of the electron density map (inset of Fig. 6). Irrespective if measured in the gas phase or in deposited particles, under identical chemical conditions, the lattice parameter is the same, i.e., *a (*150 °C)=4.78 nm. The electron density was calculated from the integrated peak intensities I_{hk} of the (10), (11), (20), and (21) reflections (using IDL 5.2, Research Systems, Inc., Boulder, CO). Note that in the intensities the multiplicity and Lorentz corrections have been taken into account. The phases have been taken from Ref. 27, i.e., for the given centrosymmetric symmetry of the nanostructure, −1, +1, +1, and −1 were chosen, respectively.

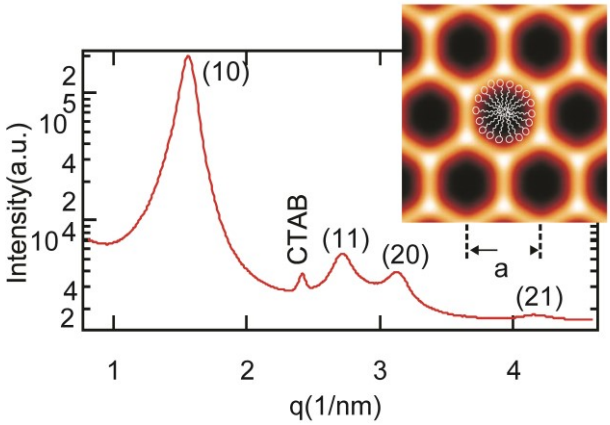

Fig. 6. *Diffraction data for deposited mesostructured silica aerosol particles. The dryer temperature was 150 °C and the CTAB/Si ratio was 0.14. The (10), (11), (20), and (21) reflections of the hexagonal phase of the silica aerosol are indicated together with the reflection from CTAB crystals. The inset illustrates the corresponding electron density map (bright regions indicate the silica matrix and darker the CTAB micellar regions), the unit cell parameter a is indicated at the bottom.*

Fourier series of cosines expresses the electron density contrast $\tilde{\rho}_e(r)$ for the 2D hexagonal phase by[27]

$$\tilde{\rho}_e(r) = \sum_{hk}^{max} \alpha_{hk} \sqrt{I_{hk}} \cos(q_{hk} \cdot r) \qquad (2)$$

where *h,k* are the Miller indices, α_{hk} the phases, and q_{hk} the scattering vector.

From the electron density map, it is estimated that the volume ratio between CTAB and SiO_2 is about 1.5 and the silica wall thickness is ~1 nm. It is also clear that at the given ratio of

CTAB/Si=0.14, and at the given thermodynamic conditions, not all the CTAB molecules have been used to build up the mesostructure. Traces of CTAB were phase separated and crystallized, as seen in Fig. 6. The peak at q=2.4 nm^{-1} compares well to the literature data on pure CTAB crystals (e.g., Ref. 28).

Hence performing SAXS experiment in the gas phase enables us to track the structuring of the particles online and to study the self-assembly processes *in situ*. The properties of fully condensed silica mesostructures can be altered by changing various parameters such as the CTAB/Si ratio, dryer temperature, heating rate, etc.

Conclusions

An aerosol generator has been built in-house using a low cost ultrasonic mist maker that produces at the exit nozzle ~ 4 x 10^8 droplets/s with a size of about 2.5 µm. It has been shown that this is a sufficient particle concentration to carry out gas phase studies with SAXS. As a first approach, the working concept was shown by experiments using gold nanoparticles. Chemical aerosol synthesis and the production of quantum dots are possible future applications of this setup.[20] Second, the setup was extended for the EISA studies of aerosol particles. An efficient dryer including a temperature control system was constructed and used for the production of mesostructured silica particles. The first SAXS data obtained with the silica aerosol particles were presented along with SEM. Performing X-ray diffraction experiments in the gas phase allowed us to track the nanostructural evolution of the particles in dependence of the temperature online. The particle size distribution could be determined with SEM. For further insight into the nanostructure, the diffraction data of deposited particles and the corresponding electron density map were presented. In future experiments, we plan to systematically investigate the influence of different production parameters such as gas flow rate, dryer temperature, and CTAB/Si ratio in greater detail. Further, we have constructed a particle size selector (aerodynamic lens system), which is capable of a size selection in the range of 1–8 µm.[29,30] Including this element in the setup allows us to produce particles with narrow size distributions and thus the microparticle production can be studied in dependence of different droplet sizes, i.e., under different confinement conditions.

Acknowledgments

We wish to acknowledge G. Grenci for the SEM measurements, F. Schmid and F. Cacho for their help with technical drawings and fruitful discussions, C. Morello for the technical support during the construction, and K. J. Ainger for proofreading. The work was supported from the European Union (EU) Design Study "SAXIER" (RIDS 011934).

References

[1] R. G. Agostino, T. Caruso, G. Chiarello, A. Cupolillo, D. Pacile, R. Filosa, V. Formoso, E. Colavita, L. Papagno, C. Ducati, E. Barborini, C. Lenardi, G. Bongiorno, P. Piseri, and P. Milani, Phys. Rev. B 68, 035413 2003.

[2] K. Wegner, P. Piseri, H. V. Tafreshi, and P. Milani, J. Phys. D 3968, 439 2006.

[3] W. J. Stark and S. E. Pratsinis, Powder Technol. 126, 103 2002.

[4] C. Boissiere, D. Grosso, H. Amenitsch, A. Gibaud, A. Coupe, N. Baccile, and C. Sanchez, Chem. Commun. Cambridge 2003, 2798.

[5] Y. F. Lu, H. Y. Fan, A. Stump, T. L. Ward, T. Rieker, and C. J. Brinker, Nature London 398, 223 1999.

[6] C. J. Brinker, Y. F. Lu, A. Sellinger, and H. Y. Fan, Adv. Mater. Weinheim, Ger. 11, 579 1999.

[7] G. V. R. Rao, G. P. Lopez, J. Bravo, H. Pham, A. K. Datye, H. Xu, and T.

L. Ward, Adv. Mater. Weinheim, Ger. 14, 1301 2002.

[8] S. Areva, C. Boissiere, D. Grosso, T. Asakawa, C. Sanchez, and M. Linden, Chem. Commun. Cambridge 2004, 1630.

[9] D. Grosso, G. J. de A. A. Soler-Illia, E. L. Crepaldi, and C. Sanchez, Adv.

Funct. Mater. 13, 37 2003.

[10] D. Grosso, F. Babonneau, P.-A. Albouy, H. Amenitsch, A. R. Balkenende,

A. Brunet-Bruneau, and J. Rivory, Chem. Mater. 14, 931 2002.

[11] A. Corma, Chem. Rev. Washington, D.C. 97, 2373 1997.

[12] T. Caruso, C. Lenardi, T. Mazza, A. Policicchio, G. Bongiorno, R. G. Agostino, G. Chiarello, E. Colavita, P. Finetti, K. C. Prince, C. Ducati, P.

Piseri, and P. Milani, Surf. Sci. 601, 2688 2007.

[13] M. Blomqvist, G. Bongiorno, A. Podesta, V. Serin, G. Abrasonis, U. Kreissig, W. Möller, E. Coronel, S. Wachtmeister, S. Csillag, V. Cassina, P. Piseri, and P. Milani, Appl. Phys. A: Mater. Sci. Process. 87, 767 2007.

[14] G. Beaucage, H. K. Kammler, R. Mueller, R. Strobel, N. Agashe, S. E. Pratsinis, and T. Narayan, Nat. Mater. 3, 370 2004.

[15] W. A. England, Combust. Sci. Technol. 46, 83 1986.

[16] G. Beaucage, J. Appl. Crystallogr. 28, 717 1995.

[17] G. Beaucage, J. Appl. Crystallogr. 29, 134 1996.

[18] S. di Stasio, J. B. A. Mitchell, J. L. LeGarrec, L. Biennier, and M. Wulff, Carbon 44, 1267 2006.

[19] F. Ossler and J. Larsson, J. Appl. Phys. 98, 114317 2005.

[20] Y. T. Didenko and K. S. Suslick, J. Am. Chem. Soc. 127, 12196 2005.

[21] J. Shu, K. R. Wilson, M. Ahmed, and S. R. Leone, Rev. Sci. Instrum. 77, 043106 2006.

[22] M. T. Bore, S. B. Rathod, T. L. Ward, and A. K. Datye, Langmuir 19, 256

2003.

[23] S. Bernstorff, H. Amenitsch, and P. Laggner, J. Synchrotron Radiat. 5, 1215 1998.

[24] H. Amenitsch, M. Rappolt, M. Kriechbaum, H. Mio, P. Laggner, and S.

Bernstoff, J. Synchrotron Radiat. 5, 506 1998.

[25] A. M. Petrascu, M. H. J. Koch, and A. Gabriel, J. Macromol. Sci., Phys. B37, 463 1998.

[26] T. C. Huang, H. Toraya, T. N. Blanton, and Y. J. Wu, J. Appl. Crystallogr.

26, 180 1993.

[27] I. Beurroies, P. Ågren, G. Buchel, J. B. Rosenholm, H. Amenitsch, R.

Denoyel, and M. Linden, J. Phys. Chem. B 110, 16254 2006.

[28] K. J. Edler, T. Brennan, S. J. Roser, S. Mann, and R. M. Richardson, Microporous Mesoporous Mater. 62, 165 2003.

[29] P. Liu, P. J. Ziemann, D. B. Kittelson, and P. H. McMurry, Aerosol Sci. Technol. 22, 193 1995.

B. Mesostructured Silica Aerosol Particles: Comparison of Gas Phase and Powder Deposit X-ray Diffraction Data

I. Shyjumon,[#a] M. Rappolt,[#] B. Sartori,[#] F.Cacho-Nerin, [#] G. Grenci,[‡] P. Laggner,[#] and H. Amenitsch[#*]

[#]Institute of Biophysics and Nanosystems Research, Austrian Academy of Sciences, Schmiedlstr. 6, 8042 Graz, Austria

[‡]CNR-INFM Laboratorio Nazionale TASC, Strada Statale 14, km 163.5, 34012 Basovizza (TS), Italy

[a]Current address: Institute for Synchrotron Radiation, Karlsruhe Institute of Technology, Postfach 3640, D-76021, Germany

Abstract

We report on the characterization of mesostructured aerosol silica particles in the gas phase using *in situ* synchrotron small angle X-ray scattering (SAXS) in order to unveil the influence of the basic production parameters. The investigated system was based on tetraethylorthosilicate (TEOS) as the inorganic precursor, and on cetyltrimethyl-ammonium bromide (CTAB) as the surfactant. The heating temperature, surfactant to silicate ratio and particle flow rate were thoroughly investigated, and for this purpose an in-house built aerosol reactor equipped with a special X-ray observation chamber was used. Complementary fine structural analysis were applied on dried deposits of the silica aerosols comprising direct Fourier transforms as well as simple two-phase model fits. This resulted in robust estimates for the silica wall thickness and surfactant core radius of the hexagonally ordered mesostructure. Particle shape and size distribution were examined by scanning electron microscopy (SEM). The quality of the inner nanostructure was revealed from analysis of the peak width. The comparison of data from the gas phase and powder deposit shows that, in general, slower drying conditions (heating temperature about 80 °C) and medium surfactant to Si ratio (about 0.14) lead to nanostructures of best quality, in terms of well defined long-range organization.

Introduction

Over the last years research on materials with ordered and well defined nanopores has received much attention due to its potential applications in catalysis, separation processes, drug delivery, optics, and nano-devices, to mention a few.[1-4] Such mesostructured materials are prepared by self-assembly processes of organic and inorganic compounds, where the mesoscopically organized organic part acts as structure directing agent for the inorganic phase.[1] Among various methods available today for the synthesis of mesostructured materials the well documented evaporation induced self-assembly (EISA) method[5,6] has been the focus of extensive work. The advantages of the EISA process compared to the other procedures for the synthesis of mesostructured materials are the perfect control over the final stoichiometry and the ability to form different final texture types like thin films, macrospheres and membranes depending on the chosen production route (dip-coating thin films[7] , spray drying macrospheres (aerosol)[6], or slow evaporation methods[8]). The aerosol synthesis of mesostructures has many advantages such as its low cost compared to other methods.[4,6,9,10]

In this respect synchrotron SAXS is a very versatile technique to track the structural changes during the mesophase formation by time-resolved measurements.[7,11,12] In particular *in situ* investigations of mesostructures in the gas phase using SAXS help to understand the individual impact of different process parameters, which can be obscured when only analyzing particles after deposition.[10,12]

Various parameters decide the final mesostructure formed, such as the micellar shape, the relative surfactant concentration, and the nature of the interaction between the organic template and the inorganic oligomers. Although there are many studies published on the formation of various types of mesostructures,[9,10,13-16] it is still of great interest to understand how particle size distribution, porosity and quality of the inner nanostructure can be optimized with spray drying parameters like temperature or evaporation rate. Recording the process directly in the gas phase provide a better insight on the key process parameters and thus to produce tailor made mesostructure with well defined nano-voids. [17–20] However, the limiting factor of *in situ* experiments in the gas phase is the low particle concentration, (i.e. 107 particles equivalent to 6 µg dry matter per cm^3 for a commercial apparatus.[10]) Therefore, we have recently constructed an aerosol generator using an ultrasonic ceramic

disc mist maker that can provide a particle concentration sufficient to carry out *in situ* gas phase measurements of particles using synchrotron SAXS.[20] Here we report on silica mesostructure synthesis in the gas phase using our in-house built aerosol reactor and compare these results to corresponding powder deposit samples.

Several groups reported on the production of mesoscopically structured particles using the aerosol assisted EISA process [6,9,14] resulting in 10-20 µm diameter hollow particles with thin ordered silica walls, and also in compact, nanostructured particles in the sub-micron range.[6,9,14] The later works describe the production of spherical and nearly spherical silica particles with a variety of intriguing inner morphologies such as lamellar, 2D hexagonal, and cubic structures.

Bore et al.[9] reported on the effect of various synthesis parameters on the mesostructure of silica, such as the dryer temperature and the cetyltrimethylammonium bromide (CTAB) to tetraethylorthosilicate (TEOS) ratio. These investigations were carried out on powder products using laboratory X-ray diffraction (XRD) and nitrogen adsorption. Nevertheless, direct monitoring of structural parameters helps to further understand the production processes.[10,11] In this paper we show how gas phase investigations of silica mesostructuring at different conditions using synchrotron SAXS can be used to optimize the synthesis by analyzing the particles directly in the gas phase. Besides to the influence of the heating temperature and surfactant to TEOS ratio, also the gas flow (residence time) and drying behavior was analyzed.

The electron density maps from deposited particles were calculated and the silica matrix thickness was deduced from model fittings. The particle shape and size distribution was determined using SEM. The size analysis was done for particles deposited at different dryer temperatures. As we outline in this work comparing both, *in situ* (gas phase and deposited) and *ex situ* (deposited) data give new information on how to optimize process parameters to produce highly ordered mesostructures.

Materials and Methods

Sample Preparation. Aerosol particles were produced from a precursor solution containing tetraethylorthosilicate (TEOS) as the inorganic precursor, cetyltrimethyl-ammonium bromide (CTAB) as the surfactant, deionized water and 1 M HCl. All chemicals were supplied from

Sigma Aldrich, Austria. The precursor preparation procedure was the following: The molar ratio used was (CTAB:TEOS:H2O:HCl) 0.14:1:41:0.13 (pH ~2.5),[9,10] and for one set of experiment the CTAB/TEOS ratio was varied from 0.04 to 0.25. CTAB was mixed with water and stirred for about 15 min. Then TEOS and 1M HCl was added and further stirred for 15 min. Typically the solutions used for all experiments have been aged about 5 to 8 hrs.

Synchrotron SAXS and SEM. Synchrotron SAXS experiments were performed at the Austrian high-flux SAXS beamline of the 2 GeV electron storage ring ELETTRA (Trieste, Italy).[22,23] Data acquisition was done using a one dimensional linear position sensitive Gabriel detector[22] for *in situ* studies covering the q-range of interest from about 0.19 to 4.2 nm^{-1} and a two dimensional CCD camera for the powder diffraction samples covering the q-range from about 0.34 to 3.93 nm^{-1} at 8 keV photon energy. Silver behenate (CH_3-$(CH_2)_{20}$-COOAg, unit cell parameter 5.84 nm) was used for the calibration of the angular scale of measured intensity.[24]

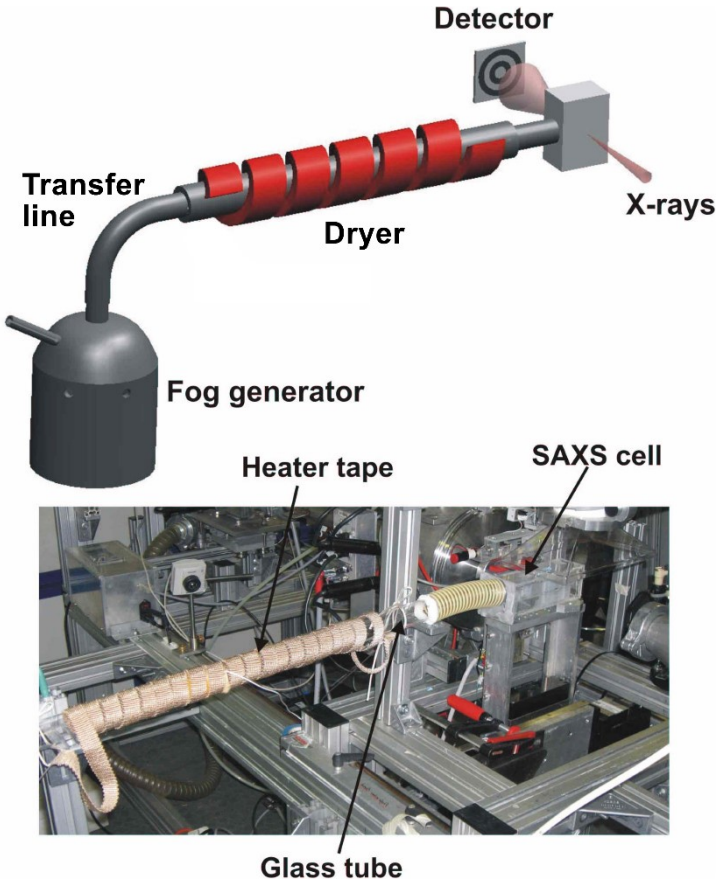

Fig. 1. *In situ set-up for the study of EISA of aerosol particles, schematic (top) and photo (bottom).*

The set-up for the *in situ* analysis of the mesostructuring in gas phase is shown in Fig. 1. Aerosol droplets were generated using the in house built aerosol generator (using a ceramic disc mist maker), that produce droplets in the size range of ~2.5 µm with an evaporation rate of 14 ml/h at the end of the transfer line of the aerosol generator. The produced droplets were carried by an air flow of desired rate (measured in Standard Litre per Minute, SLM) to the dryer with a length of 1 m, that can be heated up to 300 °C. The temperature has been measured at the end of the dryer directly in the gas phase, i.e. the aerosol temperature. For the SAXS analysis of the aerosol a sample cell with free X-ray path (windowless) was placed at the end of the dryer and an efficient exhaust system was used to remove the areosol after the SAXS cell. Further details on the aerosol particle set-up are given elsewhere.[21]

Further measurements have been conducted on deposited particles. *In situ* deposition has been performed by placing a thin X-ray foil directly in side the SAXS cell at the same position, at which the aerosol particles have been measured. *Ex situ* deposition was performed by putting an air filter paper at the inlet of the exhaust system. The powder was then collected from the filter paper, filled into 1 mm diameter glass capillaries (Hilgenberg, Malsfeld, Germany) and measured after rigorous drying.

SEM imaging was carried out to characterize the average particle sizes at different temperatures working with a Zeiss Supra 40 instrument (Carl Zeiss MicroImaging GmbH, Germany). The accelerating field for the primary electrons was set at 1.2 keV in order to minimize the accumulation of charge on the particles surface. In this way the actual nanoparticle surface could be scanned without any covering conductive layer.

Data Treatment

The electron density maps were derived from the small angle X-ray diffraction patterns by standard procedures (for details see e.g., ref.25). After the raw data have been corrected for background scattering, all recorded Bragg peaks where fitted by Lorentzian distributions. The fittings were carried out using the software package Igor Pro 6.03 (WaveMetrics, Lake Oswego, OR). Thereafter, a Lorentz correction was applied for all powder diffraction patterns by multiplying each peak intensity (peak area) by the square of the corresponding wave vector, q^2.Further, the intensities were corrected for their multiplicity (for a discussion on powder sample corrections see ref.26). The square root of the corrected peak intensities

I_{hk} of the (10), (11), (20), and (21) reflections were used for the calculation of the electron density maps (using IDL 5.2, ITT Visual Information Solutions, Boulder, CO). The electron density contrast for the 2D hexagonal phase is expressed by the Fourier series of cosines, as given in equation 1:

$$\tilde{\rho}_e(\mathrm{r}) = \sum_{hk}^{\max} \alpha_{hk} \sqrt{I_{hk}} \cos(\mathrm{q}_{hk} \cdot \mathrm{r}) \tag{1}$$

where α_{hk} are the phases, h, k are the Miller indices and q_{hk} is the scattering vector. The phase combination -1, +1, +1, and -1 was taken from ref.27

Alternatively the decomposition of the electron density maps into silica and CTAB compartments with cylindrical shape, respectively, was achieved by model calculations interpreting the diffraction data with a simple two-phase model taken from Impéror-Clerc et al.[28] and Zickler et al..[29] The structure model contains uniform densities for the corona and core, respectively. Fig. 2 shows the model having the density ρ_1 and radius R_1 for CTAB and ρ_0 for silica matrix. With this model the corrected integrated intensities I_{hk} of different diffraction peaks (*h.k*) were fitted applying:[28]

$$I_{hk}(q_{hk}) = K \cdot \left(2J_1(q_{hk}R_1)/(q_{hk}R_1)\right)^2 \tag{2}$$

where *K* is a scaling constant (including the electron density contrast) and J_1 is the Bessel function of the first kind of first order.

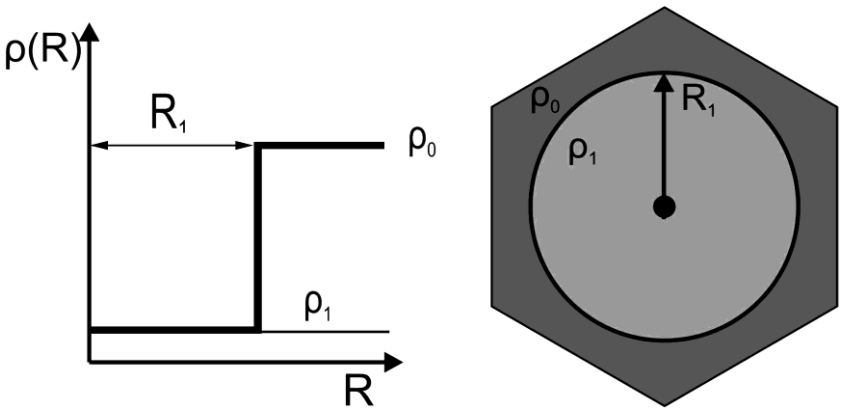

Fig. 2. *Two-density phase model, silica with high electron density ρ_0 and inner core with lower density ρ_1 and radius R_1 of CTAB.*

For the examination of the lattice spacing evolution as a function of dryer temperature, we applied a simple two step exponential function with the constraint for continuity at 100 °C.

Results

In this work we present data obtained in gas phase and from deposits. The gas-phase data were recorded directly from the aerosol at the end of the dryer. Fig. 3 shows the comparison between the two. The solution was prepared with a CTAB to TEOS ratio of 0.14. The aerosol generator was operated with a flow rate of 5 SLM keeping the residence time in the dryer as short as possible in order to follow the silica condensation close to full hydration. In the gas phase, the recorded signal is comparatively weak and only the first order reflection is visible, whereas from deposits we were able to record also the higher order reflections, i.e. the (11), (20) and (21) reflections of the hexagonal phase. The impact of the key process parameters was directly deduced from gas phase measurements, while detailed structural information was revealed from experimental data of the deposited samples.

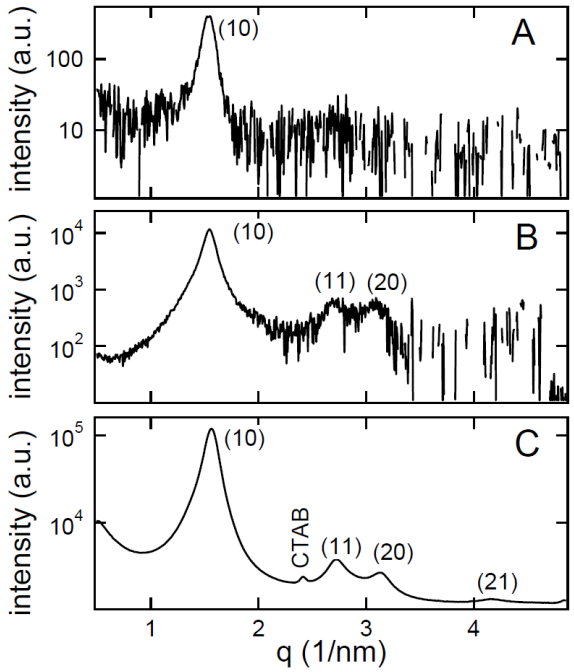

Fig. 3. *Comparison between diffraction data obtained in gas phase (A), from in situ (B) and ex situ deposits (C) (T =200 °C, flow = 5 SLM). The (10), (11), (20) and (21) reflections of the hexagonal phase of the silica aerosol are indicated together with the reflection from CTAB crystals in the ex situ deposited data. Solution prepared with a CTAB to TEOS ratio of 0.14.*

1.Influence of Temperature, Composition and Flow on the Unit Cell Parameter a in Gas Phase.

The final mesostructure formed depends on various experimental parameters like (i) dryer temperature, (ii) the surfactant to inorganic oligomer ratio, and (iii) the air flow. Therefore, experiments were performed by varying these parameters to investigate their impact on the fully condensed final silica mesostructure.

For the investigation of aerosol particles in the gas phase, the scattering data were recorded. The temperature inside the dryer is a crucial parameter, which is responsible for the rate of evaporation and the simultaneous rate of silica condensation that determines the final structure of the particles. Further, the surfactant to TEOS ratio is an important factor that influences the final mesostructure. Well-ordered hexagonal honeycomb patterns of silica can be obtained in the CTAB-Si ratio range of 0.09 to 0.28.[9] Solutions were prepared with different CTAB to TEOS ratios and gas phase data were recorded at different dryer temperatures at a flow rate of 5 SLM. The content of CTAB was varied keeping the TEOS content constant obtaining solutions with CTAB to TEOS ratios of 0.06, 0.14 and 0.25.

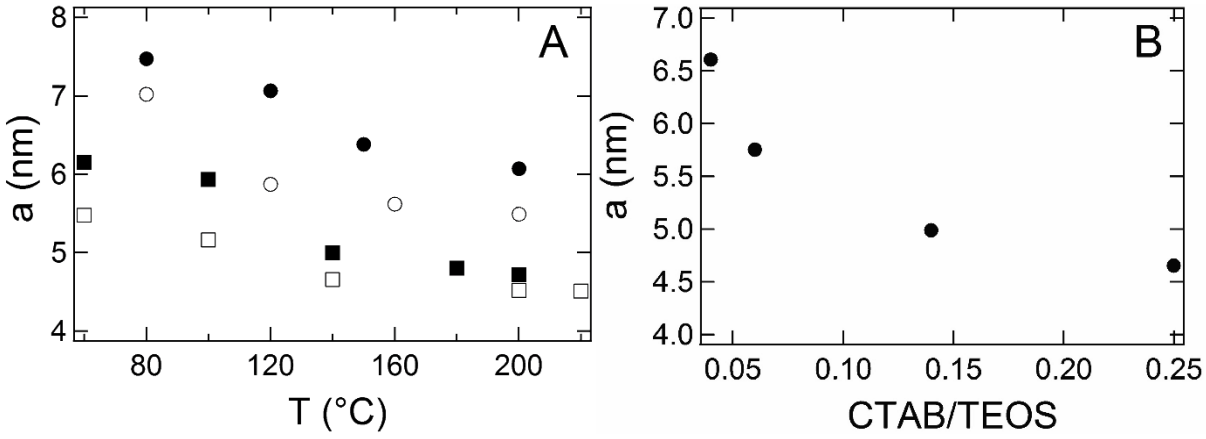

Fig. 4. *Unit cell parameter, a, as a function of temperature and CTAB/TEOS ratio. (A) The temperature dependence of a is given for different CTAB to TEOS ratios: 0.04 (●), 0.06 (○), 0.14 (■) and 0.25 (□). (B) For T = 150 °C the tendency of a is given as a function of the CTAB/TEOS ratio. The air flow used was 5 SLM and the pH of the solution was ~2.5.*

We note, that keeping the CTAB content constant and varying the TEOS concentration leads to the same results. As shown in previous studies, irrespective of CTAB or TEOS content variation, only their ratio is of importance.[9] Fig. 4A shows the dryer temperature dependence of the unit cell parameter a at different surfactant to TEOS ratios. It is seen that

the regime below 100 °C is displaying larger unit cell parameters due to the hydration of the polar interface of the aggregated micellar rods, whereas above 100 °C the water evaporates rapidly. A pronounced decrease in cell parameter a can be seen between 100 to 150 °C, thereafter the slope Δa/ΔT drops below 0.003 nm/°C. We also observed a decrease in the lattice parameter with increase of the CTAB to TEOS ratio. Fig. 4B shows a decrease of a from 6.6 nm to 4.7 nm when the CTAB to TEOS ratio is changed from 0.04 to 0.25. This unit cell parameter shrinkage with increasing relative surfactant concentration is mainly due to a reduction in the silica wall thickness. Further structural details are discussed in the section about electron density calculation and model fitting.

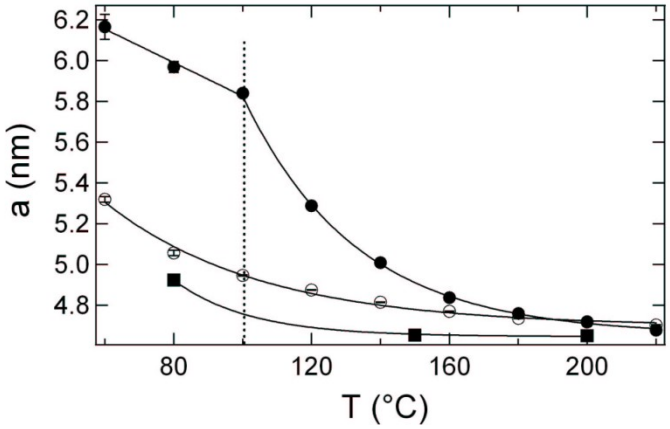

Fig. 5. *Dependence of cell parameter a, on dryer temperature obtained with different experimental conditions. Gas phase (●), in situ deposited (○), and ex situ deposited data (■) are compared at a flow rate of 5 SLM. The gas phase data were fitted with a two-step exponential function, and deposited data are fitted with a single-exponential function.*

This observed dependence of dryer temperature and surfactant to Si ratio on the final formed mesostructure can be further supported by the comparison of the gas phase data with data from deposited powders. Fig. 5 shows the difference between *in situ* gas phase, *in situ* particle deposits (investigated immediately after deposition), and ex situ particle deposited data (recorded after extensive drying). It is clearly seen that the unit cell parameter *a* is highest for the gas phase data, which is mainly due to the hydration of the particles inside the gas phase. Two hydration regimes can be distinguished, i.e. below and

above 100 °C. These data are best fitted by a two-step exponential model that distinctly demonstrates the significant hydration below 100 °C and residual hydration above 100 °C. Further it can be seen that the condensation of the structure is only completed after rigorous drying (note, the slightly lower cell parameters for the ex situ deposited particles as confronted with the *in situ* deposited particles data).

Finally, the influence of the residence time of the aerosol particles in the dryer was investigated by changing the rate of the air flow, which carries the fog from the generator to the dryer and then to the SAXS cell. The flow rate was varied from 2 to 7 SLM. The unit cell parameter *a* dependence on air flow is shown in Fig. 6 at different dryer temperatures. Given air flows from 2 to 7 SLM, the average residence time of the particles inside the dryer (1 m long) is about 30 to 9 s. The results demonstrate that at high temperatures, 150°C and 200°C, the influence of the air flow on the lattice parameter *a* of the formed particles is minor, but at 100°C the drying is not elevated, so that the silica/surfactant system is influenced by the air flow. At short residence times (i.e. residence times from 15 to 4.7 s (i.e., 4 and 7 SLM) the increased fraction of dry air added into the system causes a shrinkage of the lattice parameter of the mesophase due to reduced saturated partial water pressure. At long residence times (above 15s) the drying takes place already in the gas phase as can be seen in the reduced lattice spacing *a*.

We also note that at higher flow rates than 7 SLM a dilution of the particles in the fog takes place reaching the detection limit of 10^7 particles/s.

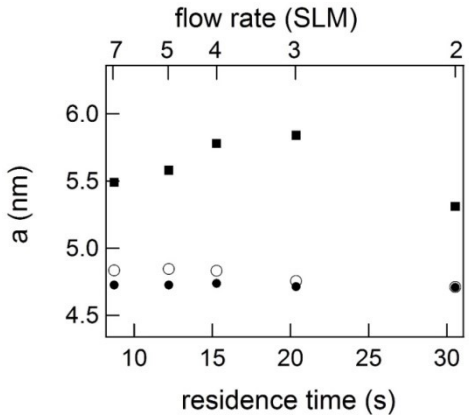

Fig. 6. *Residence time dependence (flow rate from 7 to 2 SLM) on the unit cell parameter a at different dryer temperatures. The dryer temperatures were 100 °C (■), 150 °C (○) and 200 °C (●); (CTAB to TEOS ratio 0.14)*

2. SEM Imaging of Silica Particles.

Fig. 7 shows the SEM image of silica particles deposited on a silicon wafer at a dryer temperature of 150 °C for 20 s (left) and the size histograms obtained at 80, 150 and 200 °C. Spherical particles with sizes ranging from few hundreds of nm to few µm are observed on a silica surface. The average particle size does not change much with the dryer temperature, because the final particle size depends mainly on the droplet size produced by the aerosol generator.

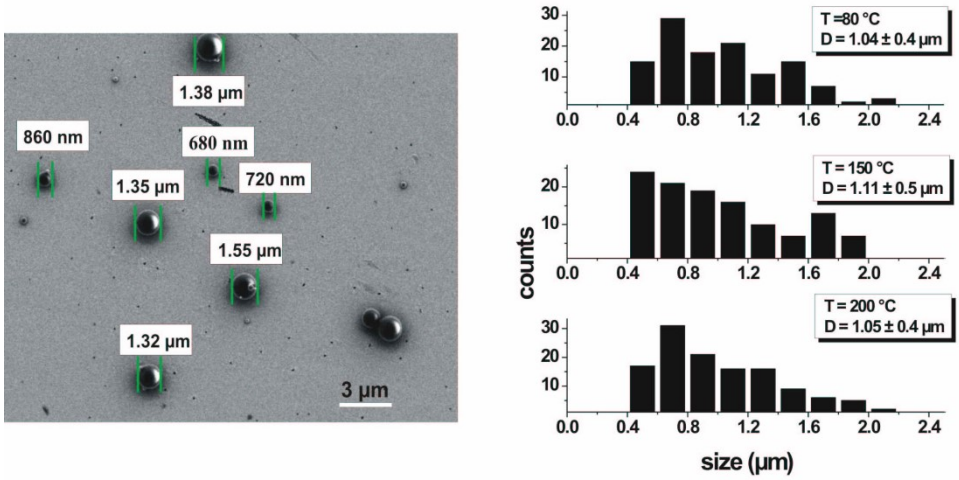

Fig. 7. *SEM image of silica aerosol particles deposited on a silicon wafer for 20 s at a dryer temperature of 150°C (left) and the size histograms of Si particles on silica surface at 80, 150, and 200°C (right).*

3. Electron Density Calculations and Model Fitting.

For a more detailed structural analysis the aerosol particles were deposited on a clean surface and the diffraction data were obtained from the collected powder, which was sealed in a capillary. Fig. 8 shows the calculated two dimensional electron density maps for samples prepared at dryer temperatures of 80, 150 and 200°C at a flow of 5 SLM and a CTAB to TEOS ratio of 0.14.

The electron density maps show a hexagonal honeycomb structure with no significant differences except for the slight decrease in the unit cell parameter with the increase in temperature.

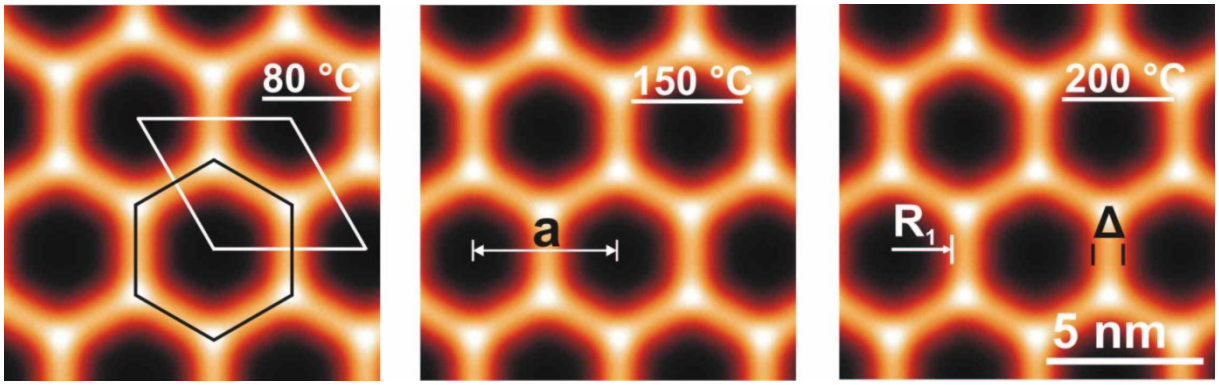

***Fig. 8**. Electron density maps calculated from the integrated peak intensities of the (10), (11), (20) and (21) reflections. The bright region indicates the silica matrix and the darker region the CTAB micellar regions. The unit cell (white line) together with Wigner-Seitz cell (dark line), lattice parameter, a, CTAB core radius, R1, and silica wall thickness, Δ, are shown. The solutions were prepared at a CTAB to TEOS ratio of 0.14.*

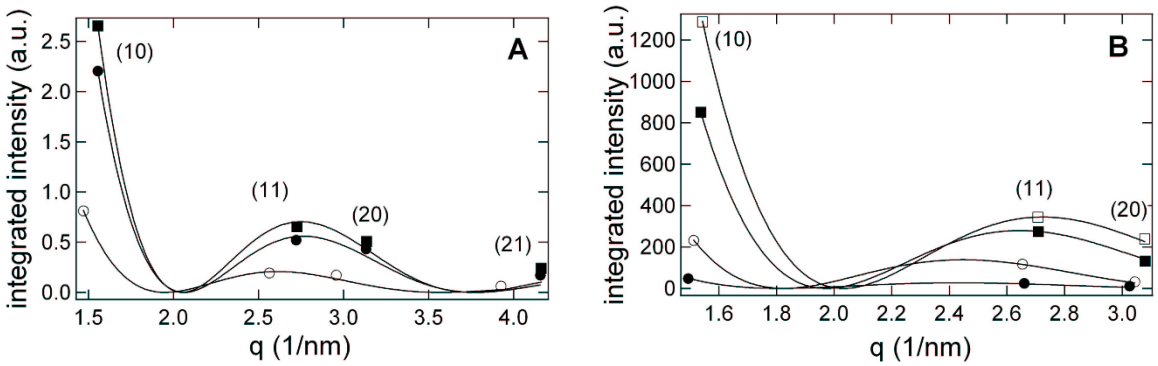

***Fig. 9**. Model fits for the integrated intensities at different dryer temperatures. The model fitting was carried out using equation 2. (A) Ex situ deposited at 80°C (○), 150°C (●) (intensity multiplied 2 times), and 200°C (■) (intensity multiplied 3 times) are displayed. (B) In situ deposited at 120°C (●), 140°C (○) (intensity multiplied 2 times), 180°C (■) (intensity multiplied 3 times) and 200°C (□) (intensity multiplied 4 times) are shown. The CTAB to TEOS ratio was 0.14.*

Fig. 9 shows the model fit of the integrated intensities for samples prepared at different dryer temperatures, for *ex situ* deposited (A) and *in situ* deposited (B) samples. The CTAB to TEOS ratio was 0.14 and the pH of the solution was ~ 2.5. Table 1 summarizes the fit results including the unit cell parameter, a, the core radius, R_1, the deduced silica wall thickness,

$\Delta = a - 2R_1$, and the silica cross-sectional area, $A_\Delta = (3)^{1/2} / 2a - \pi R_1^2$, at different dryer temperatures. The first set gives the results for the gas phase, the second set for the *in situ* deposited and the third set for the *ex situ* deposited data. It is clearly seen that the decrease in the lattice parameter is mainly due to the monotonous shrinkage of the CTAB core with increasing temperature. Further, as judged from the fraction of the silica cross-sectional area, the amount of condensed silica does not change with temperature.

Similar model fittings were carried out using equation 2 for particles deposited at different CTAB to TEOS ratio (0.04, 0.14 and 0.25) to analyze in detail the trend seen in the gas phase data (Fig. 4). Table 2 shows the fit results at different CTAB to TEOS ratios. The dryer temperature was 80°C and the pH of the solution was ~ 2.5. The first set shows the results of gas phase and the second set the results of the *ex situ* deposited data. In contrast to the temperature dependent trend, the unit cell parameter decrease with increasing CTAB to TEOS ratio is mainly caused by a thinning of the silica wall. The shrinkage of the CTAB radius is relatively small.

Fig. 10 shows the normalized Full Width at Half Maximum (FWHM) of the (20) peak with respect to the dryer temperature as well as to the CTAB to TEOS ratio. As known from the Debye-Scherrer relation the peak width is directly correlated to the long-range order of crystalline material. Detailed peak shape analysis requires the deconvolution of measured peak widths with the intrinsic instrumental resolution function. However, already qualitative comparisons are sufficient to judge the improvement of the mesostructure. Since the FWHM broadens with an increase in dryer temperature, this indicates a decrease in the long range order. Further, it can be seen that at the CTAB to TEOS ratio of 0.14 seems to result in the best ordered inner mesostructure.

Table 1. *Structural Parameters at Different Furnace Temperatures.*

	T (°C)	a (nm)	R_1 (nm)	Δ (nm)	A (nm^2)	A_Δ (nm^2)	A_Δ/A
I	60	6.17±0.04	-	-	-	-	-
	80	5.97±0.03	-	-	-	-	-
	100	5.84±0.01	-	-	-	-	-
	120	5.29±0.01	-	-	-	-	-
	140	5.01±0.01	-	-	-	-	-
II	80	5.06±0.01	-	-	-	-	-
	100	4.95±0.01	-	-	-	-	-
	120	4.86±0.01	2.11±0.09	0.64±0.11	20.44	6.44	0.32
	140	4.76±0.01	2.09±0.08	0.60±0.09	19.92	6.10	0.31
	180	4.72±0.01	1.94±0.08	0.84±0.09	19.29	7.45	0.38
III	80	4.93±0.01	1.96±0.04	1.01±0.08	21.04	8.98	0.42
	150	4.66±0.01	1.86±0.04	0.95±0.07	18.81	7.94	0.42
	200	4.66±0.01	1.87±0.03	0.93±0.07	18.81	7.83	0.42

Core radius R_1, cell parameter a, silica matrix thickness Δ, cross-sectional area of a unit cell A and silica cross-sectional area A_Δ at different dryer temperatures T. The flow rate = 5 SLM, CTAB/TEOS ratio = 0.14 and pH ≈ 2.5.

I - gas phase data, II - in situ deposited data and III - ex situ deposited data.

***Table 2**. Structural Parameters at Different CTAB to TEOS Ratios.*

	Ratio	*a* (nm)	R_1 (nm)	Δ (nm)	A (nm^2)	A_Δ (nm^2)	A_Δ/A
I	0.04	6.61±0.01	–	–	–	–	–
	0.06	5.75±0.01	–	–	–	–	–
	0.14	4.99±0.01	–	–	–	–	–
	0.25	4.65±0.01	–	–	–	–	–
II	0.06	5.66±0.01	2.195±0.05	1.27±0.1 (1.35)	27.74	12.61	0.45
	0.14	4.93±0.01	1.964±0.04	1.05±0.08 (0.87)	21.04	8.93	0.42
	0.25	4.39±0.02	1.905±0.02	0.57±0.04 (0.58)	16.69	5.23	0.31

Core radius R_1, cell parameter a, the silica wall thickness Δ, cross-sectional area of a unit cell A and silica cross-sectional area A_Δ. The silica wall thickness from Bore et al.[9] is given in brackets. The flow rate = 5 SLM, dryer temperature = 80 °C and pH ≈ 2.5.

I - gas phase data and II - ex situ deposited data.

Discussion

The effect of the reactor temperature and the surfactant-to-silica ratio on the final formed mesostructured silica particles are discussed comparing the gas phase and powder deposited sample data.

1.Effect of Reactor Temperature.

Reactor temperature is an important process parameter which influences both evaporation and silica condensation reaction rates. Importantly, the first steps of evaporation, micelle aggregation followed by the silica shell formation are too fast processes to be recorded by *in situ* gas phase measurements at the end of the dryer.[10] However, especially at low production temperatures the condensation process is not fully completed and it is possible

to track the influence of residual hydration. As shown in Fig. 4 A and Fig. 5, the presence of water and its evaporation is a critical factor in the formation of mesostructured particles by the EISA process. As can be seen in Table 1 comparing the *in situ* and the *ex situ* deposited sample results, both, the *in situ* CTAB radius and silica wall thickness are not final. First, the CTAB radius is slightly bigger. At about 150°C the difference in R_1 is, e.g. about 0.23 nm. This is in the range of one water layer and thus we assume that the CTAB micelles are still covered by a limiting hydration shell. Similar observations were made in a study of micelle hydration in CTAB templated silica thin films.[30] Second, the effect of lower production temperatures on the silica corona thickness is less pronounced. However, taking a closer look to the cross-sectional areas reveals that the condensation process is not completed. From 120 to 200°C A_A/A increases continuously from 32 % to the final value of 42 %. Note, that for all three *ex situ* deposited samples the relative cross sectional area of silica is the same (42 %).

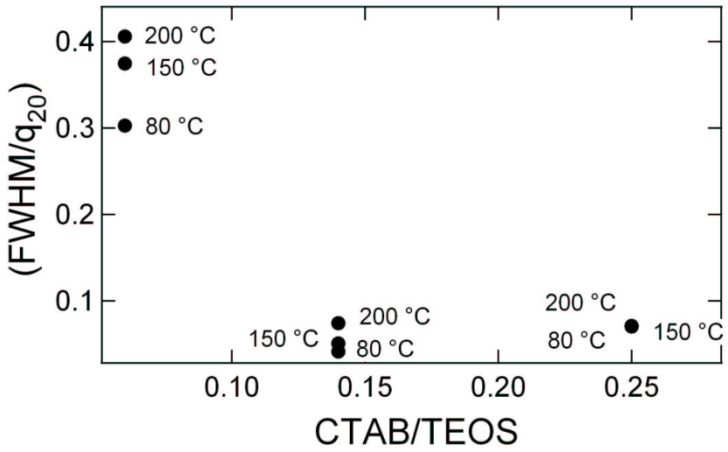

Fig. 10. *Behavior of FWHM/q20 of the (20) peak as a function of temperature and CTAB to TEOS ratio.*

The effect of the dryer temperature on the size of the CTAB core and on the silica wall thickness can be easily understood. Temperature increase induces more and more disorder in the CTAB chains (trans-gauche isomerizations) and hence causes an effective chain shortening. Another argument responsible for the shrinkage of the CTAB core could be the isotropic contraction of the silica matrix during progressive polycondensation. This trend is observed in both the *in situ* and ex situ deposited samples. However, the progression in the

in situ deposited data is overlapped by the water evaporation (see the R_1 values in Table 1). This also explains the steeper decay of the lattice parameter seen in Fig. 5. The temperature effect on the silica wall thickness in fully dried samples (*ex situ* data) is only minor (see Table 1, Δ values); however, as mentioned above, the relative cross sectional area of the silica corona remains constant.

2. Effect of CTAB/TEOS Ratio.

The silica wall thickness decreases from 0.5 to 1.2 nm for 0.06 ≤ CTAB/TEOS ≤ 0.25, which is comparable to the results obtained in previous studies using techniques other than SAXS (see ref. 9 and references therein; rf. Table 2). This thinning with increasing CTAB to TEOS ratio can be explained by an increasing surface fraction of the liquid crystalline moiety which must be encapsulated by a constant amount of silica. There are two limiting regimes, one in which there is not enough surfactant material to create a stable template media, and on the other extreme, when there is not enough inorganic material to build up stable walls. According to the literature stable hexagonally ordered mesoporous particles can be obtained in the CTAB to TEOS range of 0.09 to 0.22.[9] Note that at low dryer temperatures it is possible to extend this interval (i.e. we obtained well ordered structures in the range of 0.06 to 0.25).

The general process of silica condensation is well understood [31,32] and shall be explained here only briefly. Throughout this study acidic conditions were used (i.e. our solutions having initially a pH of about 2.5, which is close to the isoelectric point of the silicate species.[33,34]) This means that the initially anionic silica species becomes positively charged and, as the evaporation proceeds, the silica mesostructure is formed by the known $S^+X^-I^+$ templating route[31] (where S^+ defines the CTAB head group, X^- the acid anion, and I^+ stands for the protonated silicate species).

The changes in the core region are small, but significant. As listed in Table 2 the core radius R_1 decreases slightly by 0.3 nm for 0.06 ≤ CTAB/TEOS ≤ 0.25, showing that the surfactant packing in the micellar structure is influenced by the CTAB to Si ratio. At this point it is useful to introduce the simple molecular shape concept of Israelachvili,[35] which describes the effective molecular geometry of the involved surfactants and its influence on the formation of diverse self-assembled nanostructures. It is expressed as the critical packing parameter (CPP), which is defined as $V / (A_I l)$, where V is the hydrophobic chain volume, A_I is the head-

group area at the interface, and *l* is the hydrophobic chain length. In the given case, the temperature is constant and hence, *l* should not play any role. Nevertheless, increasing the CTAB concentration reduces the electrolyte concentration (Cl^- reduces effectively) and thus the charge shielding between the CTAB head-groups diminishes.[36] In other words, the area per surfactant molecule AI increases due to increased electrostatic repulsions, which is equivalent to an increase in interfacial curvature (smaller CPP). This in turn means of course that the pore diameter decreases with increasing CTAB content.

3. Quality Control.

While comparing gas-phase with deposited powder data helps to understand especially the influence of residual hydration and final condensation of the mesoporous superstructure, the quality of the end-product can only be judged from *ex situ* deposited data. As long as only relative quality parameters are concerned, it is sufficient to compare the FWHM of the diffraction peaks of the respective powders (Fig. 10). From the above discussion it is clear that there exists an optimal CTAB to TEOS ratio for the formation of well ordered mesostructures. We find an optimum value of 0.14, which agrees well with findings of other groups.[9] Interestingly, the optimum dryer temperature lies around 80°C only. One explanation for this could be that at low temperatures the drying as well as the final silica condensation processes are slowed down. In this respect, it is also important to recall that there is evidence that the silica network remains flexible for several hours, if well hydrated and at low temperatures,[31] i.e. the hexagonal superstructure has more time to find a stable low energy configuration.

Conclusions

Production of highly ordered mesostructured particles using EISA from aqueous solution of CTAB and TEOS is a very versatile technique. In this work we report the influence of different parameters on the final formed silica mesostructure by comparing gas phase data and data obtained from deposited powders. Silica mesostructure particles were produced with an in-house built aerosol generator, which is capable of producing a sufficient particle concentration for direct gas phase investigations.[20] Concerning the synchrotron SAXS data analysis, detailed structural results were directly achieved by the application of Fourier

transform analysis as well as by the application of a simple two electron density model and further discussed on the basis of molecular shapes and interface curvature changes. Most extensively the impact of the reactor temperature as well as the surfactant to silica ratio was examined. While the temperature mainly affects the CTAB core radius, the CTAB to TEOS ratio mainly changes the silica wall thickness. Comparison of gas phase and powder deposited data are especially useful for the understanding of the influence of residual hydration and slower silica condensation steps. Finally, the FWHM of the recorded diffraction peaks was exploited to interpret the long range order of the final formed structure. Heating temperatures about 80°C and medium surfactant to silica ratio (about 0.14) lead to nanostructures of best quality. Moreover, under slow drying conditions the CTAB to TEOS ratio range for the production of well ordered mesostructures enlarges.

Acknowledgments

We wish to acknowledge C. Morello for the technical support during the construction of the experimental setup, and B. Marmiroli for fruitful discussions

References

(1) Taguchi, A.; Schüth, F. *Microporous and Mesoporous Materials* 2005, *77*(1), 1-45.

(2) Sanchez, C.; Boissiere, C.; Grosso, D.; Laberty, C.; Nicole, L. *Chemistry of Materials* 2008, *20*(3), 682-737.

(3) Sanchez, C.; Rozes, L.; Ribot, F.; Laberty-Robert, C.; Grosso, D.; Sassoye, C.; Boissiere, C.; Nicole, L. *Comptes Rendus Chimie* 2010, *13*(1-2), 3-39.

(4) Boissiere, C.; Grosso, D.; Chaumonnot, A.; Nicole, L.; Sanchez, C. *Advanced Materials* 2010, *DOI: 10.1002/adma.201001410*.

(5) Brinker, C.; Lu, Y.; Sellinger, A.; Fan, H. *Adv. Mater.* 1999, *11*, 579-585.

(6) Lu, Y.; Fan, H.; Stump, A.; Ward, T.; Rieker, T.; Brinker, C. *Nature* 1999, *398*, 223–226.

(7) Grosso, D.; Cagnol, F.; Soler-Illia, G. J. D. A.; Crepaldi, E. L.; Amenitsch, H.; Brunet-Bruneau, A.; Bourgeois, A.; Sanchez, C. *Advanced Functional Materials* 2004, *14*(4), 309-322.

(8) Melosh, N. A.; Davidson, P.; Chmelka, B. F. *Journal of the American Chemical Society* 2000, *122*(5), 823-829.

(9) Bore, M.; Rathod, S.; Ward, T.; Datye, A. *Langmuir* 2003, *19*, 256–264.

(10) Boissiere, C.; Grosso, D.; Amenitsch, H.; Gibaud, A.; Coupe, A.; Baccile, N.; Sanchez, C. *Chem. Communications* 2003, *22*, 2798–2799.

(11) Agren, P.; Rosenholm, J. B.; Schwarzenbacher, R.; Kriechbaum, M.; Amenitsch, H.; Laggner, P.; Blanchard, J.; Schüth, F. *Journal of Physical Chemistry B* 1999, *103*(29), 5943-5948.

(12) Jungnikl, K.; Rappolt, M.; Shyjumon, I.; Sartori, B.; Laggner, P.; Amenitsch, H. *Aerosol Science and Technology* 2010, (accepted)

(13) Areva, S.; Boissiere, C.; Grosso, D.; Asakawa, T.; Sanchez, C.; Linden, M. *Chem. Communications* 2004, *10*, 1630–1631.

(14) Eric Hampsey, J.; Arsenault, S.; Hu, Q.; Lu, Y. *Chemistry of Materials* 2005, *17*(9), 2475-2480.

(15) Jiang, X.; Brinker, C. J. *Journal of the American Chemical Society* 2006, *128*(14), 4512-4513.

(16) Sen, D.; Spalla, O.; Taché, P.; Haltebourg, A.; Thill, A. *Langmuir* 2007, *23*, 4296–4302.

(17) Beaucage, G.; Kammler, H.; Mueller, R.; Strobel, R.; Agashe, N.; Pratsinis, S.; Narayanan, T. *Nature Mater.* 2004, *3*, 370–374.

(18) Stasio, d.; Mitchell, J.; LeGarrec, J.; Biennier, L.; Wulff, M. Carbon 2006, 44, 1267.

(19) Ossler, F.; Larsson, J. *J. Appl. Phys.* 2005, *98*, 1–11.

(20) Shyjumon, I.; Rappolt, M.; Sartori, B.; Amenitsch, H.; Laggner, P. *Rev. Sci. Instrum.* 2008, *79*, 043905.

(21) Wyslouzil, B. E.; Cheung, J. L.; Wilemski, G. ; Strey R. Phys. Rev. Lett. 1997, 79, 432-434.

(22) Amenitsch, H.; Rappolt, M.; Kriechbaum, M.; Mio, H.; Laggner, P.; Bernstorff, S. *J. Synchrotron Rad.* 1998, *5*, 506–508.

(23) Bernstorff, S.; Amenitsch, H.; Laggner, P. *J. Synchrotron Rad.* 1998, *5*, 1215–1221.

(24) Huang, T.; Toraya, H.; Blanton, T.; Wu, Y. *J. Appl. Cryst.* 1993, *26*, 180–184.

(25) Rappolt, M. In *Advances in Planar Lipid Bilayers and Liposomes*; Leitmannova-Liu, Ed.; Elsevier Inc., Amsterdam, 2006; Vol. 5, p 253.

(26) Warren, B. *X-ray diffraction*; Dover Publications, New York, 1990.

(27) Beurroies, I.; Agren, P.; Buchel, G.; Rosenholm, J.; Amenitsch, H.; Denoyel, R.; Linden, M. *J. Phys. Chem. B* 2006, *110*, 16254–16260.

(28) Impéror-Clerc, M.; Davidson, P.; Davidson, A. *J. Am. Chem. Soc.* 2000, *122*, 11925–11933.

(29) Zickler, G.; Jähnert, S.; Wagermaier, W.; Funari, S.; Findenegg, G.; Paris, O. *Phys. Rev. B* 2006, 73, 184109.

(30) Dourdain, S.; Rezaire, A.; Mehdi, A.; Ocko, A., B.M. Gibaud *Physica B* 2005, *357*, 180–184.

(31) Tanev, P.; Pinnavaia, T. *Chem. Mater.* 1996, *8*, 2068-2079.

(32) Che, S.; Li, H.; Lim, S.; Sakamoto, Y.; Terasak, O.; Tatsumi, T. *Chem. Mater.* 2005, *17*, 4103–4113.

(33) Huo, Q.; Margolese, G., and D.I. Stucky *Chem. Mater.* 1996, *8*, 1147-1160.

(34) Brinker, C.; Scherer, G. *Sol -Gel Science*; Academic Press, Boston, 1990.

(35) Israelachvili, J.; Mitchell, D.; Ninham, B. *J. Chem. Soc. Faraday Trans.* 1976, *72*, 1525-1568.

(36) Liu, M.; Shen, H. S.; Cheng, S. *J. Am. Chem. Soc.* 2009, *131*, 3998–4005.

C. Aerosol Flow Reactor with Controlled Temperature Gradient for In situ Gas-Phase X-ray Experiments -Measurements of Evaporation Induced Self-Assembly (EISA) in Aerosols

K. Jungnikl[a*]; M. Rappolt[a]; I. Shyjumon[a+]; B. Sartori[a]; P. Laggner[a]; H. Amenitsch[a]

[a]Institute of Biophysics and Nanosystems Research, Austrian Academy of Sciences, Graz, Austria

+ *present address*: Institute for Synchrotron Radiation, Karlsruher Institut für Technologie (KIT), Eggenstein-Leopoldshafen, Germany

Abstract

We present a new *in situ* aerosol flow reactor for gas-phase studies during drying of aerosol droplets by small-angle X-ray scattering (SAXS). The setup consists of an outer confinement shell and an inner tube for aerosol flow that can be positioned by a remote-controlled motor to perform scanning measurements along the flow path, providing 'quasi time resolved' information on the drying process. A controlled temperature step is provided by an insulating separation between a cooled and a heated section in the dryer. First experiments were performed on aerosols of surfactant- and silica-precursor/surfactant solutions (CTAB/ethanol, TEOS/CTAB). Measurements of the mesostructure formation during the initial steps of evaporation induced self assembly (EISA) were made, to illustrate the working principle of aerosol drying during passage through an adjustable temperature gradient.

Keywords: instrumentation development, small-angle X-ray scattering (SAXS), evaporation induced self assembly (EISA)

Introduction

Structural characterization of aerosols on the nanometer scale is important in a variety of scientific areas: for developing technical applications, like functional powders or catalytic materials (Kim et al. 2009; Moon et al. 2009; Sanchez et al. 2010), medical applications (drug delivery systems, diagnostic particles, nanotoxicology) (Tsapis et al. 2002; Ravichandran

2009), or for an assessment of the impact of artificial and naturally occurring aerosol particles on environment and climate (Wise et al. 2005). Small- (and wide-) angle X-ray scattering provides a fast and versatile method for characterizing nanoscale structural features (Schaefer et al. 1991), and even their relation to chemical reactivity and physical properties, if a relevant *in situ* experiment can be designed (Kammler et al. 2005; Marmiroli et al. 2010). Using the high brilliance available at synchrotron sources, it is possible to measure aerosols directly in the gas-phase (Boissiere et al. 2003; Sen et al. 2007; Shyjumon et al. 2008; Mitchell et al. 2010), avoiding the introduction of structural alterations by sampling, depositing, fixation, or time passing during the measurement. Time-resolved data acquisition is particularly crucial when fast synthesis processes are to be examined, like e.g. in our study, structure formation in aerosols of mesostructured microparticles.

Mesostructured microparticles have applications for catalysis, coatings, optics and drug delivery, and a large variety of morphologies and properties has been reported by applying different synthetic routes and recipes. EISA by spray drying provides an attractive route for the production of such powders, because it can be run cost-efficiently, fast and continuously, and provides good control of the product by selecting appropriate process parameters. The EISA process is driven by a progressive concentration of the non-volatile compounds of a precursor solution during evaporation of a solvent that is usually a mixture of one or more alcohols and water (Brinker et al. 1999). *In situ* studies of thin film structuring during the EISA process have been very useful for identifying critical parameters such as the relative humidity of the ambient atmosphere (Gibaud et al. 2003; Cagnol et al. 2003; Grosso et al. 2004; Dourdain et al. 2005). Studies available on the mesostructuring during spray drying are, however, mainly restricted to assessing the influence of process parameters on the final product (Boissiere et al. 2010; Alonso et al. 2007; Hampsey et al. 2005; Areva et al. 2004; Bore et al. 2003; Rao et al. 2002; Lu et al. 1999; Bruinsma et al. 1997), which is a drawback for understanding the mechanisms of the actual self-assembly process. The drying kinetics has previously been identified as influencing the overall particle morphology (Sen et al. 2007; Tsapis et al. 2002; Jayanthi et al 1993). In the case of mesostructuring droplets, the time- and temperature dependent shift of alcohol and water content along the radial evaporation gradient of the droplet additionally has consequences for mesophase self-assembly (Alonso et al. 2007; Gibaud et al. 2003) and Si-condensation (Boissiere et al. 2003).

The motivation for constructing the *in situ* aerosol dryer was to characterize the initial stages of the EISA process, by measuring the structural changes during passage of the aerosol through a temperature gradient.

Setup and Experimental Details

Aerosol flow reactor: Fig. 1a shows a schematic drawing of the working principle, Fig. 1b shows a sketch of the aerosol flow reactor. The dryer setup consists of two tubes, an outer confinement shell with fixed position and a vertical slit, and an inner tube with axial slits mounted on a stable aluminum support that can be moved inside the shell by an externally mounted motor stage. The vertical slit allows also wide-angle X-ray measurements up to 2θ ~ 30°. The slits are not covered with X-ray transparent foils to avoid background scattering from windows contaminated with eventually depositing aerosol. It is important to avoid these deposits, because they undergo continuing mesostructuration upon drying during the measurements, therefore the background signal changes and cannot be used for data correction. This 'open construction' demands a reliable exhaust at both, the vertical measurement slit and the outlet of the tube to avoid potential contamination of the hutch air with aerosol particles.

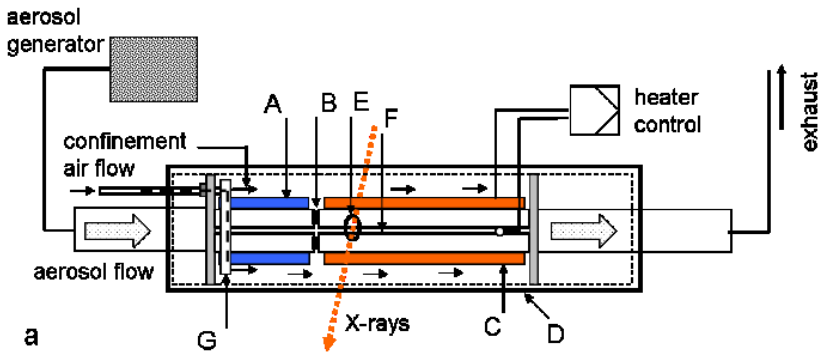

Fig. 1 (a) *Schematic drawing of the working principle of the flow reactor. A) cooled part of the dryer, B) insulating separation, C) heated part. The position of confinement shell D) and window (E) is fixed, the inner dryer tube with axial slit (F) is moved inside by a motor stage to change the measurement position within the aerosol flow path. A PT100 is mounted at the end of slit (F) to control the heating according to the max. aerosol temperature. (G) Ring-shaped outlet for confinement-air into the shell.*

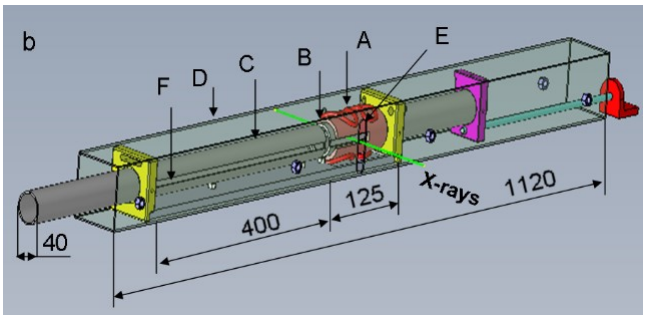

Fig. 1 (b) *Sketch of the aerosol dryer. A) cooled part of the dryer, B) insulating separation, C) heated part, D) confinement shell with X-ray window (E). F) axial slit in the inner tube. Distances are given in mm.*

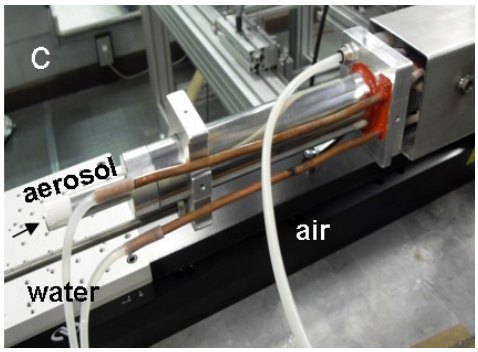

Fig. 1 (c) *Inlet piece with tubes for aerosol, cooling water and confinement-air.*

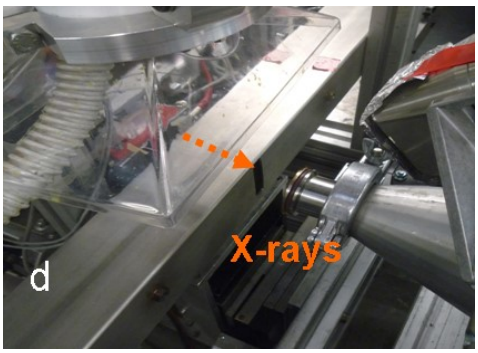

Fig. 1 (d) *Aerosol dryer mounted at the SAXS beamline at ELETTRA.*

The inlet piece (Fig. 1c) has an opening for aerosol flow into the inner tube, with a slideable tube-inset to allow an optional additional path of max. ~ 200 mm inside the flow reactor before the first measurement position (i.e., at the beginning of the axial slits). Additional openings in the inlet piece allow flow of air into the outer confinement shell and circulation of cooling water. Fig. 1d shows the aerosol dryer mounted at the experimental station at ELETTRA. The inner tube consists of a thermostat controlled water-cooled (Huber Unistat CC, Offenburg, Germany) part and a heated part that are separated by a thermal insulator to

provide a steep and adjustable temperature gradient. Heater tapes (Omegalux, Stamford, USA, 1040 W) were used as heating devices for the presented drying experiments; the effective power density at the inner tube was approximately 2.5 W/cm². To improve the efficiency and thermal stability, a thermal insulation blanked (ITM Fibermax, Schupp, Aachen, Germany) was attached to the outside of the heater tube. For achieving even higher temperatures, e.g. to observe calcination of aerosols, the heater tapes can be replaced by heating cartridges. A PT100 was placed at the end of the axial slit (i.e., at the end of measurement range), in the centre of the tube, approximately at the same height (with respect to tube diameter) as the beam position during X-ray measurements (see Fig. 1a). This configuration was chosen in order to control the heater with respect to the actual aerosol temperature at the final measurement position. Fig. 2 shows examples of temperature profiles measured with and without flow of reference aerosols. The temperature profile at the separation is influenced by the respective solvent, but also by temperature and relative humidity of the gas or air used as confinement. For the presented experiments, the starting temperature at the cooled part was kept at approximately room temperature (20 - 27°C); the maximum applied (air or aerosol) temperature in the scanning range was ~ 160°C. The maximum achieved temperature was 300°C (without aerosol). The measurements were taken at steps of 20 - 40 mm along the dryer tube that corresponded to time steps during aerosol flow of about 200 - 240 ms. The setup provides a residence time of the aerosol particles of ~ 1500 - 2000 ms in the scanning range, with a possible temporal resolution of ~ 50 ms, depending on the X-ray beam dimensions. These numbers are, however, a lower estimate, because the aerosol flow rate depends not only on the settings of the aerosol generator (for the presented experiments 250 - 300 l/h); a slight increase of the flow velocity is expected due to the influence of the exhaust system of the experimental hutch and the flow rate of the confinement-air. Those parameters have to be adjusted to optimize the particle density of the aerosol (determining X-ray signal quality and exposure time) and for confining the flow in the inner tube. For the presented experiments with EtOH-based precursor solution, the aerosol was generated with a commercial aerosol generator (TSI 3079 Atomizer, Topas GmbH., Germany) functioning as a two-stream injection nozzle.

Sample preparation: Aerosols were produced from an ethanol-rich precursor solution of tetraethylorthosilicate (TEOS)/cetyltrimethylammonium bromide (CTAB)/HCl/H2O/EtOH at

molar ratios of 1(TEOS):0.15(CTAB):0.004(HCl):5(H_2O):22(EtOH) (Lu et al. 1999) and solutions with equivalent molar ratios of CTAB/EtOH and CTAB/EtOH/H_2O. Deionized H_2O was used in Millipore quality. TEOS and CTAB were purchased from Sigma Aldrich (Vienna, Austria); EtOH, HCl from Bartelt (Graz, Austria). The precursor solutions were used after about 6 up to max. 12 hours.

X-ray measurements and data analysis: *In situ* gas-phase SAXS measurements were performed at the Austrian SAXS beamline at ELETTRA, Trieste, Italy at an energy of 8 keV (Amenitsch et al. 1998). The scattering patterns were recorded with a 2D image plate detector (Mar300, MarResearch, Norderstedt, Germany) using collection times of 200 - 250 s. The scattering vector *q* (difference between the vector of the incoming and the scattered wave) is related to the scattering angle 2θ via $q = 4\pi\sin(\theta)/\lambda$ (λ- wavelength) and is inversely related to the repeat-distance (d-spacing) of the sample mesostructure. The gas-phase measurements were restricted to the strongest low-order reflection due to the low scattering intensity of the aerosol, mainly limited by the low particle concentration. Before analysis, the background signal measured at the corresponding positions was subtracted from the patterns and the resulting images were radially integrated using the software FIT2D (Hammersley 1998). The peak parameters were evaluated using the software package IGOR (WaveMetrics, Inc.). Peak position and area were fitted using the function

$$I_q = \left(A/\left(1 + \left((q - q_0)/fwhm\right)^2\right)\right) + a + bq + cq^2$$

combining a second order polynomial as residual background with a Lorentz function, with *A* peak height, *fwhm* full width at half maximum, and q_0 peak position.

Results and Discussion

1. Characterization of the experimental setup

Physical parameters during drying have previously been shown to influence the mesostructure formation by their impact on solvent composition and drying speed, influencing Si-condensation and degree of order (Hampsey et al. 2005; Bore et al. 2003; Boissiere et al. 2003). Fig. 2a shows the temperature gradients measured at different maximum set temperatures without aerosol flow, with the heater setup used for the presented experiments. The temperature at the dryer entrance was kept at approximately

room temperature; the temperature gradient was raised by setting the maximum temperature in the heated part to 100°C, 120°C, 150°C and 190°C.

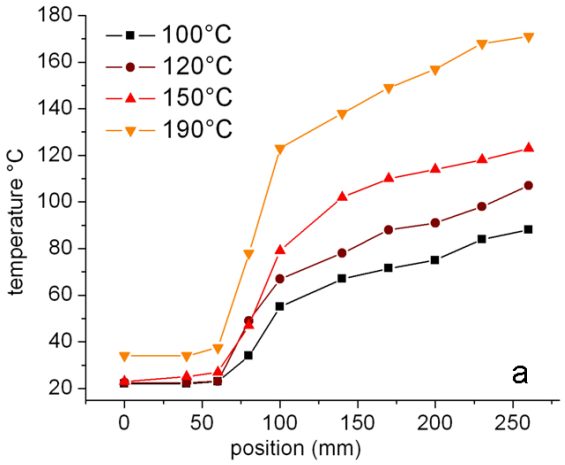

Fig. 2 (a) *Temperature steps achieved at maximum set temperatures of 100°C (squares), 120°C (dots), 150°C (triangles up) and 190°C (triangles down) without aerosol flow.*

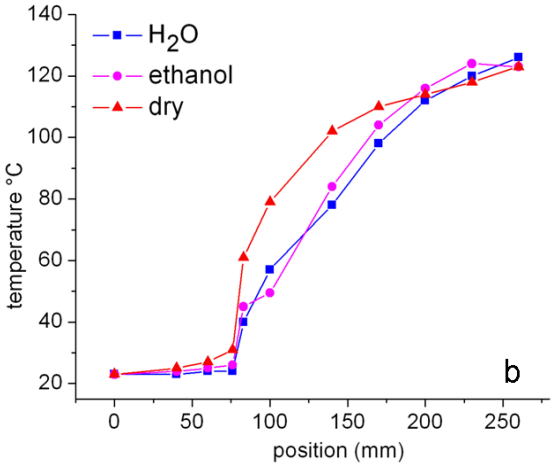

Fig. 2 (b) *Axial temperature profiles with aerosol of water (square) and 70% EtOH (dots) and without aerosol flow (triangle) with 150°C max. set temperature at the heated end. The insulation between heated and cooled part is located at 80 mm. The cooled part was kept at approximately room temperature.*

Flow velocity and heat capacity of the aerosol have a direct influence on the temperature increase of the aerosol during drying and the radial temperature gradient in the dryer tube (which is changing with axial position and aerosol temperature). To assess the influence of solvent composition on the temperature step, temperature profiles of aerosol of deionized

water and 70% EtOH were measured as reference. Fig. 2b shows profiles of these aerosols with the maximum dryer temperature set to 150°C, compared to the profile without aerosol flow. The influence of the aerosols and their different heat capacity and evaporation temperature (corresponding to different positions in the flow reactor) is clearly visible immediately after the separation; with progressive drying it is compensated. This is also valid for aerosols containing non-volatile solution components (surfactant and Si-precursor), the temperature gradients of these systems are also dominated by heater control and solvent evaporation.

2. X-ray experiments

CTAB-solutions: Fig. 3a shows SAXS measurements of aerosol of CTAB/EtOH solution during spray drying. A clear increase of peak height was observed in the measurements during initial mesostructure formation and subsequent drying of the structure (Fig. 3b). Crystallisation of CTAB from a highly concentrated, ethanolic solution is expected to result in a lamellar crystalline mesostructure (Campanelli and Scaramuzza 1986). In bulk solution, ethanol is known to enrich between head and tail groups of the surfactant (Doshi et al. 2003), therefore suppressing curvature induction of the surfactant and disturbing micelle formation (Zana 1995). Formation of a lamellar phase parallel to interfaces (interfaces with solid substrate or air) during EISA is also a typical feature of confined systems such as aerosol droplets (Fan et al. 2008). The maximum observed at q ~ 2.1 nm^{-1} corresponds to a lattice-spacing of ~ 3 nm that is larger than the length of the stretched CTAB tailgroup of ~ 2.2 nm (Venkataraman and Vasudevan 2001), possibly relating to a strongly tilted surfactant bilayer. The observed slight changes of peak position (Fig. 3b) could be tentatively explained based on findings for thin films (Doshi et al. 2003): initial evaporation of the interlamellar ethanol results in a slight decrease of lattice-spacing, subsequent evaporation of ethanol intercalated in the surfactant layer results in a slight increase of the characteristic repeat distance at the final drying stage. The opposite behavior of the H_2O containing solution can be explained by a sterical effect of H_2O molecules associated with the surfactant headgroups during initially faster evaporation of ethanol, before water finally evaporates with a time-delay at the final stage.

The purpose of these first measurements was to show the feasibility of following the mesophase formation in the gas-phase with the presented setup. The results show a potential for characterizing also chemically more complex systems that might show interesting behavior in 3D-confinement. It should be pointed out, that Fig. 3a shows the original curves after background subtraction, and that a clear signal could be obtained although the scattering contrast (electron density contrast) of CTAB is lower than e.g. of condensing silica.

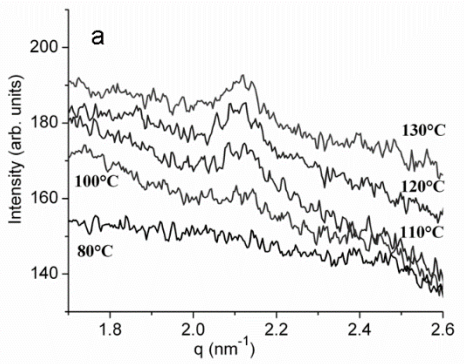

Fig. 3 (a) *SAXS patterns of aerosol of CTAB/EtOH solution during drying at max. set temperature of 150°C. The curves are offset for better visibility, the numbers represent the approximate temperature according to Fig. 2b.*

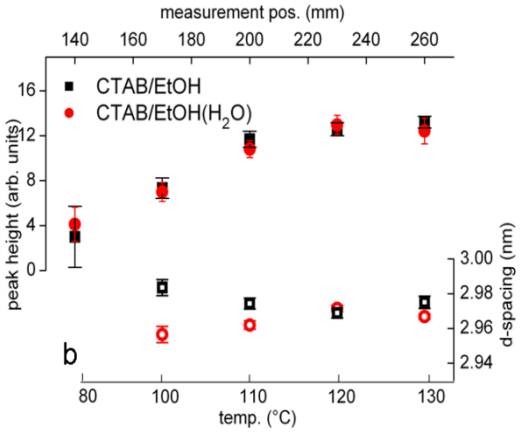

Fig. 3 (b) *Peak height (full circle/square) and d-spacing (open circle/square) during drying of CTAB/EtOH and CTAB/EtOH/(H_2O) solution.*

EISA of Si-precursor solution: Solvent composition and content of the precursor solution was previously shown to have an impact on the lattice-spacing of the formed mesostructure:

Ethanol influences the size of micelles in bulk solution or thin films (Fontell et al. 1991; Doshi et al. 2003) and inhibits Si-condensation (Boissiere et al. 2003). H_2O has a geometrical role and aids Si-condensation in the precursor solution. In thin films, a structural effect was observed when humidity from the ambient atmosphere was adsorbed to the drying system (Doshi et al. 2003; Cagnol et al. 2003). We examined the influence of Si-condensation in the precursor solution by measuring aerosols produced from the same batch with intervals of several hours (keeping the remaining solution in a closed vessel on a stirring plate to avoid ethanol evaporation), but we found no significant impact of this factor on the characteristic repeat distance. An influence of decreasing solution ethanol content was, however, clearly visible as an increase of lattice-spacing already at the dryer entrance, before the aerosol drying (data not shown). The influence of H_2O adsorbed from humidified carrier gas and confinement-air was assessed with a previous prototype of the setup. An effect on the repeat distance was visible in the first stages of drying, but was compensated at the end of the drying process. An improvement of the degree of order in the dry powder was observed by applying low (80°C) dryer temperatures (Bore et al. 2003; Shyjumon et al. *submitted*).

Measurements of aerosol of TEOS/CTAB//EtOH/H_2O solution showed a signal at $q \sim 1.6$ nm^{-1} corresponding to the (10) reflection of a 2D hexagonal phase, consistent with previous studies reporting such a structure for comparable systems (Boissiere et al. 2003; Bore et al. 2003). Also this system showed no significant change of repeat distance during drying, only a slight decrease of first order lattice-spacing at the end of the dryer (Fig. 4), at temperatures above 100°C. A decrease of about 0.2 nm was also observed by Boissiere et al. (2003) for measurements at the dryer exit. During the beginning of the drying process (50-100°C), the initial repeat distance was preserved, indicating that ethanol evaporation during spray-drying is too fast to allow any significant mesophase transitions in the course, as were observed for thin films (Grosso et al. 2004).

Powder deposit was collected at the dryer exit during the presented experiments and was measured immediately and three days later (supplementary information). The lattice-spacing remained the same, indicating that the drying was complete after passage of the dryer tube.

Conclusions

We present a new *in situ* aerosol flow reactor that allows to follow the structural changes in mesostructured aerosols during solvent-evaporation/Si-condensation along an adjustable temperature gradient. Controlling the drying process and flow conditions was possible by applying different temperature profiles and by adapting the flow rate of confinement-air and exhaust. First experiments were performed on EISA of CTAB/EtOH solutions. It was possible to gain quasi time-resolved gas-phase measurements of the initial mesophase formation during EISA in aerosol droplets. A clear increase of peak height was observed in the measurements, allowing to follow the mesostructure formation of CTAB/EtOH solutions and changes during subsequent drying of the structure. *In situ* measurements of EISA of Si-precursor solution showed that the lattice-spacings did not change considerably in the course of mesostructure formation, but that they were mostly determined by the precursor solution. The lattice-spacing also remained stable in the collected powder. At least for ethanol based systems, spray drying therefore seems to offer a route that allows to control the final unit cell dimensions directly via the solution composition, probably because drying and stabilization happen too fast to allow the additional processes observed for thin films.

In the future, this setup will be applied for direct mesostructural characterization of aerosols, for even more complex processes like self-assembly of hierarchical porous structures, co-crystallization of nanoparticles in mesoporous materials or the role of 3D-confinement on self-assembly and crystallization. It is also planned to integrate complementary methods for droplet and particle characterization, like static light scattering for size measurements.

Acknowledgements

We thank Christian Morello for his support with the setup. The study was financed by the project SAXIER contract no. RIDS 011934.

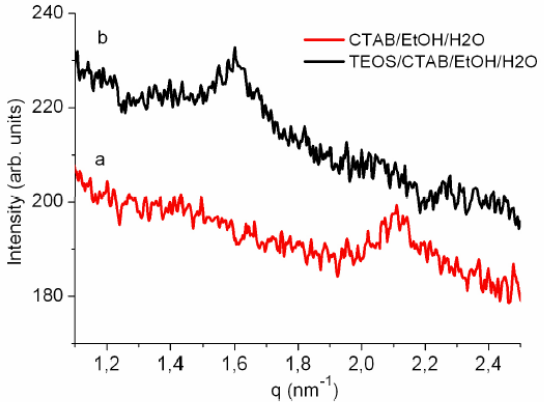

Figure S1: *SAXS patterns (after background subtraction) of aerosol of CTAB/EtOH/H2O (**a**) at the first position with a fully developed peak (appr. 110°C), and TEOS/CTAB/EtOH/H2O solution (**b**), at the first measurement position (appr. 55°C).*

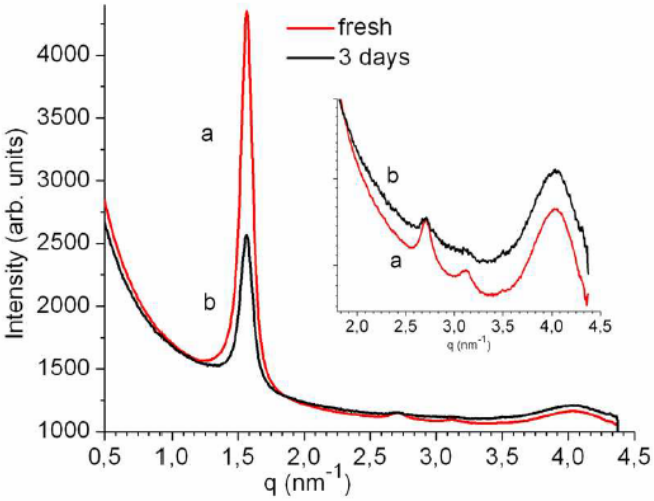

Figure S2: *Measurements of powder deposits of TEOS/CTAB/EtOH/H2O solution. Aerosol was collected at the dryer exit, measured immediately (**a**) and three days later (**b**). The insert shows the higher order reflections in log scale. The peaks visible in the diffraction pattern can be indexed as the (10), (11), (20) reflections with their characteristic d-spacing ratios 1, $\sqrt{3}$ and 2 of a hexagonal phase. (The reflection at q ~4 nm^{-1} is due to Kapton tape.)*

References

Alonso, B., Véron, E., Durand, D., Massiot, D., Clinard, C. (2007). New Insights into the Formation of Textures through Spray-Drying and Self-Assembly. Microporous and Mesoporous Mater. 106:76-94

Amenitsch, H., Rappolt, M., Kriechbaum, M., Mio, H., Laggner, P., and Bernstorff, S. (1998). First Performance Assessment of the Small-angle X-ray Scattering Beamline at ELETTRA. J. Synchrotron Radiation 5:506-508.

Areva, S., Boissiere, C., Grosso, D., Asakawa, T., Sanchez, C., and Linden, M. (2004). One-Pot Aerosol Synthesis of Ordered Hierarchical Mesoporous Core-Shell Silica Nanoparticles. Chem. Comm. 10:1630-1631.

Boissiere, C., Grosso, D., Amenitsch, H., Gibaud, A., Coupé, A., Baccile, N., and Sanchez, C. (2003). First In-Situ SAXS Studies of the Mesostructuration of Spherical Silica and Titania Particles during Spray-Drying Process. Chem. Comm. 9:2798-2799.

Boissiere, C., Grosso, D., Chaumonnot, A., Nicole, L., and Sanchez, C. (2010). Aerosol Route to Functional Nanostructured Inorganic and Hybrid Porous Materials. Adv. Mater. (published online)

Bore, M. T., Rathod, S. B., Ward, T. L., and Datye, A. K. (2003). Hexagonal Mesostructure in Powders Produced by Evaporation-Induced Self-Assembly of Aerosols from Aqueous Tetraethoxysilane Solutions. Langmuir 19:256-264.

Brinker, C. J., Lu, Y., Sellinger, A., and Fan, H. (1999). Evaporation-Induced Self-Assembly: Nanostructures Made Easy. Adv. Mater. 11:579-585.

Bruinsma, P. J., Kim, A. Y., Liu, J., and Baskaran, S. (1997). Mesoporous Silica Synthesized by Solvent Evaporation: Spun Fibers and Spray-Dried Hollow Spheres. Chem. Mater. 9:2507-2512.

Cagnol, F., Grosso, D., Soler-Illia, G. J. D. A., Crepaldi, E. L., Babonneau, F., Amenitsch, H., and Sanchez, C. (2003). Humidity-Controlled Mesostructuration in CTAB-Templated Silica Thin Film Processing. The Existence of a Modulable Steady State. J. Materials Chemistry 13:61-66.

Campanelli, A. R., and Scaramuzza, L. (1986). Hexadecyltrimethylammonium bromide. Acta Cryst. C. 42:1380-1383

Doshi, D. A., Gibaud, A., Liu, N., Sturmayr, D., Malanoski, A. P., Dunphy, D. R., Chen, H., Narayanan, S., MacPhee, A., Wang, J., Reed, S. T., Hurd, A. J., Van Swol, F., and Brinker, C. J. (2003). In-situ X-ray Scattering Study of Continuous Silica - Surfactant Self-Assembly during Steady-State Dip Coating. J. Physical Chemistry B 107:7683-7688.

Dourdain, S., Rezaire, A., Mehdi, A., Ocko, B. M., and Gibaud, A. (2005). Real Time GISAXS Study of Micelle Hydration in CTAB Templated Silica Thin Films. Physica B: Condensed Matter 357:180-184.

Fan, J., Boettcher, S. W., Tsung, Ch.-K., Shi, Q., Schierhorn, M., and Stucky, G. D. (2008). Field-Directed and Confined Molecular Assembly of Mesostructured Materials: Basic Principles and New Opportunities. Chem. Mater. 20:909–921.

Fontell, K., Khan, A., Lindström, B., Maciejewska, D., and Puang-Ngern, S. (1991). Phase Equilibria and Structures in Ternary Systems of a Cationic Surfactant (C16TABr or (C16TA)2SO4), Alcohol, and Water. Colloid and Polymer Sci. 269:727-742.

Gibaud, A., Grosso, D., Smarsly, B., Baptiste, A., Bardeau, J. F., Babonneau, F., Doshi, D. A., Chen, Z., Brinker, J. C., and Sanchez, C. (2003). Evaporation-Controlled Self-Assembly of Silica Surfactant Mesophases. J. Physical Chemistry B 107:6114-6118.

Grosso, D., Cagnol, F., Soler-Illia, G. J. D. A., Crepaldi, E. L., Amenitsch, H., Brunet-Bruneau, A., Bourgeois, A., and Sanchez, C. (2004). Fundamentals of Mesostructuring through Evaporation-Induced Self-Assembly. Adv. Func. Mater. 14:309-322.

Hammersley, A. P. (1998). FIT2D V9.129 Reference Manual V3.1, ESRF Internal Report ESRF98HA01T.

Hampsey, E. J., Arsenault, S., Hu, Q., and Lu, Y. (2005). One-Step Synthesis of Mesoporous Metal-SiO2 Particles by an Aerosol-Assisted Self-Assembly Process. Chem. Mater. 17:2475-2480.

Jayanthi, G. V., Zhang, S. C., and Messing, G. L. (1993). Modeling of Solid Particle Formation during Solution Aerosol Thermolysis: The Evaporation Stage. Aerosol Sci. Technol. 19:478-490.

Kammler, H. K., Beaucage, G., Kohls, D. J., Agashe, N., and Ilavsky, J. (2005). Monitoring Simultaneously the Growth of Nanoparticles and Aggregates by In Situ Ultra-Small-Angle X-ray Scattering. J. Appl. Phys. 97:054309

Kim, H.-S., Lee, K.-H., and Kim, S.-G. (2006). Growth of Monodisperse Silver Nanoparticles in Polymer Matrix by Spray Pyrolysis. Aerosol Sci. Technol. 40:536–544.

Lu, Y., Fan, H., Stump, A., Ward, T. L., Rieker, T., and Brinker, C. J. (1999). Aerosol-Assisted Self-Assembly of Mesostructured Spherical Nanoparticles. Nature 398:223-226.

Marmiroli, B., Grenci, G., Cacho-Nerin, F., Sartori, B., Laggner, P., Businaro, L., and Amenitsch H. (2010). Experimental Set-Up for Time Resolved Small Angle X-ray Scattering Studies of Nanoparticles Formation using a Free-Jet Micromixer. Nuclear Instruments and Methods in Physics Res. B 268:329–333

Mitchell, J. B. A., di Stasio, S., LeGarrec, J. L., and Florescu-Mitchell, A. I. (2010). Synchrotron Radiation Studies of Additives in Combustion I: Water. Nuclear Instruments and Methods in Physics Res. B 268:1486–1491.

Moon, Y. K., Lee, J., Lee, J. K., Kim, T. K., and Kim S. H. (2009). Synthesis of Length-Controlled Aerosol Carbon Nanotubes and their Dispersion Stability in Aqueous Solution. Langmuir 25:1739-1743.

Rao, R. G. V., Lopez, G. P., Bravo, J., Pham, H., Datye, A. K., Xu, H. F., and Ward, T. L. (2002). Monodisperse Mesoporous Silica Microspheres formed by Evaporation-Induced Self Assembly of Surfactant Templates in Aerosols. Adv. Mater. 14:1301-1304.

Ravichandran, R. (2009). Nanotechnology-Based Drug Delivery Systems. Nanobiotechnol. 5:17–33.

Sanchez, C., Rozes, L., Ribot, F., Laberty-Robert, C., Grosso, D., Sassoye, C., Boissiere, C., and Nicole, L. (2010). ‘‘Chimie Douce’’: A Land of Opportunities for the Designed Construction of Functional Inorganic and Hybrid Organic-Inorganic Nanomaterials. C. R. Chimie 13:3–39.

Schaefer, D. W., Olivier, B. J., Hurd, A. J., Beaucage G. B., Ivie, J. J., and Herd, C. R. (1991). Structure of Combustion Aerosols. J. Aerosol Sci. 22:447-450.

Sen, D., Spalla, O., Taché, O., Haltebourg, P., and Thill, A. (2007). Slow Drying of a Spray of Nanoparticles Dispersion: In situ SAXS Investigation. Langmuir 23:4296-4302.

Shyjumon, I., Rappolt, M., Sartori, B., Amenitsch, H., and Laggner, P. (2008). Novel In Situ Setup to Study the Formation of Nanoparticles in the Gas Phase by Small Angle X-ray Scattering. Rev. Scientific Instruments 79:043905.

Shyjumon, I., Rappolt, M., Sartori, B., Marmiroli, B., Cacho-Nerin, F., Grenci, G., Amenitsch, H., and Laggner P. Mesostructured Si-Particles studied by Comparison of Gas Phase and Powder Deposit X-ray Diffraction. submitted

Tsapis, N., Bennett, D., Jackson, B., Weitz, D. A., and Edwards, D. A. (2002). Trojan Particles: Large Porous Carriers of Nanoparticles for Drug Delivery. Proc. Nat. Acad. Sci. U. S. A. 99:12001-12005.

Venkataraman, N. V., and Vasudevan, S. (2001). Hydrocarbon Chain Conformation in an Intercalated Surfactant Monolayer and Bilayer. Proc. Indian Acad. Sci. (Chem. Sci.) 113:539–558

Wise, M. E., Biskos, G., Martin, S. T., Russell, L. M., and Buseck, P. R. (2005). Phase Transitions of Single Salt Particles studied using a Transmission Electron Microscope with an Environmental Cell. Aerosol Sci. Technol. 39:849–856.

Zana, R. (1995). Aqueous Surfactant-Alcohol Systems: A Review. Adv. Coll. Interf. Sci. 57:l- 64